Enhancing the piston effect in underground railways

by
Daniel Marshall Cross

A thesis submitted in partial fulfilment of the
requirements for the degree of
Doctor of Philosophy

University of Sheffield
Faculty of Engineering
Department of Mechanical Engineering

March 2017

Acknowledgments

This study would not have been possible without the support and guidance of my supervisors, Dr Ben Hughes, Professor Derek Ingham and Professor Lin Ma. Without their support and encouragement, I would never have been able to complete this study.

My thanks also go to Guy Brammar and Paul Cook for their generous funding and great enthusiasm for this study. I am also grateful to the EPSRC for providing funding through a CASE Award Studentship (#1344073) and a Graduate Internship.

I have met many people through the course of this study, in Leeds and Sheffield, who have provided support, jokes and distractions, for which I am grateful.

I would like to thank all my family for their support, and for reminding me of life away from this study.

I would like to thank all the staff at the University of Leeds and the University of Sheffield for all the help and support they provided.

Finally, I would like to thank my wife, Rici, for everything.

Enhancing the piston effect in underground railways

Abstract

The purpose of this study was to investigate methods of enhancing the piston effect in underground railways for the improvement of thermal conditions on platforms. In many underground railways, the piston effect is used to provide ventilation. However, in older underground railways insufficient ventilation can lead to high temperatures, largely due to heat from train braking. Additionally, the energy demand from ventilation and cooling equipment in newer underground railways can be significant. Enhancing the piston effect can provide additional ventilation for improved thermal conditions or a reduced energy demand.

Two novel devices for the enhancement of the piston effect were investigated; a train fin and aerofoil. Through influencing the air flow patterns around a train, the devices alter the train air displacement and aerodynamic work. Moreover, variation of the fin size or the aerofoil angle of inclination allows the air displacement and aerodynamic work to be controlled. The influence of an enhanced piston effect on the thermal conditions on an underground platform is shown to reduce the air temperatures, through the enhanced displacement of braking heat. Two- and three-dimensional computational fluid dynamics models were developed, and verified with experimental data from the literature, to study numerically the piston effect, train fin and aerofoil and the thermal conditions on an underground platform.

The results from the numerical analysis showed that a train aerofoil can increase air displacement by around 8%, with no increase in the aerodynamic work. It was found that an increase in the piston effect of $10\,\mathrm{m^3s^{-1}}$ could reduce the highest air temperatures on an underground platform by between 0.16–0.29 °C. The cooling effect of enhancing the piston effect was found to be between 4.5–5.6 kW.

Publications

The work presented in this thesis was carried out between October 2012 and January 2015 at the School of Process, Environment and Materials Engineering, University of Leeds and between January 2015 and March 2017 at the Department of Mechanical Engineering, University of Sheffield. As an outcome of the work, the following research output has been published:

1. Cross, D., Hughes, B., Ingham, D., & Ma, L. (2015). A validated numerical investigation of the effects of high blockage ratio and train and tunnel length upon underground railway aerodynamics. *Journal of Wind Engineering and Industrial Aerodynamics*, 146, 195–206
2. Cross, D., Hughes, B., Ingham, D., & Ma, L. (2017). Enhancing the piston effect in underground railways. *Tunnelling and Underground Space Technology incorporating Trenchless Technology Research*, (pp. 71–81)

Contents

Nomenclature

Symbol	**Term**	**Unit**
α_c	Layer collapse factor	-
α_s	Layer split factor	-
β	Blockage ratio	-
β_g	Train-tunnel gap blockage ratio	-
Γ	Scalar diffusion coefficient	$\mathrm{m^2s^{-1}}$
ϵ	Turbulent dissipation	$\mathrm{m^2s^{-3}}$
θ	Aerofoil angle of inclination	$^\circ$
κ	von Kármán constant	-
λ	Coefficient of thermal conductivity	$\mathrm{Wm^{-1}K^{-1}}$
μ	Dynamic viscosity	$\mathrm{kgm^{-1}s^{-1}}$
μ_t	Eddy viscosity	$\mathrm{kgm^{-1}s^{-1}}$
ρ	Density	$\mathrm{kgm^{-3}}$
τ	Shear stress	$\mathrm{kgm^{-1}s^{-2}}$
ϕ	General scalar quantity	-
A_t	Cross-sectional area of the tunnel in the y-z plane	$\mathrm{m^2}$
A_{tr}	Cross-sectional area of the train in the y-z plane	$\mathrm{m^2}$
c	Chord length	m
C_D	Drag coefficient	-
C_D^P	Pressure drag coefficient	-
C_D^V	Viscous drag coefficient	-
C_p	Pressure coefficient	-
${}^{du_{tr}}\!/_{dt}$	Rate of acceleration or deceleration	$\mathrm{ms^{-2}}$
e	Specific enthalpy	$\mathrm{Jkg^{-1}}$

E	Empirical constant	-
F_x	Drag force acting in the x direction	kgms^{-2}
h	Cell height adjacent to moving boundary	-
k	Turbulent kinetic energy	kgm^{2}s^{-2}
M	Mach number	-
u_{tr}	Train velocity	ms^{-1}
u_{tr}^{max}	Maximum train velocity	ms^{-1}
$(u_{rel}, v_{rel}, w_{rel})$	Velocity relative to the moving train	ms^{-1}
u_*	Reference velocity	ms^{-1}
$U = (u, v, w)$	Velocity	ms^{-1}
U_{max}	Maximum train velocity	ms^{-1}
U_g^+	Normalised velocity through the train-tunnel gap	-
U_o^+	Normalised velocity at the tunnel outlet	-
U^*	Dimensionless velocity	-
PMV	Predicted mean vote	
PPD	Predicted percentage of dissatisfied	
p	Pressure	Pa
P	Aerodynamic power	W
P_P^+	Normalised aerodynamic power due to the pressure force	-
P_V^+	Normalised aerodynamic power due to the viscous force	-
Q_b	Braking heat load	W
Q_r	Residual heat	W
RWI	Relative warmth index	
Re	Reynolds number	-
Re_{max}	Reynolds number at maximum train velocity	-
s	Train stopping distance	m
t	Time	s
t_T	Total train travel time	s

T	Temperature	°C
T^+	Normalised time	-
T_a	Train arrival time	s
T_d	Train departure time	s
V	Volume	$\mathrm{m^3}$
V_t	Tunnel volume	$\mathrm{m^3}$
V^+	Normalised air volume	-
$\dot{V}$	Volume flow rate	$\mathrm{m^3s^{-1}}$
$\dot{V}_g^+$	Normalised air flow rate through the train-tunnel gap	-
$\dot{V}_o^+$	Normalised air flow rate at the tunnel outlet	-
W	Aerodynamic work	$\mathrm{kgm^2s^{-2}}$
W_P^+	Normalised aerodynamic work due to the pressure force	-
W_V^+	Normalised aerodynamic work due to the viscous force	-
(x, y, z)	Cartesian coordinates	-
x_f	Width of train fin	m
x_t	Tunnel length	m
x_{tr}	Train length	m
y_{gap}	Height of the train-tunnel gap	m
y_t	Tunnel height	m
y_{tr}	Train height	m
y^*	y star	-
z_a	Width of the train-tunnel gap occupied by the aerofoil	m
z_f	Height of train fin	m
z_{gap}	Width of the train-tunnel gap	m
z_t	Tunnel width	m
z_{tr}	Train width	m

Z	Mesh velocity	ms^{-1}

1

Introduction

Underground railways—also known as métro or subway systems—form an important part of the transport systems in many cities around the world. Such systems can rapidly move large numbers of people into and around densely developed urban areas without occupying large areas of land or causing the environmental problems associated with road transport. An underground railway consists of a network of tunnels connecting underground stations, which can be accessed by passengers from the surface by stairs, escalators and lifts. In this context an underground railway is distinct from a railway tunnel, the purpose of which is to allow a railway to overcome a geographical obstacle such as a hill or river.

1.1 Underground railways in London

The early underground railways were built in the mid 19th century, in the major European capitals. The world's first underground railway, the Metropolitan Railway, was opened in London in 1863 [139]. The construction of railways in central London had been prohibited and as a result the mainline railway termini in London were restricted to the edge of the city. London, a major economic and political centre, also suffered from significant traffic problems caused by population and economic growth. The Metropolitan Railway proposed to connect together the several railway termini and the city to improve transport in the growing city. However, because of the restriction on railway construction in the city and the dense surface development, a subterranean railway was envisaged. The construction of the Metropolitan Railway was carried out using the cut-and-cover method, where a trench is dug in the street in which the railway is constructed and then covered over to create the tunnel, and the street then reinstated. However, this method of construction was inherently disruptive.

Although the initial aim of the Metropolitan Railway was to improve access to London, various extensions into rural areas north of London opened these areas to development. The spread of the railway encouraged the development of suburbs, becoming known as 'Metro-land'.

Although the Metropolitan Railway was considered a success, the cut-and-cover method of construction caused a significant degree of disruption and required the agreement of various landowners. Therefore, when the City and South London Railway advanced plans for a new underground railway line, a deep level railway was proposed, to avoid difficulties with surface development. These deep level tunnels were bored through the ground using a tunnelling shield, and thus resulted in narrow, circular tunnels—which lent the London Underground the nickname the Tube. The depth and size of the tunnels on the City and South London Railway led to the use of electric traction in place of steam, which had been used elsewhere in underground railways, therefore becoming the world's first deep level underground railway on opening in 1890.

The City and South London Railway, now part of the the Northern Line in London, set the form for many future underground railways, consisting of two separate tubes for up and down traffic and electric traction. Over the following decades, the newer lines opened in London followed a similar design, but with various improvements—the Victoria Line opened with an early form of automatic train operation and the Jubilee Line extension included platform doors for greater passenger safety.

1.2 Thermal conditions

The construction and operation of underground railways is challenging in many respects—the civil engineering in an urban area is complex and expensive as are the systems required for safe operation, significant numbers of passengers must be managed within the system and a safe environment must be maintained in terms of fire, air quality or terrorist attack.

The operation of an underground railway presents a significant challenge in maintaining acceptable thermal conditions. Although there are many sources of heat in an underground railway, the majority—around 80-85% in London Underground [121, 23, 4]—is generated by train brakes. As a train arrives in a station, the braking mechanism releases significant amounts of heat, converted from the train kinetic energy, into the air within the station and surrounding tunnels, leading to a rise in air temperature. In early underground railways, minimal consideration was given to tunnel ventilation. However, as the first underground railways were built close to ground level, they often had large openings to the open air and were generally built as double track tunnels, and thus the effect of braking heat on the temperatures is minimised.

Later underground railways, built in deep level tunnels, are more susceptible to effects of heat from train braking. As the tunnels and stations are generally of small cross section, the heat generated is dissipated into a small volume of air, thus resulting in a higher heat intensity. Moreover, the deep level at which the tunnels and stations are located, and a lack of openings to the atmosphere, means that removal of heat is difficult.

Upon construction, the deep level underground lines were initially cool, maintained as such by the clay surrounding the tunnels, which acted as a heat sink. London Underground even encouraged patronage by suggesting in adverts that the underground was a heaven from the hot summer weather. However, over decades of operation the temperature of the clay increased, reaching an average of 20–25 °C.

The average temperatures in a particular underground railway line can be related to the age and construction of the stations and tunnels. Generally, the highest temperatures are found in the older deep level underground tunnels and shallower cut-and-cover tunnels. The newer deep level tunnels are usually cooler then the oldest due to more consideration given to the requirement for cooling at the time of construction. In summer months considerable portions of the London Underground network have temperatures that are in the range of 27–32 °C [121].

1.3 Ventilation and cooling

In a modern underground railway, considerable effort is made to ensure thermal conditions are maintained within comfortable limits [124]. Stations and tunnels are built with high ceilings, large passageways and numerous ventilation shafts to reduce heat intensity and for the removal of heat. Additionally, mechanical ventilation systems are used to remove heat from stations, in particular from train braking and traction systems, and to supply fresh air. The new Elizabeth Line in London, which has been built at depths of up to 40 m where trains will operate at a maximum velocity of $100\,\mathrm{kmh^{-1}}$, will be cooled with a combination of fan driven ventilation shafts and air extraction from stations [112], in particular from the train brakes. As well as removing the heat from a modern underground railway, considerable effort is made to minimised heat generation. Measures such as lighter trains, low energy lighting, inclines on the approach to stations to reduce braking and regenerative braking to convert less kinetic energy to heat are used to reduce heat generation. In older systems, such as the London Underground, much of the infrastructure found in a modern underground railway is not present, leading to high temperatures.

Operators of both new and old underground railways face challenges. Old systems often experience problems with unacceptable thermal conditions, due to a lack of ventilation and cooling infrastructure which is difficult and expensive to construct. New systems face the challenge of reducing the energy demand from the ventilation and cooling infrastructure—about 14% of the energy demand on the Barcelona Metro is attributed to ventilation and cooling [27]. All underground railways face the challenge of climate change, which in London is expected to increase passenger dissatisfaction with temperatures significantly by 2050 [74].

1.4 The piston effect

A significant mechanism used for the ventilation of underground railways is the air flows induced by the movement of trains in a tunnel, known as the piston effect. As a train moves through a tunnel it acts like a piston—air is displaced ahead of the train and it sucks air from behind. In older underground railways in London the only ventilation provided is through this means, leading to poor thermal conditions. However, in the newer underground railways such as the Jubilee Line Extension, good design and numerous ventilation shafts allow acceptable thermal conditions to be maintained in normal operating conditions through using the piston effect alone [22]. As the piston effect is generated as a consequence of train movement, it is a useful means of ventilation. Moreover, as it requires no additional energy input, it may be considered to be a low energy form of ventilation.

A significant body of research exists into the mechanism of the piston effect and the influence on thermal conditions within stations and tunnels in underground railways. Also there is research into how mechanical ventilation systems can be optimised to work in conjunction with the piston effect air flows. Research on enhancing the capability of the piston effect to improve thermal conditions and the energy efficiency of an underground railway are limited. This study targets this area in order to achieve the objectives of the thesis.

1.5 Research aims and objectives

The aim of this research is to achieve a reduction in temperatures in underground railway stations using a low energy approach through utilising and enhancing the piston effect air flows. The study investigates the kinematic and geometric factors which effect the magnitude of the piston effect and the train drag. Methods of increasing or varying the piston effect are studied by altering the train aerodynamic resistance. The impact of enhancing the piston effect on heat displacement and thermal conditions in stations is determined.

The main objectives of this research are as follows:

1. Evaluate the effect of train blockage ratio, train and tunnel length on the air flows induced by the piston effect as well as the effect of kinematic factors.
2. Determine a method to increase the piston effect air flows through alterations in the shape of a train.
3. Consider the effect of enhancing the piston effect on the energy demand of the train.
4. Establish a transient model to determine the behaviour of the piston effect air flows in stations.
5. Consider the impact of an enhanced piston effect on the thermal conditions within an underground station.
6. Verify all the computational models using data from the literature, within sufficient bounds.

1.6 Research methodology

The study is divided into four parts, each a specific topic of work. The first part is a review of work relating to underground railway thermal conditions, means of energy demand reduction, methods of ventilation and cooling and the piston effect. From this review data was collected for the development and verification of numerical models.

The second part of the study investigates the impact of geometrical and kinematic factors on the piston effect air flows. A three-dimensional, transient, numerical model is used for the investigation to determine the factors, principally the blockage ratio, which influence an increase in the piston effect, and by what proportion.

The third part considers how the piston effect can be enhanced by altering the shape of a train, using a two-dimensional, transient, numerical model. Particular consideration is given to the impact on the energy demand of the train.

The fourth and final part of work determines the impact of an enhanced piston effect on thermal conditions within a underground station platform. Through considering the enhancement in the piston effect due to altering the shape of a train, the impact on temperatures and the overall cooling effect is found.

1.7 Outline of the thesis

This thesis is divided into seven chapters, a summary of which is as follows:

Chapter 1 introduces underground railways, the need for ventilation and cooling and the various ways in which it is delivered. The chapter further introduces the piston effect and the influence on ventilation and cooling. The research methodology is also summarised.

Chapter 2 presents a review of the literature relating to underground railway thermal conditions, energy demand, ventilation and cooling and the piston effect. The review covers experimental and numerical methods used to investigate underground railway ventilation and the piston effect. The research gap which forms the focus of this thesis is identified.

Chapter 3 presents the numerical models used in this thesis. This covers the governing equations, numerical method, the simulation of train motion using moving meshes and numerical and modelling errors. The processes of geometrical and kinematic scaling are also explained.

Chapter 4 presents an investigation of the factors which influence the piston effect. The effect of train and tunnel length on air displacement and aerodynamic work is shown. A benchmark configuration, with parameters similar to that of an existing underground railway, is presented and the pattern of air flows, air displacement and aerodynamic work explained. The blockage ratio is varied and compared with the benchmark configuration.

Chapter 5 considers methods by which the blockage ratio could be increased. A train fin and train aerofoil are introduced as a means of enhancing the piston effect. The effect of the fin and aerofoil are compared to a benchmark configuration to illustrate the effect on the air displacement and aerodynamic work.

Chapter 6 covers the the effect of piston effect on the air flows and thermal conditions in an underground railway platform. The station is modelled on a location on the London Underground. A transient model is used to find the pattern of air flows within the station complex and are used to provide boundary conditions for a steady state model which is used to consider the thermal conditions. The influence on the thermal conditions for increasing the piston effect are presented.

Chapter 7 concludes the thesis. The work of the thesis is summarised and the findings presented and discussed. Possible topics for further work are identified.

2

Literature review

2.1 Introduction

The operation of an underground railway generates a significant amount of heat, which acts to raise the temperature of stations, tunnels and trains. In order to maintain acceptable conditions a system of ventilation and cooling is required. The piston effect generates air flows within underground stations and tunnels which can assist the ventilation of these spaces.

This chapter presents a background and review of literature relating to each each of these areas. The heat sources in an underground railway are discussed as well as the thermal conditions in a variety of different underground railway systems. The various approaches and methods for ventilation and cooling are surveyed and compared. The energy demand of an underground railway is discussed with particular concern for ventilation and cooling. The mechanism of the piston effect is introduced and the factors which influence it are discussed. Finally, the position of this study within the context of previous work is discussed.

2.2 Heat sources

The heat sources in an underground railway are unsteady in space and time. Generally, the heat sources can be divided into two types; those generated by the operation of a train and those associated with the infrastructure of the railway. The main sources of heat are from the use of electricity, the inflow of air when the ambient is warmer than the underground railway and from metabolism.

The Subway Environmental Design Handbook [127] presents a breakdown of the heat sources in a typical underground railway. The breakdown was calculated using the Subway Environmental Simulation computer program [115], a standard tool used for the simulation of underground railway environmental conditions and for the design of environmental control systems. The breakdown of the heat sources is shown in Table 2.1.

Table 2.1: Heat sources in a typical underground railway for a $17.9\,\mathrm{ms}^{-1}$ design velocity [127].

	Heat load per train stop	
Source	Energy (J)	Proportion of total (%)
Braking	6.26×10^7	45.7
Acceleration	1.41×10^7	10.3
Third rail losses	1.06×10^6	0.8
Tunnel lighting	2.11×10^5	0.2
Train accessories	3.27×10^6	2.4
Train air conditioning	4.11×10^7	30.0
Station equipment and people	1.47×10^7	10.7

The largest source of heat—45.7%—is a result of the train breaking as it arrives at each station. Together with the heat from the accelerating train, this amounts to 56.0% of the heat generated. In total train heat sources, including air conditioning and other accessories, amount to 89.1% of all heat generated. The sources of heat associated with railway infrastructure and people are comparatively small, amounting to 10.9%.

Train breaking is fundamentally the dissipation of kinetic energy during deceleration. Traditionally underground trains have utilised dynamic breaking as the main means of breaking with friction brakes retained for emergency situations. In dynamic braking the motors are used as generators, driven by the decelerating train. The electrical energy is then dissipated through resistor banks in the form of heat. In modern underground trains the electrical energy, instead of being wasted as heat, can be stored in capacitors for use during acceleration or transmitted into the power system for use by other trains, thus reducing the generation of heat. Additional kinetic energy is lost through aerodynamic drag and mechanical resistance but generate a small amount of heat.

In accelerating the train, the electric motors must do work so that the kinetic energy of the train corresponds to the maximum speed. Additionally, mechanical losses must be overcome which include mechanical resistance and aerodynamic drag which are lost in the form of heat. Electrical power is transmitted to trains through a third rail or overhead wire. The greatest losses, in the form of heat, occur during acceleration when the current demand is highest. Air conditioning systems on trains extracts heat from the interior of the carriages and releases it into the tunnels and stations. Additionally the air conditioning equipment performs work and thus generate heat. Air conditioning generates the second largest amount of heat in an underground railway. As the braking heat energy is generated as the train decelerates on approach to a station, the distribution of heat is concentrated in certain regions.

The effect of running at speed to the heat sources in an underground railway is not included in Table 2.1, as in the model the stations were so closely spaced as to make the contribution negligible. In practice many underground railways will also have stations located so close as to mean that this assumption is sufficient. However, if stations are spaced a distance apart such that the train runs at speed for significant periods of time, then the heat load will be more significant, and will raise the average temperature of the underground railway.

Figure 3.1 shows the spatial distribution of breaking heat energy dissipated by a train in the approach tunnel to a station, the station and the departure tunnel [127]. The spatial distribution represents the dissipation of heat during the arrival and departure of a train from a station, in a worst case scenario.

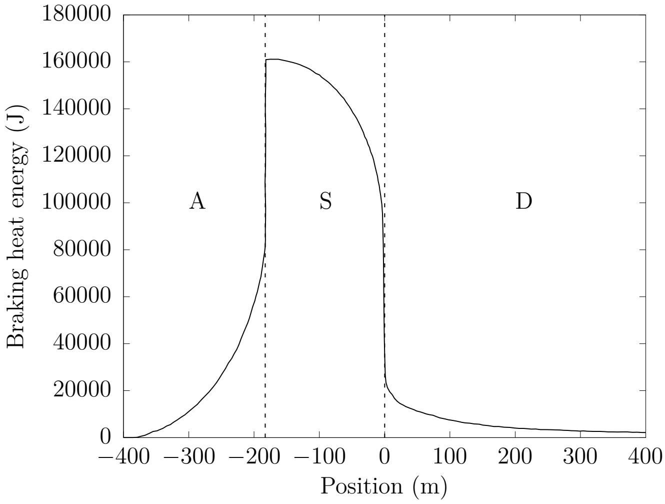

Figure 2.1: Spatial distribution of braking heat energy in a typical underground railway for a 26.8 ms^{-1} design velocity (A: approach tunnel, S: station, D: departure tunnel) [127].

As the train approaches the station deceleration begins in the approach tunnel and heat is dissipated in the tunnel, close to the station. The majority of heat is dissipated in the station itself, as the train decelerates and waits at the platform. A small amount of heat is dissipated in the departure tunnel, which is dissipated by the train as it departs. The worst case scenario means that the energy is dissipated as heat rapidly, while at less than the worst case scenario heat would be dissipated more evenly in time. However, over each station stop the capacity of the resistors to store heat decreases and more energy is dissipated as heat.

Values for the spatial distribution of breaking heat energy for the case shown in Figure 3.1 and various other design velocities are shown in Table 2.2.

Table 2.2: Spatial distribution of breaking heat energy in a typical underground railway [127].

	Proportion of braking heat dissipation (%)		
Design velocity (ms^{-1})	Approach tunnel	Station	Departure tunnel
17.8	4.0	69.9	26.1
22.4	6.9	65.3	27.8
26.8	10.9	61.9	27.2
31.3	15.3	58.9	25.8
35.8	22.3	54.7	23.0

For higher design velocities, the amount of heat dissipated in the approach tunnel increases as deceleration starts further from the station. The heat dissipation is greatest in the station, above 50% for all design speeds. Table 2.3 shows the spatial distribution of all dissipated heat energy.

Table 2.3: Spatial distribution of all dissipated heat energy in a typical underground railway [127].

	Proportion of heat dissipation (%)		
Design speed (kmh^{-1})	Approach tunnel	Station	Departure tunnel
17.8	5.1	65.3	29.6
22.4	7.2	57.5	35.3
26.6	9.7	51.5	38.8
31.3	12.1	46.3	41.6
35.8	15.8	40.8	43.4

Including all heat sources changes the spatial distribution of the dissipated heat energy. In particular, the inclusion of the acceleration heat load, increases the proportion of heat dissipation in the departure tunnel, particularly at the highest design speeds. At most design speeds the majority of heat dissipation occurs in the station, due to the dominance of braking heat load, as a proportion of the total.

Ampofo et al. [4] carried out an investigation of the heat loads in an underground railway. The analysis used a similar approach to the Subway Environmental Design Handbook [127] but did not consider the influence of train air conditioning. The investigation was focused on the underground railway environment in the UK, therefore the inclusion of air conditioning is not relevant as it is absent in most systems. Table 2.4 presents the breakdown of heat sources in a generic underground railway station and tunnels.

Table 2.4: Heat sources in a generic UK underground railway station and tunnels [4].

Source	Proportion of total (%)
Braking	85
Train	13
Tunnel lighting	2

The braking system is clearly the dominant heat source. From the mathematical model presented by the authors, it appears that the heat generated during acceleration is included in the braking term. The value given for the breaking heat load is close to that given in the Subway Environmental Design Handbook is air conditioning is excluded and acceleration and breaking sources are combined. Abi-Zadeh et al. [2], in a study of a UK underground railway, also quote the braking heat load as being 85% of the total, but give no justification for the value. Bendelius [21] presented the heat loads in the Atlanta underground railway system finding that the breaking and air conditioning heat loads were greater than the next largest contributor by at least a factor of six. Ordódy [107] stated in a study of the thermal conditions in the Budapest Metro that 75% of heat gains were a result of train traction equipment—acceleration and braking—and 25% from all other sources. Botelle et al. [23] state that 80% of the heat load is due to train traction.

2.3 Heat sinks

Heat is lost from underground railway tunnels and stations through ventilation, absorption into the surrounding soil or being carried out of the tunnels and stations in the mass of the train. The ventilation may be provided by the train induced air flows or mechanical ventilation systems. The effect of the soil heat sink will vary according to the tunnel and station air temperature and the temperature of the soil. In circumstances when the air temperature exceeds the soil temperature, during winter or during the night for example, the soil will act as a source of heat. According to Ampofo et al. [4], in a UK underground railway 30% of heat loss will be absorbed by the soil while 70% will be lost through ventilation.

2.4 Thermal conditions

The thermal conditions in an underground railway are a complex phenomena, varying in space and time, both diurnally and between seasons. The influence of the various sources and sinks of heat will determine the thermal conditions at a particular time. Generally, the operation of an underground railway will result in the raising the temperatures of tunnel and stations above ambient conditions due to the significant heat loads present in relatively small underground spaces. The New York City Transit Authority state that the operation of an underground railway raises temperatures in tunnels and stations by around 8–11 °C [105].

The Subway Environmental Design Handbook [127] presents a temperature profile along a typical underground railway tunnel found using a numerical simulation to show the effect the operation of an underground railway and the ventilation on tunnel and station temperatures. The typical underground railway includes stations, draught relief (B) and ventilation shafts (V) and tunnel portals (P). Ventilation shafts are positioned between stations to provide tunnel ventilation, while draught relief shafts are positioned just outside of the station to reduce the high air velocity of the piston effect on the station environment. The simulation consisted of 8 carriage underground trains, equipped with air conditioning, operating with a headway of 90 s. The profile is shown in Figure 2.2, where ambient temperature conditions were 24 °C.

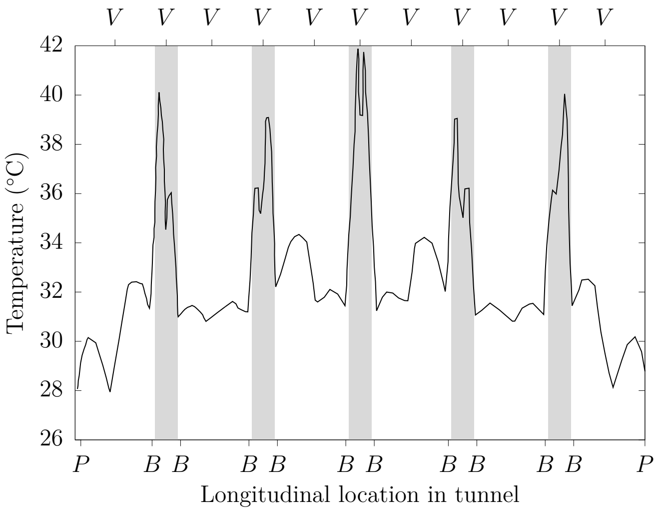

Figure 2.2: Underground railway average temperature profile in a typical underground railway [127].

The temperature in the stations, indicated by the shaded regions in Figure 2.2, is significantly higher than in the adjacent tunnels. This is a consequence of the large heat load dissipated in the stations due to train braking. The effect of the draught relief and ventilation shafts can be seen, resulting in a drop in temperature at each location. The station in the mid-point of the tunnel is warmest due to being furthest from the tunnel portals. Pope et al. [113] carried out a similar numerical study and found comparable temperature patterns.

Abi-Zadeh et al. [2] collected temperature data in the Kings Cross St Pancras Underground Station in London over a period from August 2001 to December 2002, between 5–6 pm in the evening. The temperatures were recorded on shallow and deep level platforms and the ambient temperature was also collected. The results are shown in Figure 2.3.

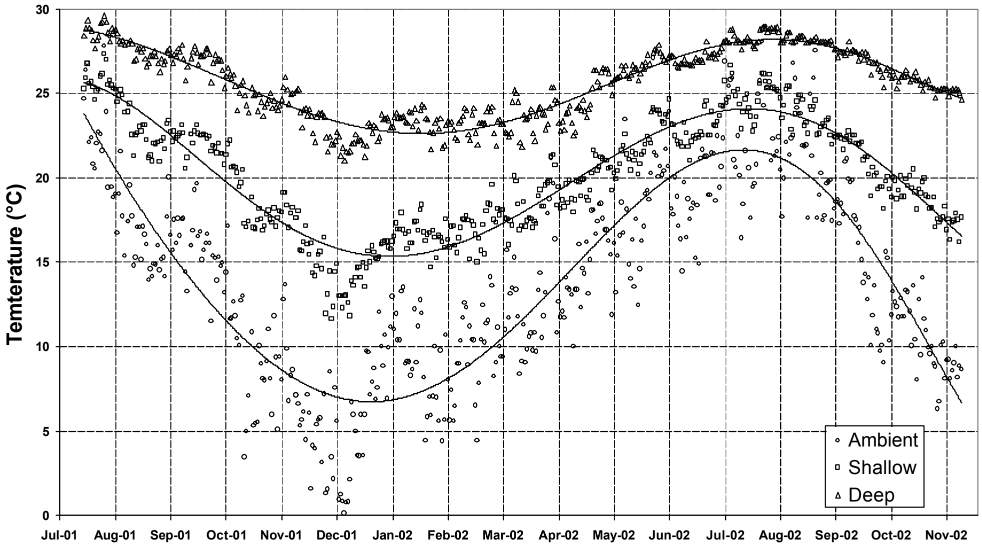

Figure 2.3: Evening peak hour temperatures for ambient and shallow and deep level platforms [2].

There is a clear sinusoidal shape to the temperature patterns due to the seasonal changes in ambient temperature. The peaks and troughs of the temperatures trends are later for the shallow and deep level platforms as the effect of ambient temperature changes is moderated by the inertial effect of the thermal mass of the surrounding soil. The temperatures on the deep level platform are significantly higher than the shallow level, with a minimum of around 23 °C and 15 °C, respectively, and 7 °C for ambient conditions. As the ambient temperature decreases the difference between ambient and platform temperature increases. The range of temperature variation on the deep level platform is smaller than on the shallow level due to the thermal mass of the soil and the dissipation of large amounts of heat into small station volumes compared with the shallow stations.

Ordódy [107] conducted a long term study of the thermal conditions in the Budapest Metro to investigate the thermal comfort in stations and the effect of ventilation. Temperature, relative air humidity and air velocity data were collected in several deep level stations, generally located at depths of around 20–30 m. Figure 2.4 shows the air temperature at two stations over a 22 hour period in the concourse area and left and right platforms and the outdoor ambient temperature, during the winter season.

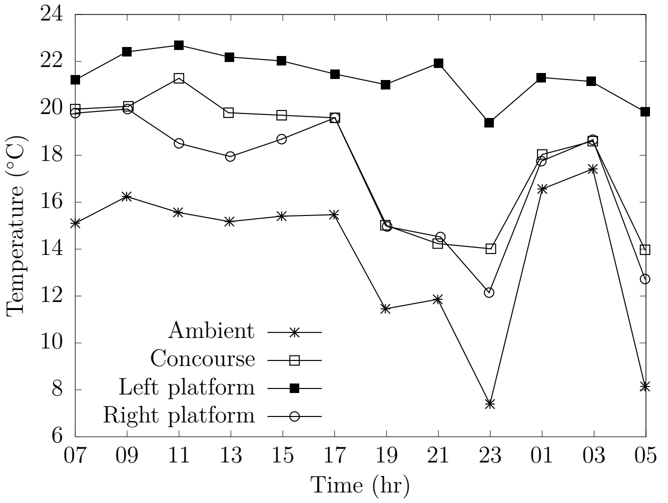

(a) Klinikák station.

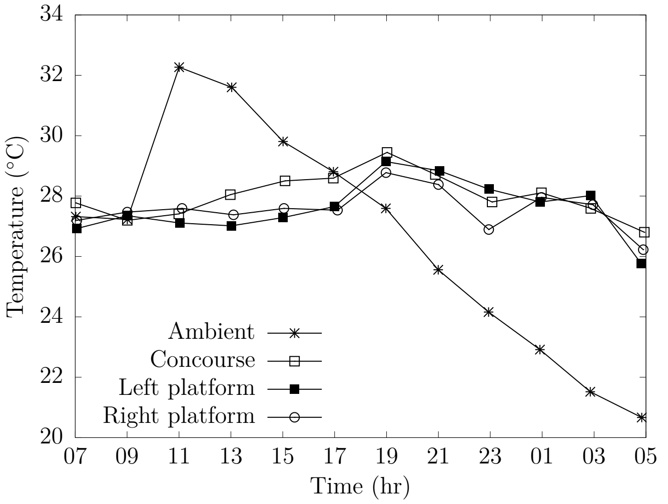

(b) Déli pu station.

Figure 2.4: Air temperature over a 22 hour period in two underground stations in Budapest [107].

The underground temperatures at Klinikák station generally follow the ambient condition, but at a higher level. The temperature on the right platform (II) responds to changes in the ambient condition more moderately than at the other locations.

The temperatures at Déli pu station are significantly higher than at Klinikák station and do not respond to changes in ambient conditions. These differences are due to the different ventilation systems in operation at the two stations, the system at Déli pu station being considered inadequate by the author. An annual fluctuation of ambient temperature of 30 °C was found compared with a fluctuation of around 5 °C for underground temperatures, similar to that observed in Figure 2.3, due to the inertia of the soil temperature, creating a delay of around 30 days. The author used the collected data to calculate the thermal comfort of passengers in Déli pu station using the commonly used predicted mean vote (PMV) and predicted percentage dissatisfied (PPD) approaches introduced by Fanger [44]. PMV calculates the predicted comfort vote using a subjective scale of subjective warmth, using air temperature, mean radiant temperature, air speed, humidity, metabolic rate and the insulation of the clothing as inputs. The calculated PMV values were found to indicate that thermal conditions were slightly warm and slightly cool in summer and winter, respectively. The PPD, a prediction of the number of dissatisfied people, was found to be between 5-30% but peaked at around 80% due to the piston effect during train arrival. The maximum PPD was found to be 90%, a very high value but can be considered realistic due to the very large heat gains due to train braking in stations.

Transit Development Corporation [127] proposed a thermal comfort index, the relative warmth index (RWI), the only attempt to consider thermal comfort in an underground railway environment. The RWI is a subjective index calculated from the vapour pressure of water, insulation of the clothing, insulation of air boundary, air temperature, mean incident radiant heat and metabolic rate. The index attempts to distinguish between different parts of the underground environment and a warmth level can be expressed for a variety of activities and conditions. The use of this index has been limited, but Abbaspour et al. [1] applied it to the study of thermal comfort in the Tehran Metro, Iran.

Ampofo et al. [3] reviewed the limited research in the area of thermal comfort in underground railway. The authors highlight the great difficulty in defining what ‘acceptable’ thermal comfort criteria in an underground railway. The challenge is due to that the criteria used to define thermal comfort are the same as the methods used to control the underground environment. Moreover, factors which effect the underground environment will change significantly over the period of a journey, whether long or short—for example, the heat load, air velocity, ambient conditions and number of passenger present. In contrast to an office or home, Ampofo et al. [3] proposed that a higher than normal PPD of 40–50% is acceptable as passengers spend a short amount of time in the underground environment. A PPD of 45% equates to a dry bulb temperature of 28 °C, a relative humidity of 70% and an air velocity of $0.15\,\mathrm{ms}^{-1}$. However, this is not true for members of staff working in the underground railway, who will spend extended periods of time in such an environment. Ampofo et al. [3] also considered the difference between newer and older London Underground stations finding that in older stations temperatures were in the range 20–27 °C while the range in an older station was 27–30 °C. Additionally, 96% of passengers were satisfied with the thermal conditions in the newer stations, 63% of passengers found the older stations uncomfortable.

Jenkins et al. [74] considered the prospects for thermal comfort on the London Underground up to the year 2050, particularly in the context of climate change. The authors found that without adaption the almost total dissatisfaction will be seen. It is suggested that saloon cooling for certain deep line could reduce the PPD by between 36% and 41% in 2050 conditions, but that further infrastructure improvements will be required.

Katavoutas et al. [81] considered the thermal comfort on the Athens Metro using the PMV and PPD indices, in trains and on platforms. The temporal behaviour of the PMV was presented for a deep and shallow stations shows that the index rises throughout the day. The PMV in the deep station is around 0.9 lower than for the shallow station, as the effect of the outdoor temperature is stronger. Additionally, increasing the air velocity is found to decrease the PMV up to a air temperature of around 33.7 °C, after which the PMV is found to increase.

Pope et al. [113] carried out a numerical study of a hypothetical twin-tunnel underground railway. The authors noted that temperatures varied closely with the pattern of train operation. A decrease in traffic from 30 to 20 trains per hour caused the temperatures to drop by around 1.5 °C. Additionally, the highest temperature occur in the evening peak due to high traffic levels and the air being at a relatively high temperature.

Han et al. [54] carried out a series of temperature measurements combined with passenger interviews to investigate the thermal comfort on the Seoul Metro. It was reported that 87% of passengers said they felt thermal conditions were ‘neutral’ or ‘comfortable’. The temperature on the platform was found to be at least 1 °C higher than the concourse temperature, during summer, autumn and winter. The difference between the platform and concourse temperatures was higher for autumn and winter, compared with the summer season, due to the cooler outdoor temperatures.

The climate and season of the area in which a underground railway is located, as well as the design, will influence the underground thermal conditions. In temperate climates, acceptable conditions can usually be maintained though ventilation with air from the outside environment. This will be sufficient except when weather conditions are unusually hot. Deeper underground railways usually have higher temperatures due to the greater distance which ventilating air must pass, whereas tunnels close to the surface may have a higher rate of ventilation. In climates with high outdoor temperatures it may be necessary to include mechanical cooling systems to maintain acceptable conditions. The increasing influence of climate change may prove a significant challenge to maintaining acceptable conditions in many underground railways around the world.

2.5 Environmental criteria

There are four criteria which must be considered in order to maintain an acceptable underground railway environment—air temperature, velocity, pressure and quality. These criteria are effected by climatic conditions, the operation of trains and the numbers of passengers in the underground environment, and therefore will vary significantly in space and time. The standards and requirements desired in an underground railway are set out by various organisations and the operators themselves. Air temperatures must not be too high as to cause a danger to health or significant discomfort. Air velocities must not cause discomfort or danger to people or objects being blown onto tracks. Air pressures should not be excessive to cause harm to people. Air quality should be sufficient to meet passenger physiological needs.

Environmental design criteria for underground railways are dispersed within a variety of sources. ASHRAE [15] recommends that the fresh air supply in waiting areas, in trains and on platforms should be at a rate of $8\,\mathrm{Ls^{-1}}$ per person, the same as recommended by CIBSE [32]. No particular standards are given by CIBSE [31] for tunnel ventilation, but reference is made to the industry regulator. ASHRAE [14] references the Subway Environmental Design Handbook [127].

Criteria for temperatures and air velocities in stations come from a variety of these references and HM Railway Inspectorate [64] and London Underground Limited [96] in a UK context. For ambient temperatures less than 20 °C station air temperatures must not exceed 25 °C; for ambient temperatures in the range 20–30 °C station air temperatures must not be 5 °C above ambient conditions; and for ambient temperatures above 30 °C station air temperatures must not exceed 35 °C. Station air velocities must not present a safety risk to passengers in stations, which should not exceed $5\,\mathrm{ms^{-1}}$.

Guidelines also specify air pressure conditions. Pressure should not exceed 3 kPa or 0.45 kPa if occurring at regular intervals of less than 10 s. Pressure transients should not exceed $400\,\mathrm{Pas^{-1}}$.

2.6 Ventilation and cooling

The heat generated due to the operation of trains in an underground railway must be removed to maintain temperatures within acceptable limits. Failing to maintain a comfortable environment may reduce the attractiveness of an underground railway as a mode of transport to the public and limit the capacity to operate trains at a desired frequency. Figure 2.5 shows a typical ventilation configuration around a single station.

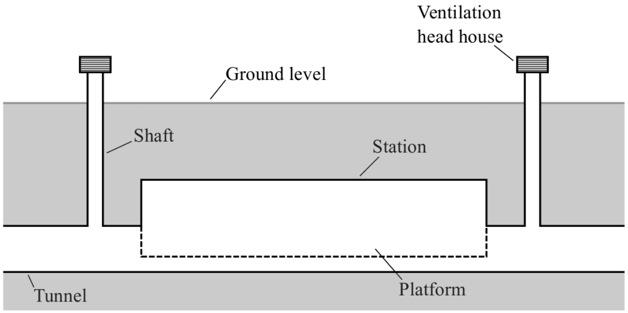

Figure 2.5: Typical ventilation configuration in a contemporary underground station.

During normal operation, adequate ventilation can often be achieved using ventilation shafts, with the air exchange provided by train induced air flows. In congested or emergency operating conditions, mechanical ventilation, often located in the stations, will provide the air flows. In warm climates, mechanical ventilation may also be required during normal operations.

The primary source of heat in an underground railway is the train braking. In a contemporary underground railway, the braking heat is extracted from the underground environment at source. This is achieved using over track (OTE) or under platform exhaust (UPE), shown in Figure 2.6.

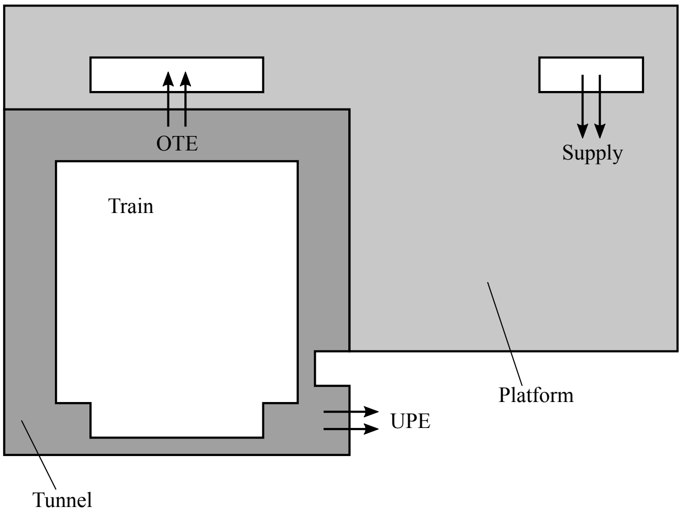

Figure 2.6: Typical air supply and extract in a contemporary station.

The architecture of a contemporary underground railway will also differ significantly from older examples. The trend previously was the construction of small, confined spaces. In a modern system, stations tend to be far larger and more open.

This characteristic is important for ventilation and thermal management. Small stations increase the density of dissipated heat [2] and narrow and sinuous passages hinder ventilation, while larger, more open, stations decrease the heat density and improve ventilation [22].

The design of a ventilation system for an underground railway will be constrained by various other requirements. The depth and geometrical configuration of stations, length of air shafts and length of the tunnels connecting stations will be determined by the characteristics of the system and surrounding development. Additionally, the costs of constructing ventilation infrastructure, such as air shafts and tunnels, may be considerable as will the operation of mechanical ventilation or air conditioning.

Ampofo et al. [5] used a mathematical model [4] to investigate the effect of various methods of cooling on tunnel temperatures. Imposing a speed restriction by reducing the maximum train velocity from $17.5\,\mathrm{ms}^{-1}$ to $12\,\mathrm{ms}^{-1}$ reduced tunnel temperatures by 2 °C and to a PPD of 66%. As many underground railways operate at high frequency, such a reduction in maximum speed would be very difficult to implement. Reducing the weight of the rolling stock by 50% gave a PPD of 59% but would also prove difficult to achieve in practice. During rheostatic braking the kinetic energy of the train is converted into electrical energy which is then dissipated, through resistors, as heat. In regenerative braking the electricity instead is use to perform a function, through feeding it back into the power system or storage in the train, thus reducing dissipated heat. If 70% of kinetic energy is converted to useful electricity then the authors found that tunnel temperatures would reduce by around 2.5 °C. The proportion of kinetic energy converted to useful electricity depends on the electrical transmission system, third rail or catenary, the current, AC or DC, the electrical substations and the train operational pattern [52]. The particular combination of system characteristics will influence the proportion of kinetic energy converted to useful energy. Assuming that 70% of kinetic energy can be converted into useful energy may be optimistic, Gelman [47] reported that in a particular scenario 40% could be recovered in an AC system. The impact of altering the thermal conductivity of the soil using heat pipes, simple devices for the transfer of heat [28], was also considered. It was found that increasing the thermal conductivity of the soil reduced the temperature by around 12% but that this would require 2500 heat pipes per kilometre of tunnel. This concept was also investigated experimentally by Thompson et al. [125]. Increasing the ventilation fan capacity by a factor of 10 was found to reduce temperatures by 12–18% but such a fan capacity is very large, and would present practical problems in implementation. Groundwater cooling was also investigated and was found that 50 kW of cooling per kilometre of tunnel would give a PPD of 58%.

Revesz et al. [116] have carried out a review of work relating to heat recovery from underground railways, extending the concept to heat recovery from the soil surrounding the tunnels. The authors suggest that ground source heat pumps could be used to exploit heat in the soil as a year round source of heat.

Ampofo et al. [6] monitored the application of a groundwater cooling system in Victoria Station, UK. Groundwater cooling utilises the relatively cool water in the surrounding soil for the purposes of underground cooling. The system was compared with vapour compression cooling and was found that the operational cost of groundwater cooling is three times less per unit of cooling and the CO_2 emissions four times less. However, the cost of the borehole required for such a cooling system would be significant.

Di Perna et al. [40] carried out an experimental investigation in a underground railway station in Barcelona, Spain, to study the ventilation of the station. The experimental results were combined with numerical simulations and statistical analysis to develop a methodology to estimate the flow rates through station passages using only a few point measurements. The authors showed that if velocity and pressure data was collected at points in a station in real time, then estimations of air flows could also be made. The authors suggest that with such real time information, the mechanical ventilation systems could be controlled to work with train induced air flows and underlying air flows, rather than in conflict.

Pflitsch et al. [111] also studied the conflicts between mechanical ventilation and underlying air flows. A series of velocity and temperature readings were made during the night in Monument Station on the Tyne and Wear Metro in Newcastle, UK. The authors noted that there was a significant underlying air flow created by the characteristics of the tunnels and station and the climate, independent of mechanical ventilation or the movement of trains. The effect of turning off mechanical ventilation was shown to reduce temperatures in the areas where measurements were carried out. This indicates that the mechanical ventilation systems were poorly thought out and that if the underlying air flows were considered, then energy savings could be made.

Gonzalez et al. [51] considered the ventilation of an underground railway complex using mechanical and train induced ventilation. A series of numerical simulations were carried out with various mechanical ventilation operating scenarios, including no mechanical ventilation. The effect of train induced air flows was compared with mechanical ventilation where it was found that the peak flow rate induced by the train may be as high as 50% of that provided by mechanical ventilation. As a proportion of total mechanical ventilation the train induced air flows may provide between 2.1-3.0% of the air flow. The authors suggest that ventilation systems may be designed to account for the presence of train induced air flows.

Huang et al. [70] investigated numerically the effect of using solid curtains within a underground railway tunnel to increase ventilation through ventilation shafts. The proposed curtains would consist of solid partitions used to block the tunnel and divert air flows through ventilation shafts. The curtains would be raised and lowered to allow the passage of a train. The authors considered a tunnel consisting of two ventilation shafts and two curtains which isolated the region of the tunnel containing the two shafts. It was found that the air flow suction and exhaust through the shafts was 125.7% and 697.5% and 95.0% and 123.9% of the case without curtains, respectively. The curtains also reduced the suction and exhaust of air from the two stations and the ends of the tunnel. The increase in air flow through the ventilation shafts may reduce high velocities in the stations and improve air exchange with the ambient environment. However, the effect may also reduce the ventilation in the stations. How such a system of solid curtains would work in practice, and in a safe manner, is a practical challenge.

Huang et al. [71] carried out a validated numerical investigation of the effect on ventilation flow rates of the arrangement of ventilation shafts. The number of ventilation shafts was increased while keeping the total area of the shaft openings constant. An increase in exhaust air flow of around 31.2% was found for a configuration consisting of six air shafts while having a negligible effect on the suction air flow. The authors also found that increasing the distance between the location at which the train starts moving and an air shaft results in a greater exhaust air flow and reduces the suction.

Jia et al. [75] considered the air flows within an underground railway station during the arrival and departure of a train. The authors highlighted the air distribution within the station region, in particular the behaviour of air flows through the air shafts and exits. In particular, the effect of ventilation shafts on increasing air exchange between the underground and ambient environments was highlighted, but was also noted that this would reduce the piston effect in the station.

Juraeva et al. [76] investigated the effect of installation location of a mechanical ventilation shaft upon ventilation performance, using a validated numerical model. The authors also investigated the effect of guide vanes and air curtains on the performance of the mechanical ventilation shaft. Two locations were investigated, on the top of the tunnel and at the side of the tunnel. The air flow through the mechanical ventilation shaft was found to be higher when located at the top of the tunnel, and the performance was further enhanced by the use of an air curtain. The study investigated the two locations using one model so the effect of one shaft location may have effect the performance of the other, thus it is unclear if any firm conclusions can be drawn from this work.

Juraeva et al. [77] investigated the optimum location for the installation of a air curtain within a tunnel equipped with natural and mechanical ventilation shafts. Without investigating the air curtain itself, but by analysing the air flows and pressures the authors recommended that an air curtain should be installed between the mechanical and natural ventilation shafts. However, it is unclear what metric was being considered to arrive at this conclusion. Juraeva et al. [78] investigated air curtains further finding that their use can improve air flow into mechanical ventilation shafts.

Pope et al. [113] studied numerically the factors effecting draught relief and air temperatures in an underground railway system. The authors carried out a parametric study of the cross sectional area, length and location of draught relief shafts finding that the cross sectional area should be around $20\,\mathrm{m}^2$, a longer shaft increases the largest mean air flows significantly in escalator shafts and that shafts should be located close to stations to minimise peak air velocities in stations. The authors found that temperatures were dependent on the pattern of train traffic. The highest temperatures were found to be during the evening peak period, due to the dissipation of heat from braking trains, which then drops towards the end of operations. During the night, temperatures increase when there is no traffic due to the lack of train induced air flows providing ventilation.

Abi-Zadeh et al. [2] carried out field measurements and numerical simulations of Kings Cross St Pancras Underground Station, London, UK to study the thermal conditions as part of the design for ventilation in an upgraded station. The authors found that the train induced air flows are sufficient for the provision of fresh air for physiological requirements. Temperatures in underground railways can generally be maintained at reasonable temperatures, especially in a temperate climate as in London. This is the case on the Jubilee Line Extension, where sufficient ventilation shafts were provided to maintain acceptable conditions [22]. The train induced air flows are found to be sufficient for temperature control in most circumstances in the original and redeveloped station, although temperatures in the developed station have a stronger relationship with ambient conditions. In particular, the increased traffic in the redeveloped station resulted in a higher heat load, but this was counteracted by higher ventilation air flow from the train induced air flows. The authors conclude that some areas of the station will suffer from high temperatures and as such additional cooling in these locations would be required.

Ke et al. [82] studied the influence of the train induced air flows, under platform exhaust ducts and draught relief shaft upon underground railway temperatures and ventilation, in Taipei, Taiwan. The dimensions of draught relief shafts were investigated where it was found that increasing the length from 40 m to 100 m would reduce air flow by 15–25% and when the cross sectional area is increased from 15 m^2 to 30 m^2 the air flow will increase by 40%. Thus if an air shaft needs to be longer due to design constraints then the cross sectional area could be increased to maintain air flows at the desired level. The under platform exhaust ducts are found to reduce temperatures significantly, reducing the station and tunnel temperatures from 46.6–48.8 °C to 38–39 °C for a exhaust rate of 30 $\mathrm{m}^3\mathrm{s}^{-1}$ and below 37 °C, the required temperature, for a exhaust rate of 40 $\mathrm{m}^3\mathrm{s}^{-1}$. The influence of train induced air flows on underground temperatures was investigated in terms of the maximum speed of the train. With a maximum speed of 80 kmh^{-1} the temperature in the tunnel is around 1–2 °C higher than for a maximum speed of 60–70 kmh^{-1}. This is due to a higher heat load at 80 kmh^{-1}, which it too great to be counteracted by stronger train induced air flows. For a maximum speed of 20 kmh^{-1} the temperatures will rise due to far weaker train induced air flows.

Pope et al. [113] also investigated the use of under platform exhaust ducts. In tropical climates, they found that temperatures reduced from 50.5 °C to 42.5 °C and 44.5 °C to 36.5 °C in tunnel and concourse regions, respectively, for an air flow of 40 $\mathrm{m}^3\mathrm{s}^{-1}$. In temperate climates temperatures reduced from 44.5 °C to 36.0 °C and 38.0 °C to 31.0 °C in tunnel and concourse regions respectively for a air flow of 40 $\mathrm{m}^3\mathrm{s}^{-1}$. Further increases in air flow rate gave diminishing reductions in temperatures.

Eckford & Pope [42] investigated increasing the ventilation rate in tunnels by 60%, from 316 $\mathrm{m}^3\mathrm{s}^{-1}$ to 500 $\mathrm{m}^3\mathrm{s}^{-1}$. This could be achieved using mechanical ventilation, train induced air flows or ventilation or draught relief shafts. It was found that temperatures would be reduced by around 4 °C. Increasing the ventilation rate further was found to give limited additional temperature reduction.

Kim & Kim [86] evaluated the effect of ventilation shaft location on ventilation efficiency. Ventilation efficiency was defined as the proportion of the tunnel volume which is displaced through the air shaft due to the passing of a train. Four ventilation shaft locations were investigated. A ventilation shaft located just before the train started to decelerate was found to give the highest efficiency, resulting in around 36% of the tunnel volume to be displaced through the ventilation shaft, 7.3% better performance than the worst location. The location which performs best is due to the train having the longest travelling distance before the ventilation shaft, and before deceleration begins. The authors also found that the ventilation shaft closest to the station minimised the highest air flows in travelling into the station region. Huang et al. [69] carried out a similar study.

Krasyuk & Lugin [89] carried out field measurements of pressure and velocities in the Novosibirsk Metro, Russia. The carried out measurements in a tunnel between two stations, which the authors referred to as a station-to-station block, which are never more than 20 m deep. It was found that train movement outside of the block had negligible effect on the pressure and air velocity within the block. Train movement within the block created air flows, which decay slowly once the train has left the block.

Krasyuk [88] further investigated the Novosibirsk Metro by considering the thermal conditions, the ventilation fan flow rates required to maintain particular conditions and the effect of train induced air flows. It was found that the air flow rate required is governed by the need to remove heat generated by trains, and is of the order of 85–90 $\mathrm{m^3 s^{-1}}$ for operation by 4–5 carriage trains. The authors also found that if the ambient air temperature exceeds 25 °C then the required flow rate increases significantly and the operating regime of the fans should be modified. The train induced air flows were found to be sufficient for maintaining the desired temperatures if the ambient temperature is 8 °C or less. However, for ambient conditions above this level, the train induced air flows still contribute to the reduction of underground temperatures, and the authors recommend that if attention is given to this in the operation of fans then energy use may be reduced.

Lee et al. [91] carried out field measurements of air velocities in ventilation shafts located between two stations on the Seoul Metro, South Korea. The air flows through the shafts were estimated numerically. It was found that more than double the volume of air was sucked into the tunnel as was exhausted out through the air shafts. Of the six ventilation shafts separating the stations, the two shafts adjacent to the station have lowest air flow, either suction or exhaust, and the exhausted air flow is larger that the suction. The largest air flow is in the central shafts after the train has accelerated and before deceleration has begun.

Gerhardt & Krüger [48] carried out scale model testing of Potsdamer Platz Station in Berlin, Germany, in order to evaluate the effect of train induced air flows on passenger comfort. In order to reduce discomforting air velocities, the use of surge openings—or draught relief shafts—was evaluated and found to reduce air velocities to safe levels, of around 0.5–$1\,\mathrm{m\,s^{-1}}$.

Lin et al. [93] carried out a series of field measurements of temperature and air velocity in draught relief shafts on the Taipei Subway, Taiwan. Additional numerical analysis was carried out to investigate the effect of shaft length and cross sectional area on air flows. The train induced air flows were found to induce air exchange between the tunnels and ambient environment due. The passing of a train causes a cycle of exhaust and suction in the shaft, and a drop in the temperature in the shaft due to the intake of cooler ambient air. The authors introduced a concept of piston effect efficiency, η_{PE}, which compares the air flow in the shaft with the length of the shaft, to measure effectiveness of the air exchange. It was found that a shaft length of $60\,\mathrm{m}$ was required for effective air exchange. The authors claim that increasing the cross sectional area of the shaft will not increase the air exchange as the travelling distance of the air will decrease, however, reducing the shaft cross sectional area will improve air exchange.

Wang et al. [137] combined field measurements, theoretical wall jet theory and scale model testing to study the train induced air flows in underground stations. A wall jet is a jet of air moving along a wall into a larger volume with an open boundary on the side opposite the wall [79]. In the context of an underground railway, the larger volume is the station, the open boundary is the platform and the wall is the wall of the tunnel into the station. Wall jets have two layers; an inner layer which behaves like a viscous boundary layer and an outer layer in which turbulence dominates. Additionally, wall jets have three distinct regions in the direction of the flow, potential core, transitional and fully developed regions. A sketch of a wall jet and the flow regions is shown in Figure 2.7.

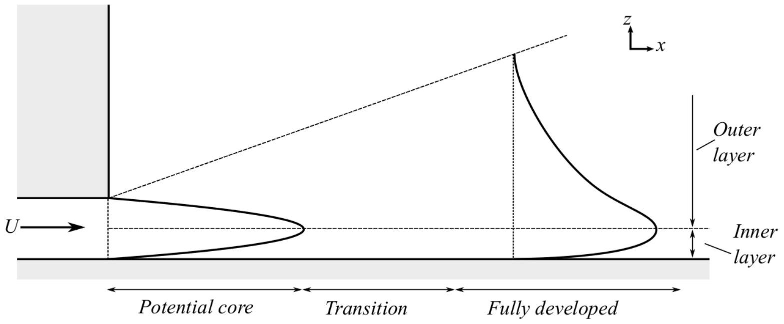

Figure 2.7: Sketch of a wall jet and flow regions.

The authors describe the train induced air flows in the context of wall jets, defining the initial stage of the flow in three parts; the potential core, boundary layer and free shear zone. The main section of the flow is composed of the free shear zone. The theoretical results are validated with field and model measurements. The results indicate that the potential core is contained within the width of the tunnel and the platform is contained within the free shear zone, meaning that the velocities on the platform are considerably lower than in the track area.

Xue et al. [143] carried out an experimental and numerical investigation of the air flows through draught relief shafts and on platforms in an underground station in Shenyang, China. In particular the area of the louvres located at the exits of draught relief shafts was investigated, finding that a large area decreased the wind discomfort on platforms.

Yan et al. [145] carried out another validated numerical investigation of the air flows in draught relief shafts induced by trains, in a station on the Shanghai Metro. The authors evaluated the impact of shafts in the arrival and departure tunnels, and in both. If a configuration was chosen to have only one draught relief shaft, being located on the train arrival side is found to give better air exchange efficiency, as was also found by Xue et al. [143]. While the net exhaust of air is similar for the two shaft locations the suction of air is considerably lower if the shaft is located after the station.

Yuan & You [149] presented the optimisation of the ventilation system in a station on the Tianjin Metro, China. A numerical model representing the air velocity and temperature conditions just as a train has arrived in the station. The model was validated using field measurements. The results show that the train induced air flows mostly influence the air velocity in the station before the access passages, located half-way along the platform. The highest average air velocity upstream of the access passages is around $0.7\,\mathrm{ms}^{-1}$ while it is $0.1\,\mathrm{ms}^{-1}$ downstream of the passages. This velocity characteristic causes high temperatures in parts of the station. The authors investigated the optimisation of the mechanical ventilation systems to address regions of high temperature.

Moreno et al. [102] carried out field measurements to investigate the air quality in stations on the Barcelona Metro. In narrow single track platforms, the train induced air flows are not sufficient to maintain acceptable conditions and so must be supplemented by mechanical ventilation. In contrast, in wider, double track stations, the air quality is found to improve without mechanical ventilation. A cyclical pattern in CO_2 concentrations is observed in stations due waiting passengers and the arrival of trains. Strong lateral variations in concentrations of particulate matter are observed, due to the unevenness of the effect of train induced air flows and on the position of access passages.

Mortada et al. [103] developed a validated numerical model of the Central Line, part of London Underground, and carried out a parametric investigation to consider the effect of soil temperature, traffic levels, regenerative braking and ventilation rate on tunnel and station temperatures. Removing the effect of mechanical ventilation is found to increase temperatures by between 2–3 °C. Increasing the standard ventilation rate by a factor of 4 is found to reduce temperatures by only around 1 °C. Regenerative braking of 20% efficiency is found to reduce temperatures by 2 °C and 40% efficiency by a further 1 °C. As it is expected that future traffic growth will be significant, such temperature reductions will be required just to maintain current conditions.

2.7 ENERGY DEMAND REDUCTION

An underground railway is a large consumer of energy, for both traction and non-traction requirements. London Underground is the largest electricity consumer in London, and one of the ten largest in the UK [128]. Casals et al. [27] reports that between 30-50% of energy consumption in underground railways is due to non-traction requirements. In the Barcelona Metro the ventilation is found to account for 14% of station energy demand.

Hong & Kim [65] surveyed the energy consumption in a subway station in South Korea. They noted that the energy demand correlated with the numbers of passengers due to the use of air conditioning systems. The energy consumption also depends strongly on the age of the station with stations built in the 1970s using double the energy of the most recently constructed.

Anderson et al. [8] surveyed the potential for reductions in energy consumption in underground railways. The authors state that in Asia, 20% of underground railway operating costs are attributable to energy and around 5-10% in Europe and North America. It is suggested that regenerative braking systems and automatic train operation to improve train operation, have the most potential for reducing energy demand.

Di Perna et al. [40] investigated a method of estimating in real time the air flows in an underground railway. Such a system could allow for the dynamic control of mechanical ventilation systems according to the behaviour of air flows. This in turn could be used to reduce the use of mechanical ventilation when non-mechanical ventilation is sufficient, thus reducing energy demand.

Ansuini et al. [9] outlined work carried out as part of the Sustainable Energy Management for Underground Stations (SEAM4US) project, the aim of which was to reduce underground station energy demand through the advanced control of ventilation systems. The basis of the advanced control system is the use of sensors to monitor the environment so that the ventilation systems may be controlled optimally, and in an anticipated fashion. As part of the development of the control system, numerical modelling of the Passeig De Grácia metro station in Barcelona was carried out using computational fluid dynamics to evaluate the effects of the outside environment and train induced air flows on the station environment. It was found that for 85% of the year these air flows are relevant to the conditions in the station. Additionally, it was found that for 40% of this time, the air flows work against the mechanical ventilation systems, a scenario also observed by Pflitsch et al. [111]. The results from the numerical modelling are used in the development of a predictive control algorithm. Vaccarini et al. [131] presented the predictive control algorithm which controls ventilation systems together with station sensors, weather forecasts, train and mechanical ventilation schedules and passenger monitoring. An energy demand reduction of 30% is realised while maintaining thermal conditions in the station.

Lee et al. [92] developed a predictive model of indoor air quality and ventilation energy demand based on the outdoor air quality. The prediction model was based on the partial least squares approach and improved prediction accuracy by 20% for PM concentration on the platform and 64% for the energy demand. The authors suggest that the model could be used to maintain indoor air quality while reducing energy demand, in a similar way as shown by Vaccarini et al. [131].

Liu et al. [94] optimised the control of ventilation control systems in a station on the Seoul Metro to maintain air quality and reduce energy consumption. A model predictive control was developed accounting for the ventilation fan speed, outdoor particulate matter levels and train schedule. A multi-objective optimisation was used to determine optimal set points for the ventilation fans. The optimised system improved indoor air quality and reduced energy demand by 24%.

Ono et al. [106] also considered the optimisation of control and found that for the majority of the day train induced air flows were sufficient for maintaining thermal conditions. Mechanical ventilation was found to be needed only for short periods of time.

Gonzalez et al. [51] carried out a numerical investigation of the train induced ventilation of a underground station. The ventilation provided by train induced air flows was compared with that from mechanical ventilation. The train induced air flows are found to provide an instantaneous flow rate of 50% of the mechanical ventilation. Over longer periods it is found that the train induced air flows amount to at most 3% of the mechanical ventilation air flows. The authors suggest that if mechanical systems accounted for these air flows, energy savings of a similar order could be achieved.

Marzouk & Abdelaty [100] applied building information modelling and wireless sensor networks in the Cairo Metro to reduce the energy demand in underground stations. The wireless sensor network is used to measure the temperature and humidity in stations and the building information model is used to monitor the thermal conditions. This allows the identification of regions of stations with unacceptable thermal conditions and the prediction of thermal conditions therefore allowing more efficient control of ventilation systems.

Khalil et al. [83] carried out an experimental and numerical investigation of thermal conditions in a station on the Cairo Metro, which extended the work of El-Bialy & Khalil [43]. Experimental measurements were used to validate numerical simulations, which accounted for the heat load of passengers and trains. Applying a task dependent air conditioning system is found to maintain thermal conditions but reduce energy demand.

Platform screen doors (PSD) are used to separate the tracks in an underground station from the platform areas. A PSD has two purposes; to stop passengers being able to access the tracks and to reduce the effect of train induced air flows on the platform environment. It may be desirable to reduce effect of the train induced air flows on the platforms if the air flows may be too strong or that the platform may be air conditioned and as such would be preferable to isolate the environment from the higher temperature air of the tunnel.

Hu & Lee [68] investigated the effect of PSDs on energy consumption in a station on the Taipei Metro. The peak cooling load is found to be reduced by around 50%

due to the use of PSDs. However, with the PSDs UPEs are used to remove heat from the tunnel and as such negligible difference is found with or without using PSDs. This is due to the UPEs operating at all times, which if optimised could reduce energy demand further.

Yang et al. [146] investigated numerically a system to combine the benefits of PSDs with the ventilating effect of train induced air flows. Controllable slits were incorporated into the PSDs which allow air flow through the PSDs. It is shown that the train induced air flows are sufficient for ventilation, and if utilised may reduce the energy demand from mechanical ventilation and cooling. A system to control the PSD controllable slit, cooling systems and mechanical ventilation was investigated and found that maximum energy demand reductions of around 30% could be achieved.

2.8 The piston effect

Train induced air flows—also known as the piston effect—are generated by the movement of trains in tunnels. As a train passes through a tunnel, the air around it can only move ahead or behind the train. The constraining effect of the tunnel walls generates a pressure gradient along the length of the train, with high pressure at the front and low pressure at the back. The magnitude of the air flows in the tunnel, the drag on the train, and the pressures within the tunnel are dependent on the interaction of the train and tunnel, train-tunnel aerodynamics. For the purposes of underground railway ventilation, the magnitude of the train induced air flows are an important consideration. The factors which effect the behaviour of such air flows must be known in order to understand how they are generated and controlled.

The original approach to the investigation of the train-tunnel aerodynamics was to assume that for long periods the air flows in a tunnel are steady, which allows results to be deduced for resistance coefficients, air flows and temperatures [126, 122, 25]. This work was advanced in the 1960s during the development of Shinkansen high speeds trains in Japan. The Japan National Railways carried out a programme of research into drag and pressures produced by high speed trains in tunnels, and published a series of articles using experimental and theoretical approaches [55, 58, 56, 46, 59, 57]. The outcome of this work was the estimation of the aerodynamic forces on the train nose and tail, depending on the wall friction and experimental coefficients, from which a drag formula was derived. Additionally, a basic method for the calculation of pressure transients for trains is long tunnels was presented. Yamamoto [144] developed an unsteady, incompressible, solution for train induced air flows. The solution was produced using the method of characteristics within a computer program.

A large scale series of experimental tests were carried out by Developmental Science Inc. [37, 36, 39, 38]. The test facilities were used to investigate the flow of air through tunnels and stations, pressure, body forces and train speed. Parsons Brinkerhoff Quade & Douglas [108, 109] developed an analytical model and computer program for the design of subway systems based on an assumption of one-dimensional (1-d), unsteady, turbulent flow. The program provided air flow and train drag information. Additionally, Parsons Brinkerhoff Quade & Douglas et al. [110] carried out a series of tests in the Berkeley Hills tunnel, California, USA, measuring the pressure, temperature and air velocity. The data were used to validate the computer program. All this experimental and analytical work was brought together by the Transit Development Corporation [127] to form the Subway Environmental Design Handbook, and companion computer program [115]. This forms an industry standard guide and analysis tool for the design of underground railways.

As part of the experimental and numerical testing, the influence of the blockage ratio (β)—the ratio of the frontal cross sectional area of the train to the tunnel cross sectional area—was investigated in terms of the effect on tunnel air flow and train drag. The results presented in the Subway Environmental Design Handbook are shown in Figure 2.8 for different values of x_t/D_h, the ratio of the tunnel length (x_t) to hydraulic diameter (D_h).

Both the tunnel air flow and train drag show strong dependency on the blockage ratio. For longer tunnels the effect of drag is larger and the air flow lower, and vice-versa for short tunnels. For low blockage ratios the air flow is weak.

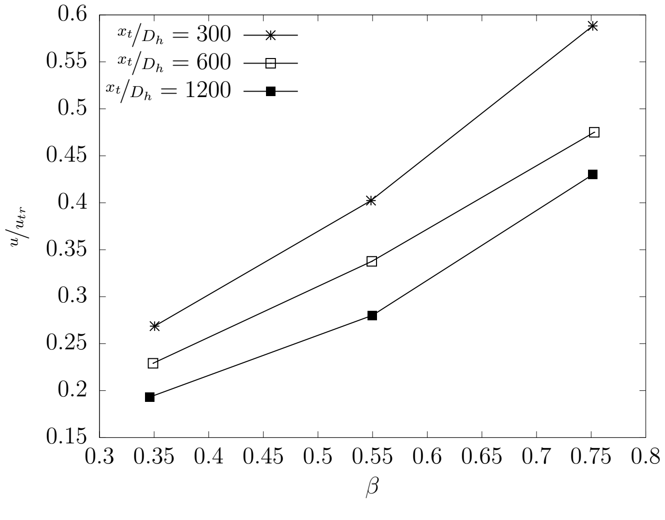

(a) Tunnel air flow.

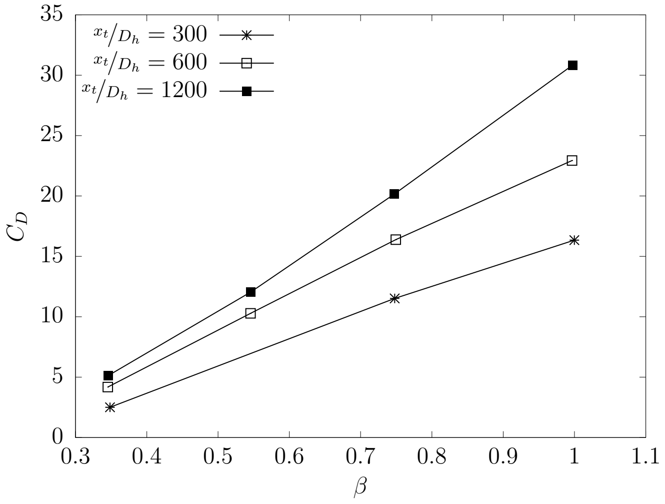

(b) Train drag.

Figure 2.8: Influence of blockage ratio on tunnel air flow and train drag for different x_t/D_h values [127].

Various other contributions were made to the topic over the following years. Henson [60] and Fox & Henson [45] developed a method of of directly calculating the pressure history of a train passing through a tunnel. A one-dimensional, unsteady, compressible formulation of fluid momentum, continuity and energy equations were solved using the method of characteristics and solved using computers. Agreement was found between the results and laboratory tests. Woods & Gawthorpe [140] investigated the same problem but used a less direct method. Henson & Fox [61, 62] expanded the scope of the model to deal with larger complexes of tunnels and stations, applying the method to the design of the Channel Tunnel. Higton [63] presented a generalised version of the program for application to any train-tunnel configuration, with validation from field measurements. Woods & Pope [141] presented a generalised flow prediction model which accounted for friction, tunnel cross sectional area change, heat transfer, locomotive heat release, vehicle leakage, and gravity body forces. Vardy [132, 133] carried out a series of field measurements on the Victoria Line, London, UK, to validate the model presented by Higton [63]. A sensitivity analysis was carried out to determine the relative importance of various system parameters, with skin friction found to be of particularly significant.

The drag on a train is a property of the overall train-tunnel configuration and not a result of one part [118]. Vardy [134] synthesised much of the work on the aerodynamics of trains in tunnels and outlined the main contributions to train drag. In the open air, the main contributions to train drag are from skin friction and pressure drag or form drag. The skin friction is often the most important. Due to the growth of the boundary layer, the skin friction varies along the side of the train. Pressure drag is, in the simplest case, the difference between the pressure forces on the front and back of the train. Due to flow disturbances and the boundary layer separation at the front and back of the train, the pressure at the back will be lower than at the front. Pressure drag is defined as the sum of all longitudinal components of all pressure forces on the train surface and the skin friction drag as the sum of all longitudinal components of all viscous shear forces on the train surface.

When the same train passes through a tunnel, the components of drag are altered. The presence of the wall alters the velocity gradient along the train, and thus the viscous shear forces are changed. The flow separations are constrained by the wall which reduces the pressure drag at the front of the train, and similar effects may occur at the back of the train. The train displaces air as it moves through the tunnel, which may pass alongside the train or down the tunnel in front of the train. In certain conditions—at high speed or high blockage ratio—this causes a rise in pressure, which contributes additionally to the pressure drag, which can be large. In a tunnel the boundary layer on the side of the train is constrained and so has an essentially constant thickness, but the pressure varies along the train. This results in a further contribution to pressure drag due to the pressure difference between the front and back of the train, even though it is a result of skin friction. Vardy [135] continued this work by making predictions of drag losses due to the changes in blockage ratio. Train skin friction was shown to vary linearly with blockage ratio and relationships for between separation losses and the blockage ratio were hypothesised.

Choi & Kim [29] carried out an investigation of the effect of the shape of a train nose, the blockage ratio and the train speed on total drag and the pressure and viscous, or skins friction, drag components. Doubling the speed from 100 $\mathrm{kmh^{-1}}$ to 200 $\mathrm{kmh^{-1}}$ is found to increase the total drag by a factor of 3.8. At 200 $\mathrm{kmh^{-1}}$ the pressure and viscous drag components account for 68% and 32% of the total drag, respectively. Lengthening the nose of the train to make the shape more streamlined is found to reduce the total and the pressure drag component significantly up to a length of around 4 m after which a longer train front has a diminishing effect on drag. The effect of a longer nose on viscous drag is not significant. The results are compared with the train in an open field and where it is shown that the viscous drag is more dominant. The blockage ratio is varied between 0.281 and 0.1 for a train with a nose length of 10 m. The viscous and pressure drag components are found to reduce simultaneously, and the total drag by a factor of 2.

Baron et al. [18] considered the effects of increasing the blockage ratio from 0.13 to 0.52 on the aerodynamic behaviour of a high speed train using numerical methods. The authors confirm what was found by Vardy [134] in that in the larger tunnel the effects of skin friction dominate the drag but not in the small tunnel. The effects of the blockage are small for the large tunnel, with the velocity ahead of the train, relative to the tunnel, being low. The blockage effect in the small tunnel are significant—the air ahead of the train generates high pressure at the train nose and the air flowing through the annular region, between the train side and tunnel wall, reaches sonic conditions at the back of the train. Various tunnel configurations are shown to reduce the effect of the blockage effects.

Baron et al. [17] investigated the generation of micro-pressure waves due to train entry into a tunnel. A compression wave is generated by a train entering a tunnel, which when they reach the opposite portal, are partly radiated outside as micro-pressure waves. The amplitude of the micro-pressure waves is found to have a quadratic relationship with the blockage ratio. As with the pressure rise at the entry of the train, the amplitude of the micro-pressure waves is determined by the blockage ratio and train speed. The initial gradient is determined by the shape of the train nose which, if lengthened, can be reduced.

Kim & Kim [85] investigated the train induced air flows generated by a subway train in a tunnel, using a scale model and computational fluid dynamics. Scale model testing was carried out by moving a geometrically simple train through a tunnel, while measurements of air velocity and pressure were recorded. The train was accelerated, moved at constant velocity then decelerated. The air velocity in the tunnel was found to reach a maximum of around 0.8 of the maximum maximum train velocity, for a blockage ratio of 0.65. The numerical results agreed with the experimental measurements reasonably well for the pressure readings, but with notable difference for the air velocity. There was no consideration of the applicability of the results to a full scale train-tunnel configuration. Camelli et al. [26] reproduced the work of Kim & Kim [85] using an immersed soil approach and a Large Eddy Simulation (LES) formulation. The results showed improved agreement with the experimental readings.

Rabani & Faghih [114] studied the effect of blockage ratio, train speed and nose shape on the pressure and drag during the entry of a train into a tunnel. The shape of the train nose is found to effect the rate at which the maximum pressure is reached, but not the maximum value. The blockage ratio is found to increase the maximum pressure by around a factor of 2 if it is increased from 0.185 to 0.242. For the same increase in blockage ratio, the drag increases by around 22%. Variations in train speed delays the time to reach maximum drag. Bellenoue et al. [19] found that the minimum pressure gradient depends on both the blockage ratio and the shape of the train nose. Auvity et al. [16] investigated the effect of a train entry on the unsteady air flows from a tunnel at train entry, finding that the shape of the train nose does not effect the mass balance, i.e. the ratio of compressed to exhausted air. Bellenoue et al. [20] carried out experimental tests of a train passing through a tunnel, and the influence of the generated pressure wave. It was found that while keeping the blockage ratio the same, different pressure gradients were generated depending on the cross section of the train. Shin & Park [119] found that the drag increased by a factor of 2.7 compared with the open atmosphere. Ko et al. [87] also found that lower blockage ratios reduced the induced pressures. Gilbert et al. [49] studied the pressure around high speed trains at tunnel entry.

Shuanbao et al. [120] developed an optimisation method using computational fluid dynamics to improve the aerodynamic properties of a high speed train passing through a tunnel. A reduction in the overall drag force of 3.34% was achieved. Muñoz-Paniagua et al. [104] also presented an numerical optimisation method to reduce the train nose pressure and drag.

Ricco et al. [117] studied experimentally and numerically the pressure waves generated by a high speed train travelling through a tunnel. The authors extended the one-dimensional models of train-tunnel systems by the addition of a separation bubble model, to account for flow separation at the train nose. The shape of the nose was investigated to assess the size of the bubble with different nose angles, finding that the bubble was not present for angles less than 30°. The bubble effects the magnitude of the induced pressure wave. The pressure rise at the train entry to the tunnel was investigated in terms of the train nose cross-sectional shape, while keeping the blockage ratio and nose shape constant, which was found not to influence the rise, as found by Bellenoue et al. [20]. Tunnel length was found to have a small effect on the pressure rise.

Gilbert et al. [50] studied the effect of blockage ratio and tunnel length on the air flows generated by a high speed train in a tunnel, using an experimental and numerical approach. An increase in the blockage ratio of 30% is found to increase the velocity in the train nose region by 40%. The air velocities in longer tunnels are shown to decay slower after a train has left the tunnel, as compared with a shorter tunnel.

Other areas of study in the context of the piston effect have included the investigation of tunnel hoods [101, 95, 130, 142] to mitigate the effect of pressure rises on train entry and perforated tunnel walls to achieve the same aim [67, 66]. Zhou et al. [152] investigated the pressure effects of a high speed train passing through a station. Khayrullina et al. [84] investigated the air gusts induced by trains passing through an underground station using a validated computational fluid dynamics model using an LES formulation. The effect of a passenger and a freight train are investigated and it is found that the freight train, because of the less aerodynamic shape, has higher velocities in the slipstream. Additionally, the higher blockage ratio and speed of the passenger train are found to result in higher wind speeds.

2.9 Discussion

The review of literature and research has covered a wide range of work relating to the thermal conditions in underground railways, methods of ventilation and cooling, the piston effect and methods to reduce energy demand.

Previous work has highlighted the large effect which the operation of an underground railway has on thermal conditions. The temperature of an underground environment is affected by ambient conditions, the operation of trains and the influence of the surrounding soil. This results in temperature patterns which vary throughout the period of a day due to the operation of trains, and throughout the year due to the influence of seasonal changes in ambient temperatures. In particular the influence of heat dissipated from train brakes, particularly in stations and in the tunnels immediately adjacent, dominates heat load in underground railways. This feature raises the station temperatures relative to the tunnels. In a contemporary underground railway braking heat is extracted from the underground environment at source, while in older systems this is not the case, resulting is significant heat loads in stations. London Underground is a singular example of this, with significant heat dissipation, in deep, small stations and tunnels, leading to a high heat density and high temperatures.

In contrast with older underground railways, a contemporary system will be designed with consideration for ventilation and cooling. In temperate climates the provision of ventilation shafts and well designed station areas will often maintain temperatures to acceptable levels, such as with the Jubilee Line Extension in London. A considerable body of research exists which considers the effectiveness of air shafts and the effect of the location, length and cross-sectional area. Previous studies have considered the effect on air velocities in stations, air exchange with the outside environment and station temperatures. In particular, the influence of train induced air flows upon ventilation and thermal conditions has been considered, as well as mechanical ventilation, and the interaction between the two. In many scenarios the train induced air flows are found to improve air exchange and thermal conditions, and are sufficient to maintain acceptable conditions in many cases.

While the train induced air flows are found to contribute to maintaining acceptable thermal conditions, it is also clear that the effectiveness is often far from optimal. Uneven patterns of air quality and temperatures in stations are attributed to the influence of train induced air flows, resulting in hot regions or pockets of poor air quality. Temperatures through the tunnels are often higher just leading into a station and cooler at the opposite end, and temperatures rise in the direction of train travel. The effect on temperatures of increasing train traffic has been found to be mitigated by the simultaneous increase in ventilation from train induced air flows. It has been found that mechanical ventilation systems and train induced air flows may conflict, thus reducing effectiveness. Additionally, there is a growing realisation that ventilation, both train induced and mechanically provided, may work against underlying air currents in an underground railway.

The piston effect mechanism which generates train induced air flows has been studied for many years. Particular concern has been given to the generation of high pressures and pressure transients which may cause discomfort, disturbance and infrastructure damage, and the effect of drag on train performance. The effect of train length, nose shape, train and tunnel cross-sectional areas and tunnel entrance shape have been investigated as to the effects.

In the context of underground railways, there has been significant interest in recent year of reducing the substantial energy demand from traction and non-traction requirements. Regenerative braking has been adopted to reduce energy demand and heat load. Improved control systems which monitor various parameters within a system have been adopted and resulted in significant reductions in energy demand. This has included taking account of train induced air flows in the operation of mechanical ventilation systems. In places new cooling methods, such as groundwater cooling, have been adopted.

Many older underground railways suffer from poor thermal conditions due to poor ventilation and high traffic loads. A particular example of this is London Underground, where conditions are expected to worsen due to increasing traffic and from the effects of climate change. Additionally, in newer systems, energy demand from ventilation and cooling can be high. The aim of this study was to study the train induced ventilation of underground stations. As the stations and immediately adjacent tunnels are where much of the heat in an underground railway is dissipated, it is in these areas where ventilation should be improved. Even though train induced air flows are known to improve underground railway thermal conditions and maintain air exchange with the ambient environment, the direct effect on the heat dissipated in stations is not known. Moreover, a detailed understanding of the air flows and train drag generated by the transit of a train in through a tunnel is not available. The increase or better utilisation of such air flows in stations may provide a low energy means of improving thermal conditions.

2.10 Summary

The study of ventilation and cooling of underground railways, the piston effect and improving the energy efficiency of underground railways is well developed. It is well understood that large amounts of heat are dissipated in stations and the adjacent tunnels and that train induced air flows provide an efficient means of underground railway ventilation. However, the literature review highlighted that the behaviour of train induced air flows and the capability of train induced air flows in directly removing heat from stations, and how this may be improved, is less well understood.

3

Numerical modelling

3.1 INTRODUCTION

Numerical modelling involves solving equations that describe some physical phenomenon. In this case that involves solving the partial differential equations which describe the behaviour of fluid flow. Analytical solutions of the continuous equations only exist for a small number of fluid flow problems. Therefore, in order to find solutions the fluid equations are solved using a domain of discrete points, constrained by boundary conditions. This is the essence of numerical modelling.

The general equations of fluid flow are the Navier-Stokes equations which describe the transport of momentum; the continuity equation which describes the conservation of mass; and the energy equation which describes the transport of heat. These continuous equations are discretised over a set of discrete points to form a system of algebraic equations, which are then solved subject to boundary conditions. As the fluid equations as non-linear, in order to find a numerical solution the system of equations is solved iteratively, to find a solution close to the exact solution. The difference in the numerical solution between iterations, known as the residual, is used to test whether the numerical solution is within a specified tolerance. Once the residual is within such a tolerance it is considered to be converged, i.e. a numerically acceptable solution has been found.

Even once a converged solution has been found, this may not actually represent physical reality. Therefore, a process of verification and validation of the solution must be carried out. Verification examines the modelling error, the difference between the numerical solution and observed conditions, and validation considers the numerical error, introduced during the numerical modelling process.

The implementation of the numerical methods used in this study is achieved using Ansys Fluent, a general purpose computational fluid dynamics code [10].

3.2 Governing equations

In this section the governing equations for fluid flow are outlined. The fluid flow is represented by the Navier-Stokes and continuity equations and heat transfer by the energy equation.

The derivation of the fluid governing equations considers the flow to be a continuum. A control volume is defined within the flow field and the mass conservation principle, the force-momentum principle and the first law of thermodynamics are applied to the control volume, the volume of which is then considered in the limit tending to an infinitesimally small size [138].

The force-momentum principle within a control volume states that the accumulation of momentum within a control volume is equal to the sum of the rate of momentum flow into and out of the control volume, the forces acting on the control volume faces and the body force within the control volume. Expressed mathematically [7], the unsteady, three-dimensional Navier-Stokes equations for a compressible viscous fluid subject to body forces, are given in conservative form as

$$\rho \frac{\partial U_i}{\partial t} + \rho U_j \frac{\partial U_i}{\partial x_j} = -\frac{\partial p}{\partial x_i} + \frac{\partial \tau_{ij}}{\partial x_j} + \rho F_i, \tag{3.1}$$

where $U = (u, v, w)$ is the fluid velocity field, ρ the fluid density, p the fluid pressure, F the body forces acting upon the fluid field, which are not considered in this study but included for completeness, and τ the viscous stresses given as

$$\tau_{ij} = \mu \left(\frac{\partial U_i}{\partial x_j} + \frac{\partial U_j}{\partial x_i} - \frac{2}{3}\delta_{ij}\frac{\partial U_k}{\partial x_k} \right), \tag{3.2}$$

where

$$\delta_{ij} = \begin{cases} 0, & \text{if } i \neq j \\ 1, & \text{if } i = j. \end{cases} \tag{3.3}$$

The continuity equation is derived by considering the conservation of mass within a control volume. This is stated as the rate of accumulation of mass within a control volume is equal to the sum of the rate of mass flow into and out of the control volume. Expressed mathematically, the continuity equation in conservative form is given as

$$\frac{\partial \rho}{\partial t} + \frac{\partial}{\partial x_i}\left(\rho U_i\right) = 0. \tag{3.4}$$

The first law of thermodynamics states that energy is conserved. When applied to a control volume, the conservation of energy is stated as the rate of change of energy within a control volume being equal to the sum of the net flux of heat into the control volume and the rate of work done on the fluid element by body and surface forces. Expressed mathematically, the energy equation in conservative form is given as

$$\frac{\partial E_i}{\partial t} + \frac{\partial}{\partial x_j}\left(\rho U_j E_i\right) = -\frac{\partial}{\partial x_i}\left(p U_i\right) + \frac{\partial}{\partial x_i}\left(\tau_{ij} U_j\right) + \frac{\partial}{\partial x_i}\left(\lambda \frac{\partial T}{\partial x_i}\right) + \rho F_i U_i \tag{3.5}$$

where

$$E_i = e + \frac{1}{2}U_i U_i \tag{3.6}$$

is the total enthalpy, e is the specific enthalpy, T is the temperature and λ is the coefficient of thermal conductivity.

All fluids are compressible, but under certain conditions the extent to which they can be compressed is small, so it may be assumed that the fluid is incompressible. The speed of trains in underground railways is generally low, relative to the speed of high speed trains. On London Underground the average train velocity is around

$10\,\mathrm{ms}^{-1}$ [129] with speeds on the Victoria Line reaching at least $22\,\mathrm{ms}^{-1}$. The incompressibility assumption is generally taken to be true for flows where the Mach number, $M = u/a$ where u is the air speed and a is the speed of sound in air, satisfies the condition $M < 0.3$ [138]. Therefore, to reach the limit of incompressibility, the air around the train would need to be travelling at $103\,\mathrm{ms}^{-1}$, significantly higher than that of underground trains. In this study the incompressible assumption is made throughout.

Stated mathematically, the incompressible condition is that the divergence of the flow velocity is zero, and the continuity equation reduces to

$$\frac{\partial U_i}{\partial x_i} = 0. \tag{3.7}$$

In conditions of incompressibility the momentum conservation equation becomes

$$\rho\frac{\partial U_i}{\partial t} + \rho U_j\frac{\partial U_i}{\partial x_j} = -\frac{\partial p}{\partial x_i} + \mu\left(\frac{\partial^2 U_i}{\partial x_j \partial x_j}\right) + \rho F_i. \tag{3.8}$$

3.3 Turbulence modelling

The equations describing an incompressible fluid, equations (3.7) and (3.8), can be applied to many classes of fluid flows. Many fluid flow problems are turbulent, meaning that they exhibit fluctuations over a variety of length and time scales. In order to capture such behaviour, the fluid equations would need to be solved using small length and time scales. Outside of a small number of esoteric examples, it is not practical to solve the fluid equations so that all length and time scales are captured, instead a modelling approach is used. Turbulence modelling typically models some proportion of the smallest scales within a fluid flow. In this thesis two modelling methods are used—the Reynolds-averaged approach and the Reynolds stress transport approach.

3.3.1 Reynolds-averaged Navier-Stokes equations

A common approach to turbulence modelling uses the Reynolds-averaged Navier-Stokes (RANS) equations. The RANS equations considers the fluid variables to consist of a mean and a fluctuating part, which is the case of the velocity is given as

$$U_i = \bar{U}_i + U_i' \tag{3.9}$$

where $\bar{U}_i$ is the mean part and U_i' is the fluctuating part. This approach, along with the assumption that $\rho = \overline{\rho}$ and $\mu = \overline{\mu}$ due to the incompressibility condition, and the ensemble-averaging of the continuity and Navier-Stokes equations gives the Reynolds-averaged form of the governing equations as

$$\frac{\partial}{\partial x_i}\left(\rho\overline{U_i}\right) = 0, \tag{3.10}$$

$$\rho\frac{\partial\overline{U_i}}{\partial t} + \rho\frac{\partial\overline{U_i U_j}}{\partial x_j} = -\frac{\partial\overline{p}}{\partial x_i} + \mu\left(\frac{\partial^2\overline{U_i}}{\partial x_j\partial w_j}\right) - \rho\frac{\partial\overline{U_i'U_j'}}{\partial x_j} + \overline{F_i}. \tag{3.11}$$

The derivation of the RANS equations has given rise to terms of the form $\rho\overline{U_i'U_j'}$, which are known as the Reynolds stresses. The Reynolds stresses result in a problem with 10 degrees of freedom in a system of four equations, therefore the system is not closed. To ensure closure, turbulence models are used to reduce the number of degrees of freedom. In this study the k-ϵ RNG turbulence model, derived from the Boussinesq approximation, and the Reynolds stress model, are used to close the system of equations.

3.3.2 Boussinesq approximation

It is assumed that the Reynolds stresses can be calculated from velocity gradients and the eddy viscosity, theorised by Boussinesq [24] as

$$-\rho\overline{U_i'U_j'} = 2\mu_t S_{ij} - \frac{2}{3}k\delta_{ij} \tag{3.12}$$

where

$$S_{ij} = \frac{1}{2}\left(\frac{\partial \overline{U_i}}{\partial x_j} + \frac{\partial \overline{U_j}}{\partial x_i}\right) \tag{3.13}$$

is the the mean rate of strain tensor and

$$k = \frac{1}{2}\left(\overline{U_i' U_i'}\right) \tag{3.14}$$

is the turbulent kinetic energy. This replaces the expressions for the Reynolds stresses and introduces two unknowns, k and μ_t. The k-ϵ RNG turbulence model represents the eddy viscosity using

$$\mu_t = \rho C_\mu \frac{k^2}{\epsilon}. \tag{3.15}$$

Therefore the Reynolds stresses Reynolds-averaged Navier-Stokes equations can be expressed in terms of U, p, k and ϵ. The k term represents the turbulent kinetic energy, a measure of the energy of the turbulence, and ϵ represents the turbulent dissipation, a measure of the dissipation of turbulent energy. Two further transport equations are solved to determine k and ϵ, given as [136]

$$\rho\frac{\partial k}{\partial t} + \rho\frac{\partial \overline{U_i} k}{\partial x_i} = \frac{\partial}{\partial x_j}\left(\mu_{\text{eff}}\alpha_k \frac{\partial k}{\partial x_j}\right) + 2\mu_t S_{ij} S_{ij} - \rho\epsilon \tag{3.16}$$

$$\rho\frac{\partial \epsilon}{\partial t} + \rho\frac{\partial \overline{U_i}\epsilon}{\partial x_i} = \frac{\partial}{\partial x_j}\left(\mu_{\text{eff}}\alpha_\epsilon \frac{\partial \epsilon}{\partial x_j}\right) + C_{1\epsilon}^{*}\frac{\epsilon}{k} 2\mu_t S_{ij} S_{ij} - C_{2\epsilon}\rho\frac{\epsilon^2}{k} \tag{3.17}$$

where

$$\mu_{\text{eff}} = \mu + \mu_t, \tag{3.18}$$

$$C_{1\epsilon}^{*} = C_{1\epsilon} - \frac{1 - \eta/\eta_0}{1 + \beta\eta^3}, \tag{3.19}$$

$$\eta = \left(2S_{ij}S_{ij}\right)^{1/2}\frac{k}{\epsilon}, \tag{3.20}$$

with $C_\mu = 0.0845$, $\alpha_k = \alpha_\epsilon = 1.39$, $C_{1\epsilon} = 1.42$, $C_{2\epsilon} = 1.68$, $\eta_0 = 4.377$ and $\beta = 0.012$.

3.3.3 Reynolds stress model

In place of assuming that the Reynolds stresses can be related to the velocity gradients and eddy viscosity, Reynolds stress models solve transport equations for the stresses. The transport equations take the form

$$\rho\frac{\partial\overline{U_i'U_j'}}{\partial t}+\frac{\partial\overline{U}_k\rho\overline{U_i'U_j'}}{\partial x_k}=-\rho\overline{U_i'U_k'}\frac{\partial\overline{U}_j}{\partial x_k}-\rho\overline{U_j'U_k'}\frac{\partial\overline{U}_i}{\partial x_k}+\frac{\partial}{\partial x_k}\left(\frac{\mu_t}{\sigma_k}\frac{\partial\overline{U_i'U_j'}}{\partial x_k}\right)-\frac{2\rho\epsilon\delta_{ij}}{3}+\phi_{ij} \tag{3.21}$$

where ϕ_{ij} is the linear pressure-strain correlation model [136] and $\sigma_k = 1.0$. The effect of bouyancy is not considered in this study and so has been neglected. An additional transport equation for the turbulent dissipation is also solved in the same manner as for the k-ϵ RNG model for closure.

3.4 Wall treatment

Turbulent flows are affected by the presence of walls, due to the no-slip condition for the velocity and changes to the turbulence. The layer of flow near the wall can be divided into three layers. In the closest layer to the wall, known as the laminar or viscous sublayer, the flow is almost laminar and momentum and heat transfer are dominated by molecular viscosity. In the outer layer, turbulence dominates the flow. Between the inner and outer layers an intermediate layer, the buffer layer, in which the effects of molecular viscosity and turbulence are of more equal importance. The k-ϵ RNG and Reynolds stress models are generally valid in the turbulent, high Reynolds number, regions of the flows and therefore wall boundary modifications are required to properly represent the physical behaviour.

In this study a wall function approach is used to model flow behaviour at wall boundaries. In this context, instead of resolving the flow close to a wall, formulae are used in the laminar sublayer and buffer layer. The wall function approach reduces the computational expense in the region of the flow which generates large gradients in the flow variables and is the main source of vorticity and turbulence.

The wall function formulation used is this thesis is that presented by Launder &

Spalding [90]. Within the buffer layer and outer layer the log law of the wall gives

$$U^* = \frac{C_\mu^{1/4} k^{1/2}}{\kappa} \ln E y^* \tag{3.22}$$

where U^* is a dimensionless velocity and

$$y^* = \frac{C_\mu^{1/2} k^{1/2} y \rho}{\mu}, \tag{3.23}$$

where y^* is a dimensionless wall distance, and $\kappa = 0.4187$ is the von Kármán constant, $C_\mu = 9.793$, y is the distance to the wall. The expression for the velocity given in equation (3.22) is considered to be valid for $30 < y^* < 300$, but in this study it is assumed to be valid for $11.225 < y^*$. For $y^* < 11.225$ the laminar stress-strain relationship is applied, which is expressed as

$$U^* = y^*. \tag{3.24}$$

A similar approach is taken for the temperature in the energy equation. For the turbulence, the k equation is solved for the whole domain and the wall conditions specified using

$$\frac{\partial k}{\partial n} = 0 \tag{3.25}$$

for the k-ϵ RNG model and in the Reynolds stress model the Reynolds stresses are specified using wall functions and at the wall by a series of expressions. In both models, ϵ is obtained using wall functions.

3.5 FINITE VOLUME METHOD

The governing equations are discretised using the finite volume method, a approach employed frequently in computational fluid dynamics due to the simplicity, robustness and efficiency of the method [136].

3.5.1 Discretisation

Discretisation of the governing equations will be shown for the case of the general transport equation of a scalar quantity ϕ. The principles shown here are directly applicable to the fluid governing equations. The general transport equation is given as

$$\rho\frac{\partial\phi}{\partial t}+\rho\frac{\partial U_i\phi}{\partial x_i}=\frac{\partial}{\partial x_j}\left(\Gamma\frac{\partial\phi}{\partial x_j}\right) \tag{3.26}$$

where Γ is a scalar diffusion coefficient. In the finite volume method, the equation under consideration is integrated over a control volume, which expresses the conservation laws at each control volume. The general transport equation written in integral form for a control volume V is given as

$$\frac{\partial}{\partial t}\int_V \rho\phi\, dV+\int_S \rho U_i\phi\, dn_i=\int_S \Gamma\frac{\partial\phi}{\partial x_j}\, dn_j \tag{3.27}$$

where S is the surface area of the control volume and n_i is the outward vector from the control volume surface. In this form the equation is still in exact form. In order to be solved numerically, approximations are made using various discretisation schemes. In discretised form the general transport equation becomes

$$\rho V\frac{\partial\phi}{\partial t}+\sum_f^{N_{\text{faces}}}\rho_f\left(U_i\right)_f\phi_f\cdot S_f=\sum_f^{N_{\text{faces}}}\Gamma\left(\frac{\partial\phi}{\partial x_j}\right)_f\cdot S_f \tag{3.28}$$

where N_{face} is the number of cell faces, S_f is the surface area of a cell face, ϕ_f and ρ_f are the values of ϕ and ρ at a cell face and $\left(U_i\right)_f$ is the value of U_i at a cell face. The transient term is discretised using first-order backward differences given as

$$\frac{\partial\phi}{\partial t}=\frac{\phi^{n+1}-\phi^{n}}{\Delta t} \tag{3.29}$$

where $n+1$ and n are the values at the next and current time steps, $\Delta t+1$ and Δt.

The values of ϕ on the cell faces must be interpolated from the cell centre where the values are stored. In this study the QUICK scheme is used for this purpose. Additionally, for the momentum equation a pressure interpolation scheme is required to find the pressure at the cell faces, for which the PRESTO! scheme is used.

3.5.2 Moving mesh

Moving meshes, along with re-meshing, allow for the manipulation of the mesh during transient simulations for the modelling of the domains in which the shape of the boundaries change with time. In this study moving meshes are utilised for all the simulations of moving trains.

3.5.2.1 Discretisation

To account for the movement of the mesh boundary, the general scalar transport equation takes a modified form expressed as

$$\frac{d}{dt}\int_V \rho\phi\, dV + \int_S \rho\left(U_i - Z_i\right)\phi\, dn_i = \int_S \Gamma\frac{\partial\phi}{\partial x_j}\, dn_j \tag{3.30}$$

where Z_i is the velocity of the moving mesh. As the volume of the cell volumes is now dependent on time, the discretisation of the transient term takes the form

$$\frac{d}{dt}\left(\rho\phi V\right) = \frac{\left(\rho\phi V\right)^{n+1} - \left(\rho\phi V\right)^{n}}{\Delta t} \tag{3.31}$$

where the cell volume is calculated using

$$V^{n+1} = V^n + \frac{dV}{dt}\Delta t \tag{3.32}$$

where the volume time derivative is

$$\frac{dV}{dt} = \sum_{f}^{N_{\text{faces}}} \left(Z_j\right)_f \cdot S_f \tag{3.33}$$

where

$$\left(Z_j\right)_f \cdot S_f = \frac{\delta V}{\delta t}. \tag{3.34}$$

Where a mesh moves relative to a stationary reference frame the control volume remains constant and therefore $dV/dt = 0$ and $V^{n+1} = V^n$.

3.5.2.2 Mesh layering

In this study mesh manipulation is carried out through a process of adding and removing layers of cells from mesh zones adjacent to moving boundaries. The layering method can be used with quad or hexahedral cell meshes. A target cell height is specified on the moving boundaries, and the cells adjacent to the boundaries are either collapsed or split depending on the direction of movement. The point at which the cells are collapsed or split depends on the hight of the cells adjacent to the moving boundary and one of two defined factors; either a layer collapse or a layer split factor. Figure 3.1 illustrates the components of mesh layering.

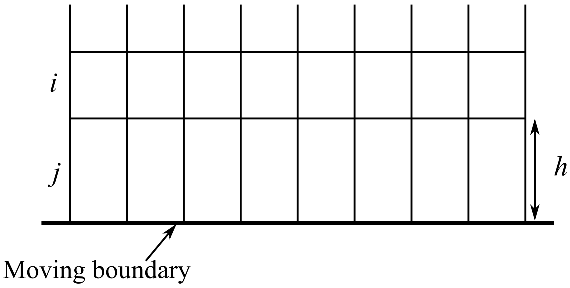

Figure 3.1: Mesh layering.

If the cells in layer j are expanding, the cell heights grow until the condition

$$h_j > (1 + \alpha_s)h_{\text{new}} \tag{3.35}$$

is met, where α_s is the layer split factor, h_j is the minimum height of cells in layer j and h_{new} is the specified height of cells on the moving boundary. Once the split condition is met, the cells in layer j are split so that the ratio of the new cells is α_s everywhere on the moving boundary.

During compression, cells in layer j are compressed until the condition

$$h_j < \alpha_c h_{\text{new}} \tag{3.36}$$

is met, where α_c is the layer collapse factor. Once the compression condition is met, the cells in layer j are collapsed and merged with those in layer i. In this study the split factor is given as $\alpha_s = 0.4$ and the collapse factor is $\alpha_c = 0.2$.

3.6 Mesh generation

In order to utilise moving meshes and mesh layering to simulate the movement of trains, the computational meshes must be generated in a specific manner. To simulate the train movement, meshes are formed in at least three discrete regions—a fixed region around the train which moves with the prescribed train speed and regions ahead of and behind the moving region. In the regions behind the moving region, mesh layering is used to add cell layers to the mesh region, while cell layers are removed from the region in front of the moving region. The mesh regions behind and in front of the moving region are made up of a quad or hexahedral cell mesh, depending whether the model is in 2- or 3-dimensions, in order to allow the use of mesh layering.

The computational meshes used to represent stations were formed of 3-dimensional hexahedral meshes.

3.7 Solution methods

The discretised systems of equations are solved literately. In this study the SIMPLE and PISO algorithms and a coupled scheme are used.

The PISO algorithm is an extension of the extensively used SIMPLE algorithm. The SIMPLE algorithm does not fully resolve the pressure-velocity coupling, instead approximations are made to the pressure gradients from the initial conditions or previous iteration. The first step in the algorithm calculates a velocity field from the estimated pressure gradients, next a pressure correction equation is solved and used to correct the pressure field and finally a new velocity field is calculated by correcting the values using the pressure correction. In the PISO algorithm, a secondary correction step is carried out. In contrast, the coupled scheme solves the system of equations simultaneously in one step.

3.8 Sources of error

Sources of error are an inevitable consequence of using a model to represent a real fluid flow. Considering the possible errors allows the models to be refined in these regions.

3.8.1 Modelling error

Modelling error arises due to differences between the actual flow and that represented by the model. In order to represent a real flow as a model assumptions are made as part of the modelling process. In order to justify the assumptions and to verify that the model represents the actual flow, computational fluid dynamics models are verified by comparing model results with experimental data.

3.8.2 Numerical error

The Navier-Stokes equations are known to represent many fluid flows. As part of the numerical modelling, the exact equations are approximated over a set of discrete points in space, e.g. Δx, and time, Δt. Therefore, there exists a difference between the exact and the numerical solutions. This is known as the discretisation error. The discretisation error is influenced by the choice of discretisation scheme, the size of the mesh and the size of the time step. In order to reduce numerical error the size of the mesh and time step can be studied to investigate the influence on flow properties. Specific mesh and time step sizes are discussed throughout the thesis.

The calculation of the numerical solution proceeds iteratively. At each iteration the difference between the numerical solution at that time step and that at the previous step, known as the residual, is calculated. The convergence of the solution can be controlled by ensuring that the residual value is within a particular bound. Additionally, the values of solution quantities, often of particular interest, may also be monitored, to ensure that the solution has reached a converged solution. Specific details of the convergence criteria are given throughout the thesis.

3.9 IMPLEMENTATION

In this study the computational fluid dynamics software Ansys Fluent [10] has been used for the numerical modelling. Ansys Fluent is said to solve the Navier-Stokes equations on an unstructured mesh, using the finite volume scheme. Ansys ICEM was used for mesh generation [12]. Ansys Fluent allows for the use of mesh layering, and as the main topics of research in this study is the modelling of a moving train in a tunnel, Ansys Fluent was chosen for the numerical modelling.

3.10 SUMMARY

In this chapter the numerical methods used in this thesis have been introduced. The governing fluid equations have been presented along with the turbulence modelling approaches. The finite volume scheme was described along with the modified formulation used to model moving meshes. Numerical modelling introduces errors due to modelling and numerical approximations, which were discussed along with the means of accounting for and minimising such errors.

4

The effect of geometric and kinematic parameters upon underground railway aerodynamics

4.1 Introduction

The piston effect, generated by a train moving though a tunnel, induces significant air flows and pressure in tunnels and generates significant aerodynamic drag upon the train. The piston effect is influenced by the geometrical parameters of a particular train-tunnel configuration—in particular by the blockage ratio, train and tunnel lengths and the shape of the train nose. This chapter considers the geometric and kinematic parameters which influence the magnitude of train induced air flows and drag, and the transient behaviour.

First a scale model configuration of an underground railway is considered, which is modelled as a 3-d representation using computational fluid dynamics. The scale model configuration is verified using results from the literature and scaled geometrically to represent a full scale configuration, then scaled kinematically to consider the effect of train velocity. The influence of the train and tunnel length on the train induced air flows and train drag are presented. In order to represent the parameters of an existing underground railway operating at high blockage ratio, the model is altered to represent the Victoria Line, UK. This is carried out by altering the cross sectional areas of the train and tunnel, and of the rate of acceleration and deceleration of the train.

The blockage ratio of the Victoria Line model is varied and the effect at high blockage ratios is investigated. The impact on the air flow patterns around the train induced air flows and aerodynamic work are presented. The effect in different phases of the train motion are also considered.

The results obtained within this chapter were published, in part, in Cross et al. [34].

4.2 METHODOLOGY

A transient, three-dimensional computational fluid dynamics simulation was used to model the induced air flows and drag generated by train movement in a tunnel. The work in this chapter is formed of two parts; a verification of a CFD model of an underground railway and the examination of the effect of the train and tunnel length and high blockage ratio upon tunnel air flow and train drag.

An idealised scale model representation of an underground railway environment, selected from the literature, was employed in order to simplify the physical phenomena and modelling process and is modelled using CFD. Verification was carried out with available experimental results from the literature. This model was scaled geometrically to represent the full scale, the train velocity varied to examine the effects and the geometry altered to represent an existing underground railway operating at high blockage ratio (Victoria Line, London Underground, UK). This process is carried out to establish the impact of the blockage ratio and train and tunnel length in current underground railways operating at high blockage ratio. The blockage ratio and train and tunnel length are all varied independently and the impact upon tunnel air flows and train drag is presented.

4.3 Scale model configuration

4.3.1 Model domain

The scale model configuration used in this chapter is based upon the experimental set-up presented by Kim & Kim [85] and used subsequently by various authors [86, 69, 71]. The model is shown schematically in Figure 4.1, and describes a $^1/_{20}$ scale model of an underground railway.

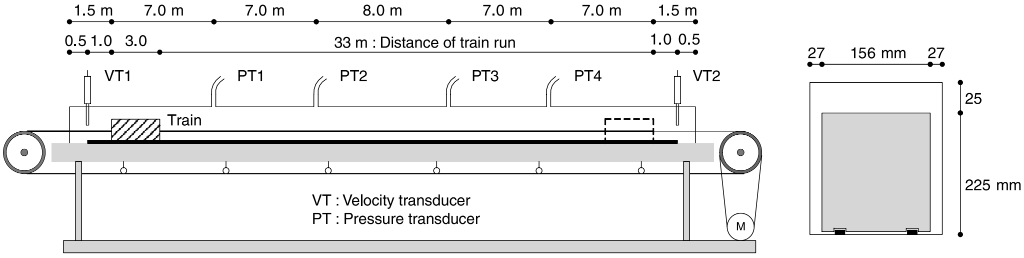

Figure 4.1: A schematic diagram of the Kim & Kim [85] train and tunnel scale model experimental set-up.

The tunnel does not include any features such as shafts or passages and the train no features or gaps between carriages, to allow the investigation of the train induced flows without interference from other factors. The set-up consisted of a tunnel, both ends open to the atmosphere, through which a model train was passed. The tunnel was 39 m long, 0.21 m wide and 0.25 m high, while the train was 3 m long, 0.156 m wide and 0.225 m high. The tunnel height is given as 0.25 m, the train height as 0.225 m and the vertical upper gap between the train and tunnel as 0.025 m, but the lower vertical gap between the train and tunnel is not stipulated. In this study a value of 0.003 m is used to represent a gap under the train without reducing the height of the train significantly, which was estimated from Figure 4.1.

The train starting position is with the back 1.5 m from the tunnel entrance portal, it was accelerated at 1 ms^{-2} for 3 s, ran at a constant cruising velocity of 3 ms^{-1} for 8 s and then decelerated at -1 ms^{-2} for 3 s, to an end position with the front 1.5 m from the tunnel exit portal. The train remained within the confines of the tunnel for the entire period of travel. Here we refer to the tunnel entrance as the portal which the train is travelling away from and the tunnel exit as the portal that the train is travelling towards. The three phases of motion—acceleration, cruising and deceleration—are referred to throughout this chapter.

Kim & Kim [85] used transducers to take pressure and velocity readings at four and two points, respectively, in the positions shown in Figure 4.1. The pressure readings were at the tunnel roof and the velocity readings were in the centre of the tunnel cross section. No details were given regarding the measurement equipment used nor of any uncertainties.

4.3.2 Computational mesh

The numerical domains investigated were produced in ICEM [12] using a hexahedral grid structure. The grid was formed so that smaller cells were concentrated around the front, back and sides of the train and the walls of the tunnel to provide sufficient resolution in these regions and larger cells far from the train in order to improve computational efficiency. The final grid structure around the train front is shown in Figure 4.2. A grid convergence test was carried out and a grid with sufficient accuracy was found that contains 1388838 cells. A time step size convergence study was also conducted giving a time step size of 0.01 s as being acceptable.

The numerical modelling was performed using the Ansys Fluent [11] commercial CFD software package. In order to simulate the train movement, the dynamic meshing option in Ansys Fluent, specifically the dynamic layering method, was utilised as outlined by Huang et al. [69]. This was applied by first dividing the computational domain into three fluid zones; a near field around the train and two far fields ahead of and behind this zone. The near field zone is moved forward at the specified train velocity and layers of cells added to the zone behind and removed from the zone ahead of the train. In this way the dynamic meshing process is simplified and the fluid zone around the train can remain unaltered. The use of a hexahedral grid, shown in Figure 4.2, allowed the use of dynamic layering.

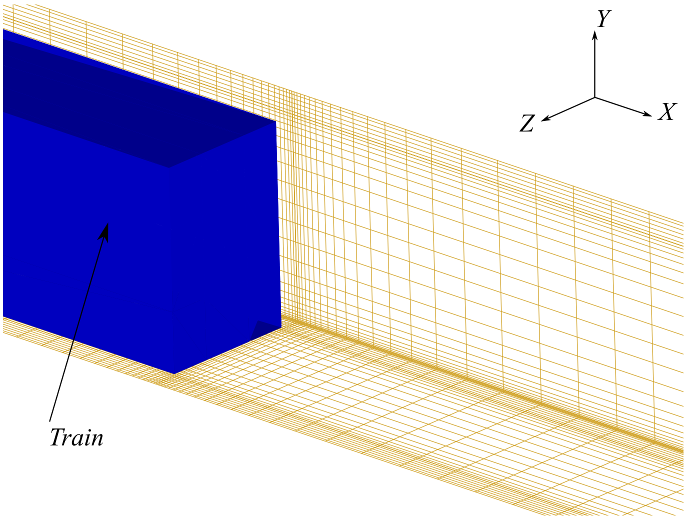

Figure 4.2: Hexahedral grid around the train front.

4.3.3 Modelling conditions

In this study, the unsteady air flows are treated as an incompressible fluid [127]. This is justified as velocities of trains in an underground railway are relatively low (average of $9\,\mathrm{ms}^{-1}$ and maximum of $27\,\mathrm{ms}^{-1}$ in London Underground for example) and thus compressible effects are moderate, given that the flow Mach number is small and that there is an absence of tunnel features which may create compressible effects. For the unsteady, incompressible fluid flow in an underground railway, the Reynolds-averaged Navier Stokes equations are solved using Fluent.

The k-ϵ RNG model is utilised in this chapter due to it's suitability on the investigation of train induced air flows, in which it was found to perform well [143, 70]. Near wall flows were modelled using the standard wall function approach. This was to reduce the computational time of the transient calculations in comparison with a near wall modelling approach. The first cell heights on the walls of the model are chosen so that the non-dimensional y^* value is maintained in the recommended range of $30 < y^* < 300$, where y^*, u_τ, y, ρ and μ are the dimensionless wall distance, friction velocity, distance from the wall, fluid density and, dynamic viscosity respectively [11].

The governing equations are solved by use of the finite volume method on an unstructured grid. In this study, the PISO pressure-velocity coupling method is adopted to solve the governing equations. The QUICK interpolation scheme is used for the discretisation of the convection terms and the PRESTO scheme to treat the pressure interpolation, for improved performance in conditions with adverse pressure gradients. Convergence criteria for the continuity, momentum, k and ϵ residual equations were set as 1×10^{-5} and additionally the pressure and velocity were monitored at various points within the domain. It was found that using a convergence criteria of 1×10^{-5} ensured that the changes in monitored flow quantities between iterations exhibited only small changes, while maintaining computational efficiency. A smaller convergence criteria showed minimal changes in flow quantities. Mass conservation within the computational domain was also monitored to ensure conservation at every time step.

4.3.4 Boundary and initial conditions

At the tunnel inlet and outlet, an outlet boundary condition with a static pressure of 0 Pa was applied. This value is given relative to an operating pressure, set at atmospheric pressure. The boundary conditions allow for the dynamic pressure (sometimes called the velocity pressure) to vary while the static pressure is fixed. This allows pressure changes at the boundaries, such as when the train approaches the outlet. An investigation was undertaken of different boundary condition combinations, including pressure inlet and outlet and periodic conditions, however this combination was found to provide good accuracy when compared to results obtained by Kim & Kim [85] and the approach is in agreement with that of Khayrullina et al. [84].

4.4 Scale model verification

This section presents the numerical results from the scale model configuration. Experimental data from Kim & Kim [85] are used to verify the numerical results and the error evaluated between the two techniques. The results presented in this section are given partly in transient form and the behaviour of the flow characteristics is explained in terms of the train position and the phase of train movement.

4.4.1 Pressure coefficient

Kim & Kim [85] measured the pressure at four points within the tunnel during the motion of the train and presented the results in terms of a pressure coefficient. The pressure measurement points, PT1-PT4, are indicated in Figure 4.1, and are located within the cruising phase of the train. The pressure coefficient used in this chapter is given as

$$C_p = \frac{p}{\frac{1}{2}\rho u_*^2} \tag{4.1}$$

where u_* is a reference velocity, taken to be the maximum velocity of the train, u_{tr}^{max}. The pressure coefficient is an expression of the pressure normalised by the dynamic pressure calculated using the reference velocity. The reference velocity is fixed as the maximum velocity of the train to ensure that it is only the pressure term within the pressure coefficient that changes with time, otherwise interpretation would be complicated if the coefficient was dependent on more than one variable. The transient pressure coefficient at points PT1-PT4 are shown in Figures 4.3 and 4.4. The vertical lines at 3 s, 11 s and 14 s indicate the end of the acceleration phase, the end of the cruising phase and the end of the deceleration phase, respectively. The shaded areas indicate the period during which the train is passing the respective measurement point.

As the train accelerates, the pressure coefficient increases at all measurement points. The pressure coefficient at measurement points closer to the accelerating train increase to a lower maximum the further from the train that the point is located, due to the build up in pressure at the front of the train. Once the train stops accelerating and enters the cruising phase, the pressure coefficient immediately begins to decrease, as the inertia of the air has been overcome and is no longer being accelerated. The decrease in the pressure coefficient during the cruising phase occurs rapidly, and then appears to asymptote towards a constant value. The trend of the pressure coefficient is interrupted by the passing of the train, which causes a sudden drop due to the pressure gradient between the front and back of the train. Once the train has passed the pressure coefficient rises again, but now has a negative value.

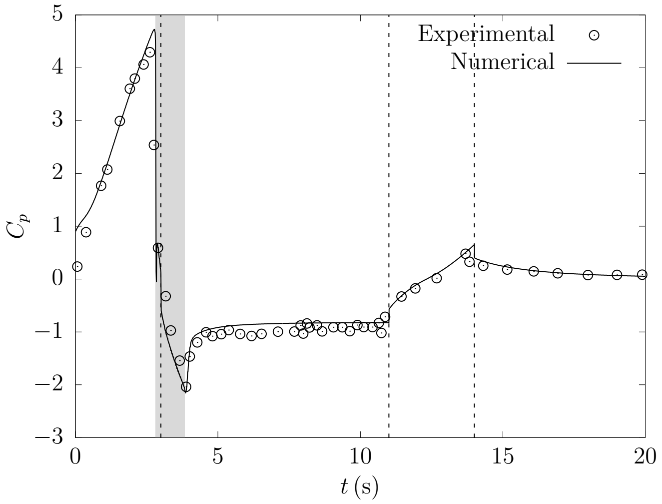

(a) PT1

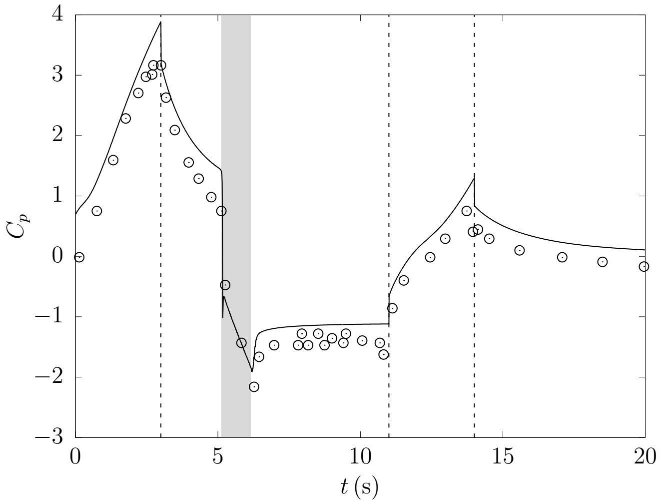

(b) PT2

Figure 4.3: The transient pressure coefficient (C_p) at points shown in Figure 4.1 (Experimental result ∘, Numerical result —).

Once the train begins to decelerate the pressure coefficient increases, with a higher maximum observed closer to the train. The increase is caused by the body of air behind the train moving faster than the train, as it still has momentum generated by the cruising train, and thus generates pressure on the back of the train as the train decelerates, to a velocity slower than the air. Once the train has stopped, the pressure coefficient drops rapidly then slowly decays, as the air velocity in the tunnel drops.

Generally, the agreement between the experimental data from Kim & Kim [85]

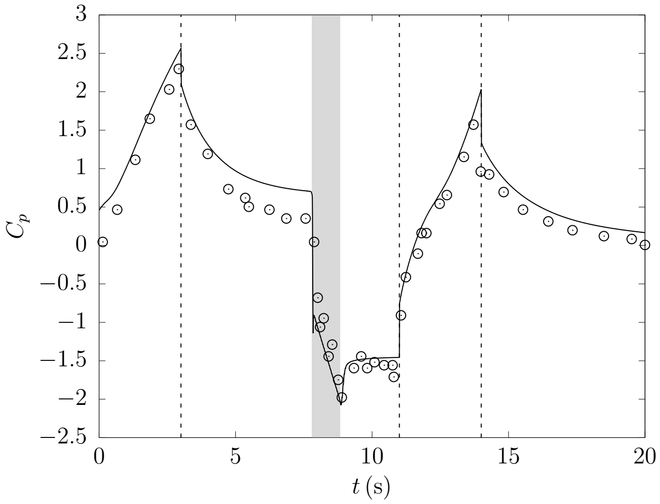

(a) PT3

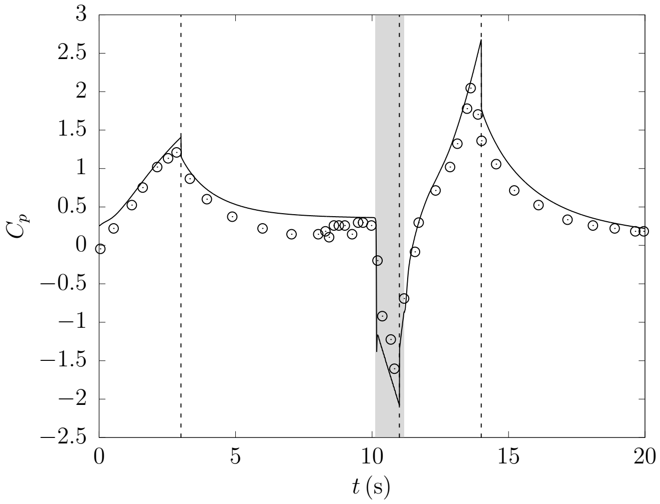

(b) PT4

Figure 4.4: The transient pressure coefficient (C_p) at points shown in Figure 4.1 (Experimental result ○, Numerical result —).

and the numerical results is good. In particular, the trend at all the measurement points is reproduced well. The largest deviations are found at the pressure peaks, such as at the end of the acceleration and deceleration phases and at the point where the train front and back passes a particular measurement point.

4.4.2 Velocity coefficient

Kim & Kim [85] also measured the velocity at two points within the tunnel during the motion of the train and presented the results in terms of a normalised velocity coefficient. The velocity measurement points, VT1 and VT2, are indicated in Figure 4.1, and are located close to the entrance and exit of the tunnel. The normalised velocity coefficient used in this chapter is given as

$$U^+ = \frac{u}{u_*} \tag{4.2}$$

where u_* is a reference velocity, taken to be the maximum velocity of the train, u_{tr}^{max}. The transient velocity coefficient is presented in Figure 4.5, the vertical lines again denote the end of the acceleration, cruising and deceleration phases.

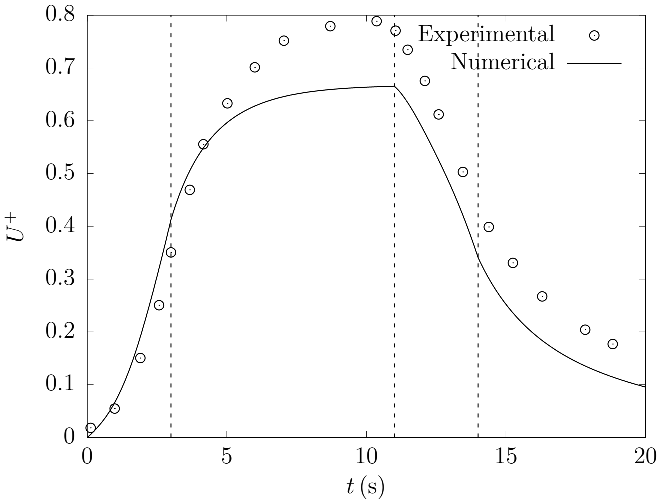

(a) VT1

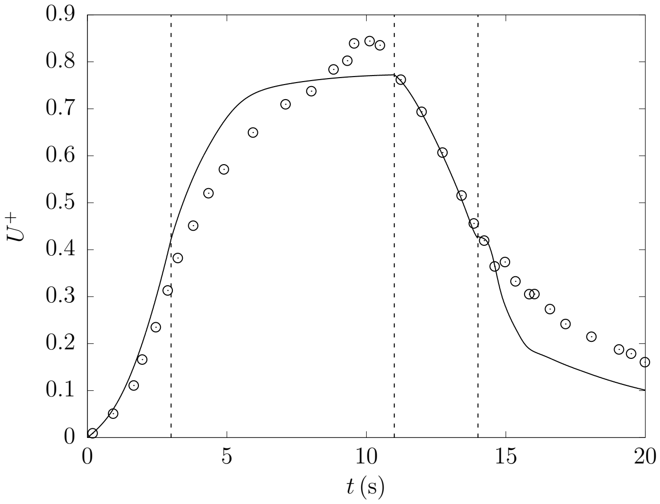

(b) VT2

Figure 4.5: The transient velocity coefficient (U^+) at points shown in Figure 4.1 (Experimental result ∘, Numerical result —).

As the train accelerates, the velocity coefficient increases rapidly at both measurement points. During the cruising phase, the velocity continues to increase, at a slower rate, and asymptotes towards a constant value. During deceleration, the velocity decreases rapidly as the slowing train acts upon the air in the tunnel. In the acceleration and deceleration phases, where inertial forces dominate, the agreement between the experimental data and numerical results is generally good, while during the cruising phase, where viscous forces dominate, the agreement is less good. The trend shown by the numerical results illustrate good agreement with the experimental data, but the maximum velocity at both points is lower. In particular, the lower velocity at the tunnel entrance and higher velocity at the tunnel exit in the initial stages of the cruising phase, compared to the experimental data, suggests that the model is over predicting the air being pushed ahead of the train, and under predicting the air being sucked from behind. However, the relative magnitude of the velocity at the entrance and exit of the tunnel preserves the behaviour observed in the experimental data. The total displaced air is presented in this study is used to illustrate the ventilating effects of the train movement. This is validated by comparing the time integrals of the measured and numerical velocity curves at the tunnel entrance and exit, which gives differences of 10.0% and 4.7%, respectively. These are within acceptable bounds.

Although there are disparities between the measured and numerical values at the velocity measurement points, the acceptable agreement over the time integrals, and for the purposes of the relative comparison of drag in the parametric study shown within this chapter the verification is considered sufficient.

4.5 MODEL SCALING

The model outlined, modelled and validated in Section 4.3 represents, according to Kim & Kim [85], a $^1/_{20}$ scale model of an underground railway. Kim & Kim [85] make no reference to the full scale underground railway on which the scale model is based, and do not consider what the scale model represents at full scale. While scale models can be used to investigate full scale phenomenon in a laboratory in an efficient and controlled manner, it is essential that the model represents realistic conditions at full scale. To ensure that the model is representing the full scale, the scale model is first scaled, both geometrically and kinematically, to represent the full scale, following the rules of similarity. Secondly, the velocity of the train in the full scale model is varied to investigate the changes in the air flows and aerodynamic parameters at a more realistic train velocity.

4.5.1 SIMILARITY

Similarity is ensured through the observation of three criteria: geometric, kinematic and dynamic similarity. Geometric similarity is maintained through the scaling of the dimensions of the scaled model by a factor of 20, so that the proportions of all the dimensions are maintained. Table 4.1 gives the characteristic dimensions of the scale and full scale models, denoted as M_1 and M_2. The dimensions x, y and z denote the length, height and width of the train (tr) and tunnel (t), respectively.

Table 4.1: Characteristic dimensions.

	M_1	M_2
x_{tr}	3.000	60.000
x_t	39.000	780.000
y_{tr}	0.225	4.500
y_t	0.250	5.000
z_{tr}	0.156	3.120
z_t	0.210	4.200

Kinematic similarity requires that the length and time scales in the scale and full scale models are similar, and dynamic similarity requires that the forces at corresponding points are similar. Given that the scale and full scale models are geometrically similar, kinematic and dynamic similarity are ensured by maintaining the instantaneous Reynolds number, Re, and train drag coefficient, C_D, between the two models. The Reynolds number is given as

$$Re = \frac{\rho u y_t}{\mu} \tag{4.3}$$

where u is the air velocity, y_t is the tunnel height, the density $\rho = 1.225\,\mathrm{kgm^{-3}}$ and dynamic viscosity $\mu = 1.7894 \times 10^{-5}\,\mathrm{kgs^{-1}m^{-1}}$ (at 288.15 K air temperature). The drag coefficient is given as

$$C_D = \frac{F_x}{\frac{1}{2}\rho A u_*^2}. \tag{4.4}$$

where F_x is the force acting upon the train along the axis of motion, A_{tr} is the frontal area of the train and u_* is a reference velocity, taken to be the maximum velocity of the train, u_{tr}^{max}. As the train is the only influence on the movement of air, the velocity of the train must be scaled accordingly to maintain similarity. The train movement is transient, therefore the kinematic parameters, the maximum velocity, acceleration and deceleration rates (${}^{du_{tr}}\!/_{dt}$) and total travel time of the train (t_T) were scaled. The kinematic properties of the scale and full scale models are shown in Table 4.2.

Table 4.2: Kinematic parameters for models M_1 and M_2.

Model	u_{tr}^{max} (ms^{-1})	${}^{du_{tr}}\!/_{dt}$ (ms^{-2})	t_T (s)
M_1	3.00	± 1.00	14.0
M_2	0.15	$\pm 1.25 \times 10^{-4}$	5600.0

Figure 4.6 shows the train drag coefficient and velocity coefficient for the scale model M_1 and full scale model M_2. The velocity coefficient is calculated using the velocity measured at VT2 in Figure 4.1, referred to as the outlet velocity coefficient (U_o^+). The results are presented as a function of the normalised time $T^+ = {}^{t}\!/_{t_T}$, where t_T is the total time of train movement, to allow for direct comparison.

From Figure 4.6 it can be seen that U_o^+ for M_1 and M_2 are essentially identical, which implies that

$$u_{M_2} = \frac{u_{M_1}}{20} \tag{4.5}$$

where u_{M_1} and u_{M_2} are the outlet velocities in models M_1 and M_2. Therefore the Reynolds number, calculated using equation (4.3) is given as

$$Re_{M_1} = \frac{\rho}{\mu} u_{M_1} y_{t_{M_1}} \implies \frac{\rho}{\mu} 20 u_{M_2} \frac{y_{t_{M_2}}}{20} = Re_{M_2} \tag{4.6}$$

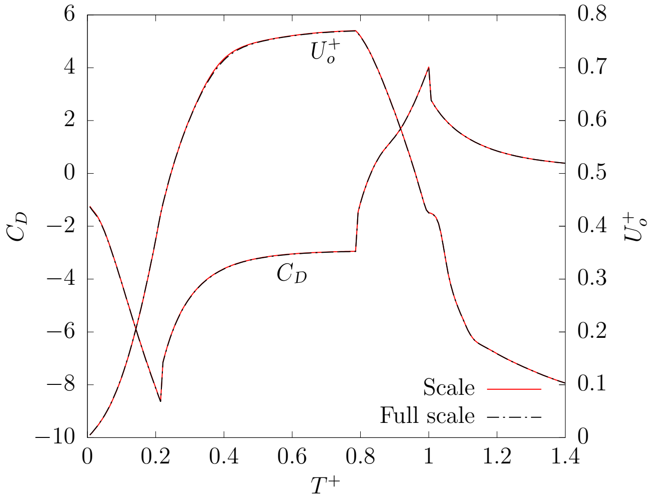

Figure 4.6: Train drag (C_D) and outlet velocity (U_o^+) coefficients for models M_1 and M_2.

where $y_{t_{M_1}} = y_{t_{M_2}}/20$, where $y_{t_{M_1}}$ and $y_{t_{M_2}}$ are the heights of the tunnel in models M_1 and M_2. This implies that the Reynolds numbers in models M_1 and M_2 are essentially identical.

Since the geometries are geometrically similar, and that the Reynolds number and train drag coefficient are consistent in both cases, kinematic and dynamic similarity has been ensured.

4.5.2 Re_{max} VARIATION

This section illustrates the effect of maximum train velocity on the air flows and train drag generated by the movement of the train within the tunnel. The velocity of the scaled model M_2 does not represent what would be considered a realistic velocity for an underground railway, therefore to undertake a meaningful analysis a more realistic velocity must be used. To assess the effect of an increased, and more realistic, train velocity the maximum velocity of the train in model M_2 is increased as shown in Table 4.3. The rate of acceleration and deceleration are also altered, so that the acceleration, cruising and deceleration phases of travel make up the same proportion of the total travel time in each case.

The cases are identified by the Reynolds number at maximum train velocity, Re_{max}, calculated using equation (4.3). This is used as a convenient description of

Table 4.3: Re_{max} scaling parameters for the model M_2.

Case (Re_{max})	u_{tr}^{max} (ms^{-1})	${}^{du_{tr}}/_{dt}$ (ms^{-2})	t_T (s)
5.134×10^4	0.15	$\pm 1.250 \times 10^{-4}$	5600.000
8.215×10^5	2.40	± 0.032	350.000
1.314×10^7	38.40	± 8.192	21.875

each case given in Table 4.3, while each case will have a different average and a constantly varying instantaneous value of Reynolds number. The effect of increasing the maximum train velocity is illustrated by showing the changes in flow patterns around the front of the train and the consequential effects on the train drag and tunnel outlet velocity. The behaviour of the pressure and viscous components of train drag are also discussed.

4.5.2.1 Flow patterns

The air flow around the front of the train, and in the train-tunnel gap between the train side and tunnel wall, are illustrated as velocity vectors in Figure 4.7.

The velocity vectors are drawn in the moving reference frame, i.e. relative to the train, in the x-y plane at $z = 0\,\mathrm{m}$ plane, at $T^+ = 0.5$. The vectors are coloured by normalised velocity magnitude relative to the train, normalised by the maximum velocity of the train, expressed as $\left(\sqrt{u_{rel}^2+v_{rel}^2}\right)/u_*$ where u_{rel} and v_{rel} are the velocity components relative to the train in the x and y dimensions. The plane is drawn in the upper region of the tunnel, extending from $x = 1.5\,\mathrm{m}$ to $x = -2\,\mathrm{m}$ where $x = 0\,\mathrm{m}$ is taken to be the position of the front of the train.

As the train moves through the tunnel, air is displaced and either moves ahead of or towards the back of the train through the train-tunnel gap. Figure 4.7(a) shows the flow patterns around the front of the train for the $Re_{max} = 5.134 \times 10^4$ case. Relative to the train, the air ahead of the train is moving at almost the same velocity as the train. The air flowing through the train-tunnel gap moves from the front to the back of the train at a maximum of about 1.6 times the velocity of the train. As the air flows around the blunt corner of the train a small recirculating region is observed. For the $Re_{max} = 1.314 \times 10^7$ case shown in Figure 4.7(b) a similar

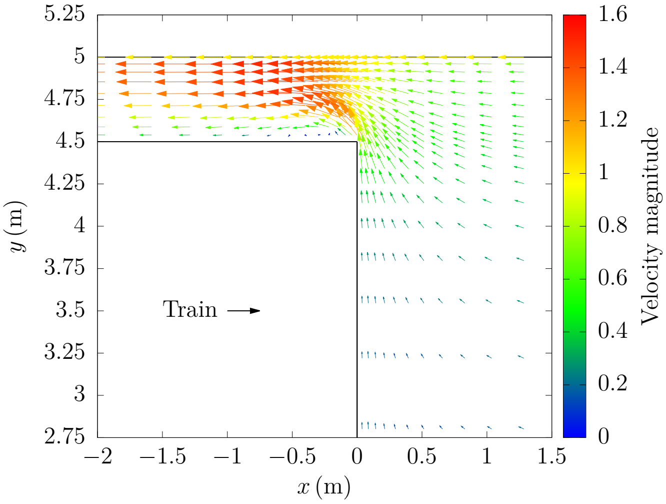

(a) $Re_{max} = 5.134 \times 10^4$.

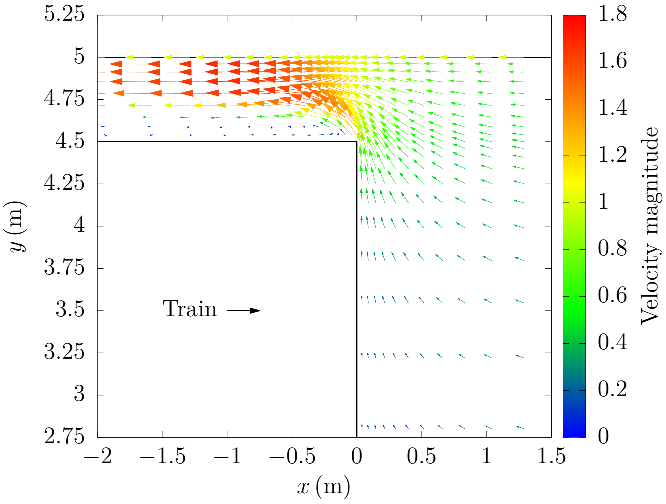

(b) $Re_{max} = 1.314 \times 10^7$.

Figure 4.7: Velocity vectors around the front of the train in the $x = 0\,\mathrm{m}$ plane at $T^+ = 0.5$.

behaviour is observed. The air flow through the train-tunnel gap is stronger, and as such the recirculating region at the corner of the train is larger and extends further along the side of the train.

4.5.2.2 TRAIN DRAG COEFFICIENT

The transient train drag coefficient and the average drag coefficient as a function of Re_{max} for model M_2 are shown in Figure 4.8 for the cases detailed in Table 4.3.

Transient drag coefficients from the variation of Re_{max} are given in Figure 4.8(a) during and after train movement. The pattern of behaviour is the same for all cases.

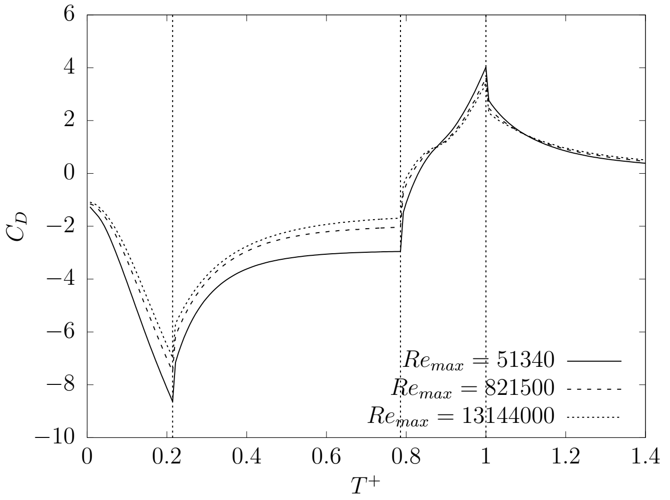

(a) Transient train drag coefficient (C_D).

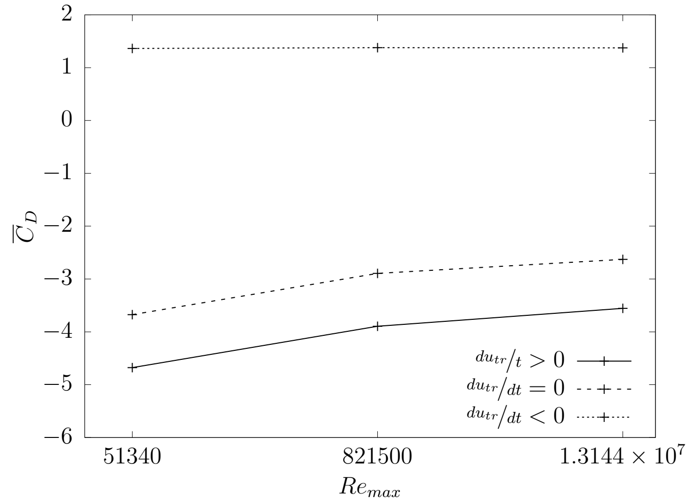

(b) Average train drag coefficient ($\overline{C}_D$) as a function of Re_{max}.

Figure 4.8: Train drag coefficients for model M_2 for various Re_{max}.

During acceleration, the train experiences a significant negative drag as the train works to overcome the inertia of the air. Once the train has reached its maximum velocity then the negative drag slowly reduces asymptotically towards what appears to be a stable value, which is due to the inertia of the air in the tunnel having been overcome. The reduction is also due to the volume of air the train is forcing forwards, reduces as the train approaches the tunnel outlet. Finally, almost instantly after the point of deceleration, the drag experienced by the train becomes positive as the body of air behind the train exerts a positive force upon the train, due to the momentum of the air behind the train. The train continues to experience a positive drag after the train has stopped after $T^+ = 1.0$, which is due to the continuing movement of air past the train.

Figure 4.8(b) shows the average drag coefficient for the acceleration ($^{du_{tr}}/_{dt} > 0$), cruising ($^{du_{tr}}/_{dt} = 0$) and deceleration ($^{du_{tr}}/_{dt} < 0$) phases of motion, as a function of Re_{max}. The average drag coefficient in the acceleration and cruising phases decreases at the same rate with increasing Re_{max} with the average drag being consistently higher in the acceleration phase, as the train in having to overcome the inertia in the tunnel air. The drag in the deceleration phase does not vary in any meaningful way for any Re_{max}.

The drag decreases with increasing Re_{max} for two reasons relating to the stronger flow of air through the train-tunnel gap. First, the effect of pressure drag on the train front decreases and secondly the effect of friction on the train side also decreases.

4.5.2.3 TUNNEL OUTLET VELOCITIES

The transient outlet velocity coefficient for model M_2 are shown in Figure 4.9 for the cases detailed in Table 4.3. Additionally, the outlet velocity coefficient and the train-tunnel gap velocity coefficient are shown as a function of Re_{max} at end end of the acceleration and cruising phases.

With increasing Re_{max}, the velocity coefficient shown in Figure 4.9(a) indicates a slower rate of increase during the velocity rise induced by the acceleration. At $T^+ = 0.75$, the maximum outlet velocity is reached and the coefficient is similar for all the cases investigated. During the deceleration, the coefficient initially indicates little variation between the Reynolds numbers until the flow though the train-tunnel gap region changes direction, due to the air behind the train having a higher velocity than the train such that it is moving from the back to the front and the outlet velocity is greater for higher Re_{max}. Once the train has stopped, there is an increasingly oscillatory behaviour at the outlet at higher Re_{max} due to the larger volume of air passing through the train-tunnel gap region towards the train front.

Figure 4.9(b) shows the outlet velocity coefficient and train-tunnel gap velocity

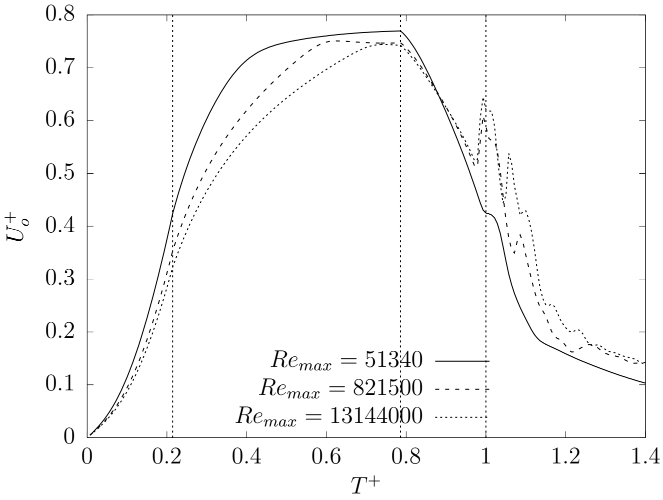

(a) Transient outlet velocity coefficient (U_o^+).

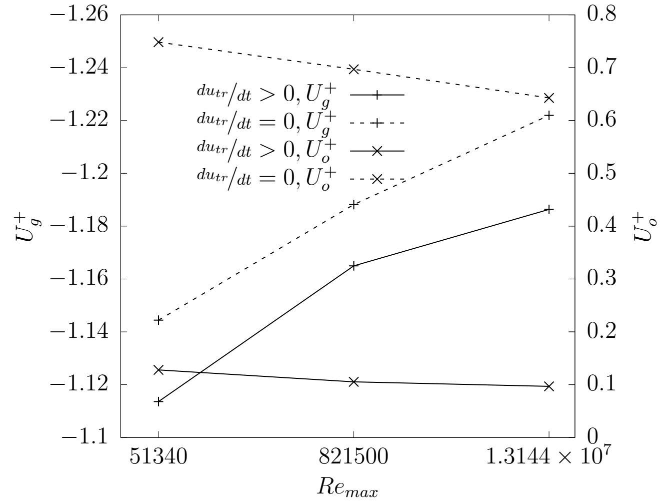

(b) Tunnel outlet (U_o^+) and train-tunnel gap (U_g^+) velocity coefficients.

Figure 4.9: Tunnel outlet and train-tunnel gap velocity coefficients for model M_2 for various Re_{max}.

coefficient at the end of the acceleration and cruising phases of motion as a function of Re_{max}. The train-tunnel gap velocity coefficient is expressed as $^{u_{rel}}/_{u_*}$ where u_{rel} is the velocity relative to the train in the train-tunnel gap and u_* is a reference velocity, in this case the maximum velocity of the train. During the acceleration phase, the train-tunnel gap velocity coefficient strengthens. The stronger flow of air through the train-tunnel gap reduces the outlet velocity coefficient, but not significantly, as was observed in Figure 4.9(a). During the cruising phase, the flow through the train-tunnel gap strengthens and the outlet velocity coefficient decreases more significantly than observed in the acceleration phase.

The ability for air to pass through the train-tunnel gap therefore determines the flow of air through the tunnel outlet. Moreover, the drag experienced by the train is also dependent on the magnitude of the air flow through the gap.

4.5.2.4 VISCOUS AND PRESSURE DRAG

Figure 4.10 shows the average pressure and viscous drag coefficients as a function of Re_{max} for model M_2 for the cases detailed in Table 4.3.

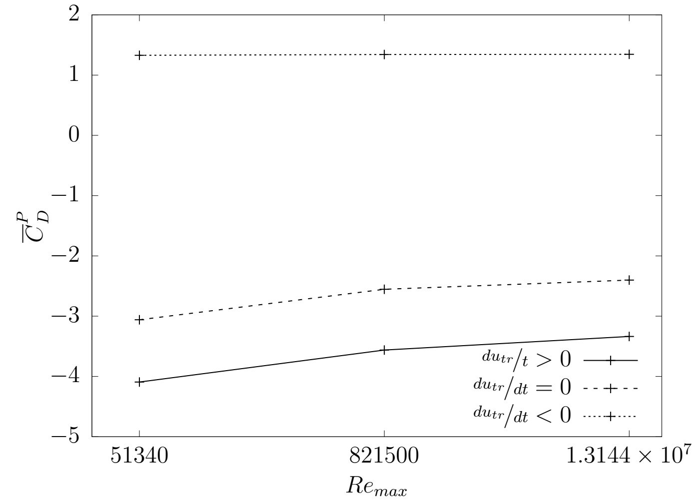

(a) Average train pressure drag coefficient ($\overline{C}_D^P$).

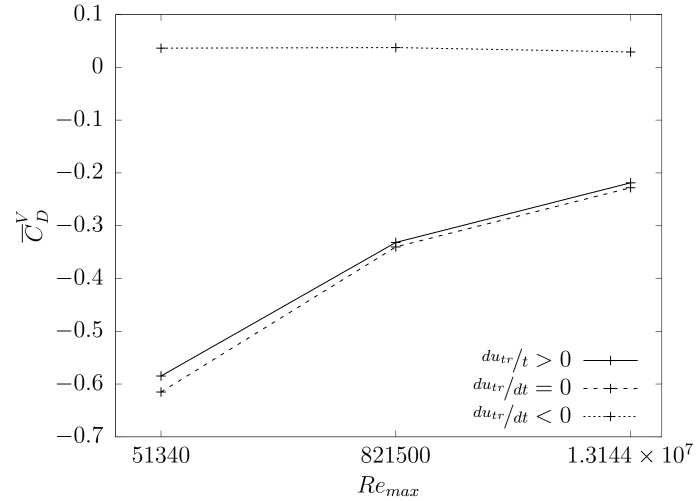

(b) Average train viscous drag coefficient ($\overline{C}_D^V$).

Figure 4.10: Average pressure and viscous drag coefficients for model M_2 as a function of Re_{max}.

The drag acting upon the train is made of two components, pressure drag and viscous, or friction, drag. The pressure drag is formed due to the air flow acting perpendicular to the surfaces of the train, while the viscous drag is formed from the effect of the air passing parallel to the surfaces of the train. In this case, due to the regular shape of the train, the pressure drag generally acts on the front and back of the train while the viscous drag acts on the sides of the train. The drag coefficients in Figure 4.10 are calculated using equation (4.4) and substituting the pressure and viscous forces for F_x, to give the pressure (C_D^P) and viscous (C_D^V) drag coefficients.

The pressure drag coefficients, shown in Figure 4.10(a), decrease with increasing Re_{max} during the acceleration and cruising phases of the train. This is due to the increase in air flow through the train-tunnel gap reducing the pressure on the front of the train. The decrease in the pressure drag coefficient towards the highest value of Re_{max} is less significant as the pattern of the behaviour of the air flows around the train do not change significantly. The pressure drag coefficient is lower during the cruising phase, as the inertia of the air has been overcome. During the deceleration phase, the pressure drag coefficient does not vary significantly.

The viscous drag coefficients, shown in Figure 4.10(b), decrease with increasing Re_{max} during the acceleration and cruising phases. The decrease in viscous drag coefficient is around 50%, compared with the pressure drag coefficient which decreased by around 25%. The decrease in the viscous drag coefficient is due to the increasing air flow through the train-tunnel gap, which causes the boundary layer thickness and therefore shear force on the train surfaces to reduce [41]. Although the viscous drag coefficient decreases more significantly than the pressure drag coefficient, the effect is of less significance as the viscous drag makes up about 10% of the total drag acting upon the train.

In practice a train is made up of several carriages with the gap between the carriages creating discontinuities in the side surfaces of the train. The discontinuities would have most significant influence on the viscous drag, as the boundary layer development on the side of the train would be interrupted. However, as the viscous drag makes up about 10% of the total drag acting upon the train, the omission of the discontinuities in the scaled model does not undermine the validity of the results.

4.6 TRAIN AND TUNNEL LENGTH VARIATION

The length of the train (x_{tr}) and tunnel (x_t) in model M_2 with $Re_{max} = 8.215 \times 10^5$, detailed in Table 4.3, were varied separately to examine the effect on the airflows and train drag. The model M_2 was chosen as this would allow comparison with a validated model and the specific Re_{max} case was selected as a compromise between a higher velocity, for realism, and the reduction in computational expense.

The train length was fixed at 60 m and x_t increased to 1170 m and 1560 m. The tunnel length was then fixed at 1170 m and the train length increased to 90 m, 120 m and 150 m. These cases are referred to as $M_2(x_{tr}, x_t)$ with appropriate values of x_{tr} and x_t

4.6.1 EFFECT ON DRAG AND VELOCITY

The results obtained from variations in the tunnel and train lengths are presented at the end of the acceleration ($^{du_{tr}}/_{dt} > 0$) and constant velocity ($^{du_{tr}}/_{dt} = 0$) phases of the train motion, shown in Figure 4.11.

The transient patterns of the train drag and outlet velocity coefficients during the train motion are similar to those presented for model M_2, shown in section 4.5.2, and so are omitted. In this section the trends during the acceleration and constant velocity phases are highlighted as representative of the flow.

Figure 4.11(a) shows the behaviour for variations of train length. Increasing the train length increases the tunnel outlet velocity during both phases of motion. Doubling the train length results in a 30% increase in air velocity during the acceleration phase and a 6% increase during the constant velocity phase. During the acceleration phase there is an increase in drag of about 7.5% while during constant velocity there is an increase of 8%.

Figure 4.11(b) shows the behaviour for variations of tunnel length. Doubling the tunnel length decreases the tunnel outlet velocity by about 35% during the acceleration phase and increases the drag by 45%. During the constant velocity phase the changes are less significant with a decrease of about 8% in outlet velocity and an increase of 37% in drag.

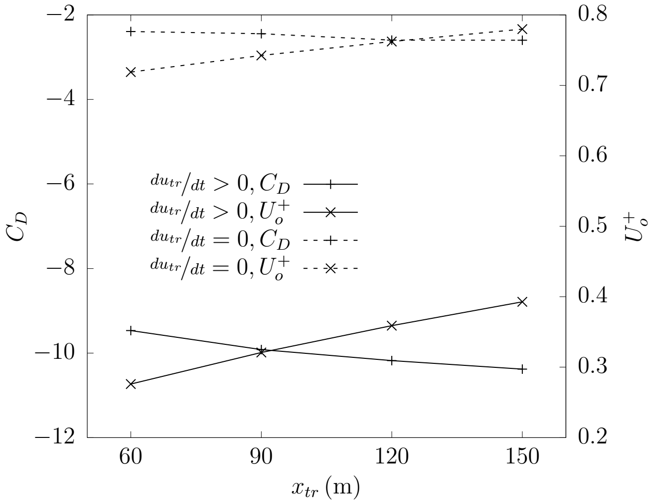

(a) Train length variation.

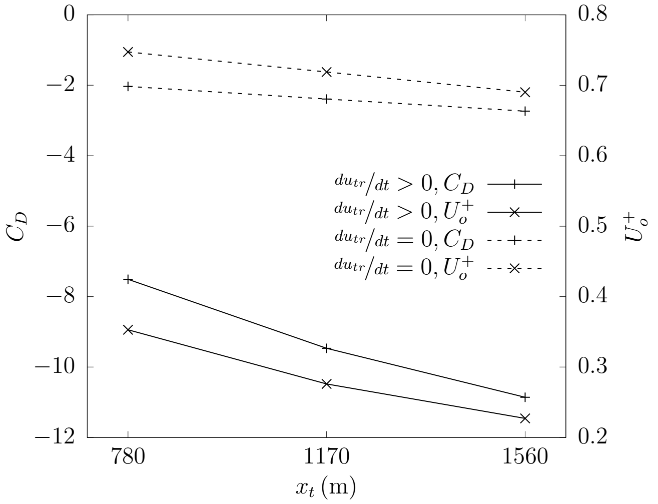

(b) Tunnel length variation.

Figure 4.11: Train drag (C_D) and outlet velocity (U_o^+) coefficients for train and tunnel length variation for model M_2 with $Re_{max} = 8.215 \times 10^5$.

The changes in the outlet velocity coefficients are less significant in the cruising phase than in the acceleration phase for two reasons. First, the inertia of the air has been overcome while in the cruising phase, and second, the volume of air ahead of the train is reduced towards the end of the acceleration phase. Increasing the train length has a small influence on the drag in both the acceleration and cruising phases of motion while increasing the tunnel length increases the drag significantly. This indicates that the effect of pressure forces are more significant then viscous forces for the overall drag force.

4.6.2 Viscous and pressure drag

Figure 4.12 shows the pressure and viscous drag coefficients for the various train and tunnel lengths at the end of the acceleration and constant velocity phases.

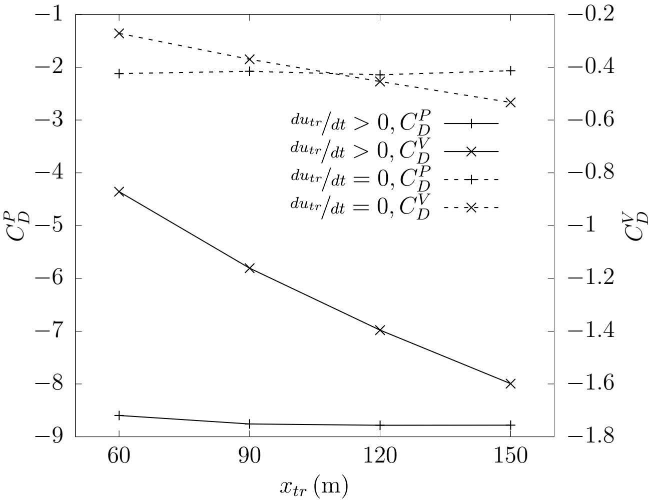

(a) Train length variation.

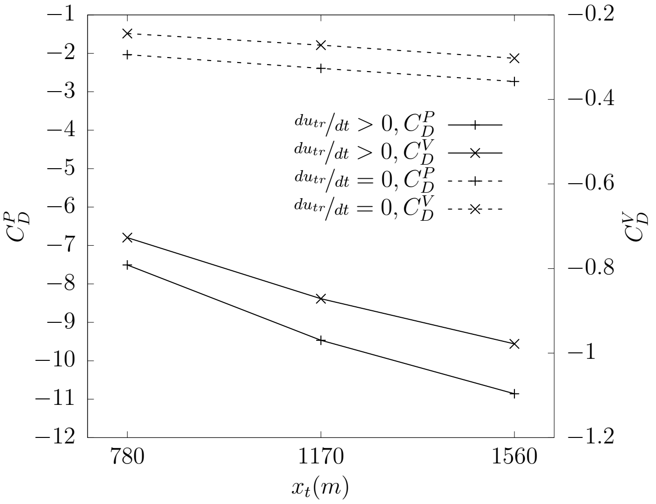

(b) Tunnel length variation.

Figure 4.12: Train pressure (C_D^P) and viscous (C_D^V) drag coefficients for train and tunnel length variations for model M_2.

Figure 4.12(a) shows the pressure and viscous drag coefficients for various train lengths. It can clearly be seen that the pressure drag does not change significantly during either phase of motion. This is due to the train frontal area and the cross sectional area of the train-tunnel gap being constant and the volume of air opposing the train being largely similar. There are larger changes in the viscous drag which increase significantly due to the larger surface area of the train sides. As there is a longer train-tunnel gap, this creates more resistance to the air flow from the train front to back, hence increasing the tunnel outlet velocity, during the acceleration and cruising phases. The small increases in pressure drag are due to the increased viscous drag, a form of drag known as viscous pressure drag [135]. As the longer train-tunnel gap restricts the flow of air down the side of the train, this viscous property contributes to the pressure drag.

Figure 4.12(b) shows the pressure and viscous drag coefficients for tunnel length variations. The pressure drag coefficient increases with longer tunnel lengths due to the greater air volume ahead of the train, which acts to increase the pressure on the train front. The viscous drag coefficient also increases due to the increased flow of air through the train-tunnel gap, and increasing shear force on the train sides. The flow through the train tunnel gap increases due to the higher pressure gradient between the front and back of the train, due to the increased pressure on the train front.

4.6.3 Air displacement

The total air displacement for various train lengths are shown in Table 4.4, for a tunnel length of 1170 m.

Table 4.4: Total air displacement for various train lengths.

x_{tr}	V (m^3)	$^V/_{V_t}$
60	12314.36	0.501
90	12538.92	0.510
120	12538.84	0.510
150	12552.67	0.511

The air displacement is calculated at the tunnel outlet and integrated over time, to find the total volume of air displaced from the tunnel.

Generally the proportion of tunnel air displaced from the outlet is about 50% of the total tunnel volume. Increasing the train length by 250% from 60 m to 150 m results in a very small increasae in displaced air volume (about 2%).

The total air displacement for various tunnel lengths are shown in Table 4.5. In this case the length of the train is 60 m.

Table 4.5: Total air displacement for various train lengths.

x_t	V (m^3)	$^{V}/_{V_t}$
780	8156.49	0.498
1170	12314.36	0.501
1560	16294.60	0.497

Again the proportion of tunnel air displaced from the outlet is about 50% of the total tunnel volume. Increasing the train length by 100% from 780 m to 1560 m results in an almost negligible increase in air displacement.

4.7 Geometric alternation

The scaled geometry, model M_2, with the train and tunnel lengths of 120 m and 1170 m respectively, was used as a reference case (denoted as $M_2(120, 1170)$) for geometric scaling in order to represent an underground railway configuration in accordance with systems found in the UK. The scaling was carried out in the y and z dimensions, as shown in Figure 4.1, which were scaled by a factor of 0.6238. This scaling process preserved the blockage ratio, at about 0.65. This model is referred to as model M_3, which has certain parameters similar to a current underground railway operating at a high blockage ratio (Victoria Line, London Underground, UK) [133, 97]. To consider the effect of the scaling on the train drag and outlet velocity coefficients the maximum train velocity, rate of acceleration and deceleration and travel time were altered to allow for comparison with the $Re_{max} = 8.215 \times 10^5$ case with model $M_2(120, 1170)$. The parameters are shown in Table 4.8.

4.7.1 Flow patterns

The air flow around the front of the train, and in the train-tunnel gap between the train side and tunnel wall, are illustrated by velocity vectors in Figure 4.13.

The air flow patterns around the train in models M_2 and M_3 appear to be similar in behaviour. However, there is a significant difference is in the magnitude of the

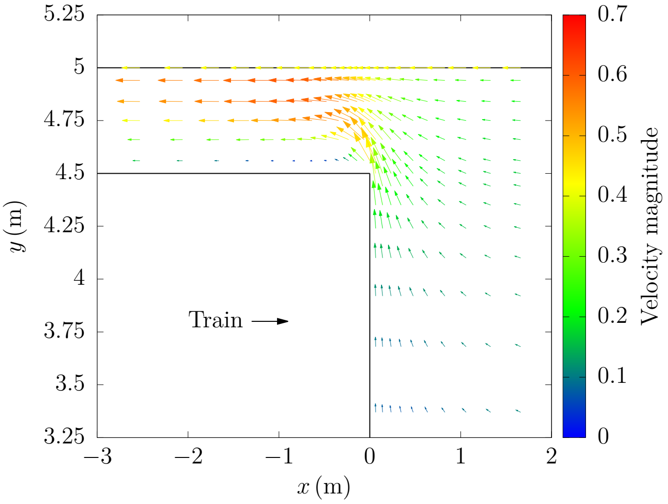

(a) Model M_2.

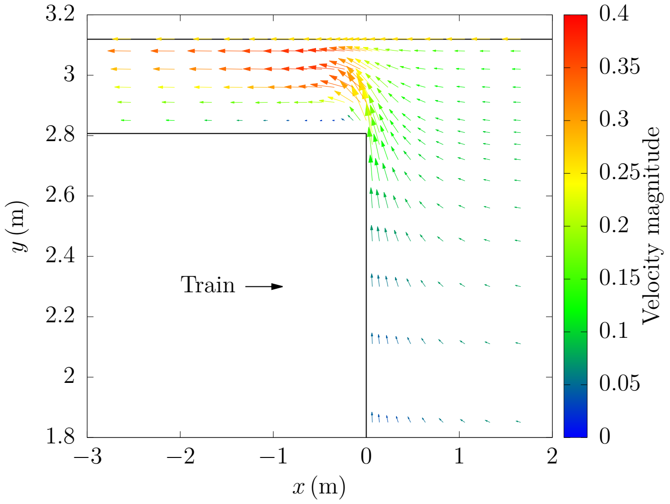

(b) Model M_3.

Figure 4.13: Velocity vectors around the front of the train in the $x = 0\,\mathrm{m}$ plane at $T^+ = 0.5$ with $Re_{max} = 8.215 \times 10^5$.

air flow through the train-tunnel gap, which has a maximum of about 0.7 in model M_2 and 0.4 in model M_3.

4.7.2 Drag and velocity

Table 4.6 shows the average drag coefficient for model M_2 and M_3 with $Re_{max} = 8.215 \times 10^5$, for the acceleration and cruising phases.

The drag coefficient is greater in models M_3 than M_2 in both phases. As the flow of air through the train-tunnel gap is lower in model M_3 than M_2, this leads to

Table 4.6: Average train drag ($\overline{C}_D$) for models M_2 and M_3.

	$\overline{C}_D$	
	M_2	M_3
${}^{du}\!/\!_{dt} > 0$	-5.74	-6.31
${}^{du}\!/\!_{dt} = 0$	-3.32	-4.21

an increase in the drag in two ways. First the train must displace a higher air flow towards the tunnel outlet and secondly, the reduction in air flow relative to the train in the train-tunnel gap increases the effect of viscous drag, due to the narrower train tunnel gap.

Table 4.7 shows the outlet velocity coefficient for model M_2 and M_3 with $Re_{max} = 8.215 \times 10^5$, at the end of the acceleration and cruising phases.

Table 4.7: Outlet velocity coefficient (U_o^+) for models M_2 and M_3.

	U_o^+	
	M_2	M_3
${}^{du_{tr}}\!/\!_{dt} > 0$	0.37	0.40
${}^{du_{tr}}\!/\!_{dt} = 0$	0.76	0.75

The outlet velocity coefficient is higher in model M_3 during the acceleration phase due to the lower air flow through the train tunnel gap. The outlet velocities in the cruising phase are essentially similar.

4.7.3 Re_{max} VARIATION

A process of Re_{max} variation was performed on model M_3, with the parameters shown in Table 4.8. The Reynolds number scaling was performed for a second time to investigate the effects of the M_2 to M_3 scaling.

4.7.3.1 TRAIN DRAG COEFFICIENT

The drag coefficients for model M_3 for various Re_{max} cases are shown in Figure 4.14.

Table 4.8: Reynolds number scaling parameters for model M_3.

Case (Re_{max})	u_{tr}^{max} (ms^{-1})	$^{du_{tr}}/_{dt}$ (ms^{-2})	t_T (s)
5.1245×10^5	2.4000	± 0.032000	487.500
8.2150×10^5	3.8474	± 0.082236	304.317
4.1000×10^6	19.2000	± 2.048000	60.938
4.1000×10^6	19.2000	± 1.000000	70.763

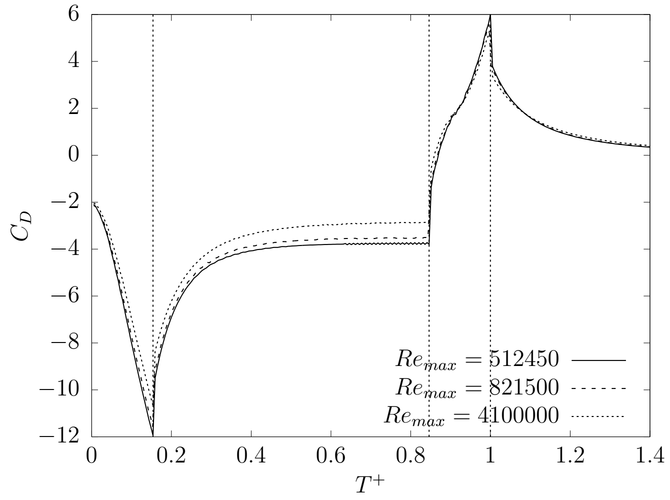

(a) Transient train drag coefficient (C_D).

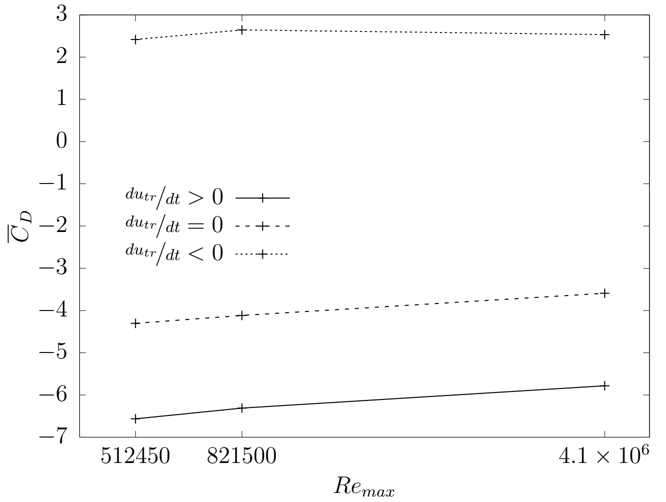

(b) Average train drag coefficient ($\overline{C}_D$) as a function of Re_{max}.

Figure 4.14: Train drag coefficients for model M_3 for various Re_{max}.

With increasing Re_{max}, the drag coefficient shows similar changes as for the M_1 to M_2 scaling. However, the changes in the drag coefficient are not significant. This is due to the small cross sectional area of the train-tunnel gap, which restricts changes in the flow air air with increasing Re_{max}.

4.7.3.2 Tunnel Outlet Velocities

The outlet velocity coefficients for model M_3 for various Re_{max} cases are shown in Figure 4.15.

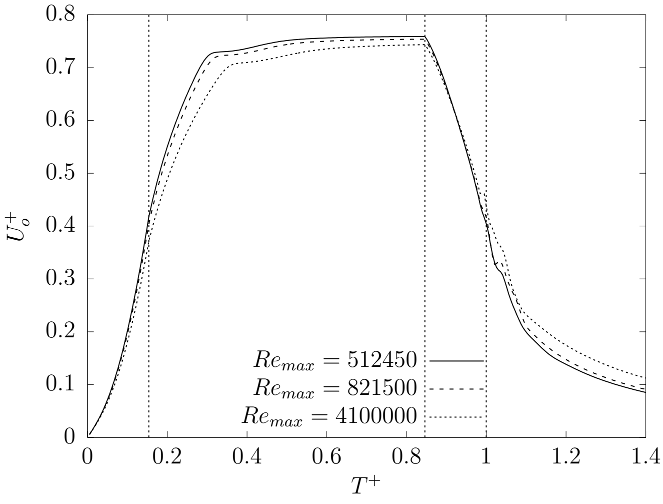

(a) Transient outlet velocity coefficient (U_o^+).

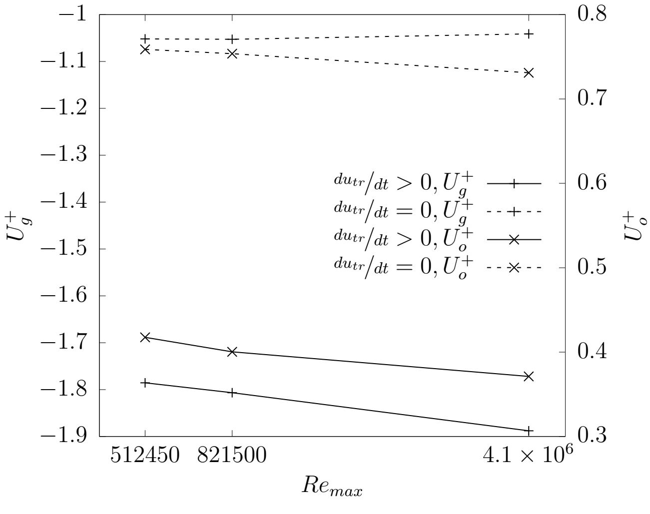

(b) Tunnel outlet (U_o^+) and train-tunnel gap (U_g^+) velocity coefficients.

Figure 4.15: Outlet velocity coefficients for model M_3 for various Re_{max}.

The behaviour of the tunnel outlet velocity coefficient follows a similar trend for each case, as shown in Figure 4.15(a). The smaller train-tunnel gap means that the tunnel outlet velocity reaches the maximum value rapidly for each Re_{max} case and this is in contrast to that observed in the model M_2. There is no oscillatory behaviour observed after the deceleration phase, which was found at high Re_{max} for model M_2. This is due to the smaller train-tunnel gap restricting the flow of air from the back of the train to the front. Figure 4.15(b) shows the outlet and train-tunnel gap velocity coefficients as a function of Re_{max}. The decreasing outlet velocity is observed which is caused by the simultaneous increase in train-tunnel gap velocity. Although the range of Re_{max} is large, the changes in velocity coefficients are not significant.

4.7.3.3 DISPLACED AIR VOLUMES

The total volume of air displaced from the tunnel outlet during the train motion is shown in Table 4.9. The total volume of displaced air is also expressed as a fraction of the tunnel volume, ${}^{V}\!/_{V_t}$.

Table 4.9: Total displaced air for model M_3.

Case (Re_{max})	V (m^3)	${}^{V}\!/_{V_t}$
5.1245×10^5	4977.06	0.521
8.2150×10^5	4956.74	0.518
4.1000×10^6	4901.25	0.513

The displaced air volumes are largely the same for models M_2 and M_3, at about 0.5 of the tunnel volume, although there is a moderate decrease at the higher Re_{max} cases. This shows that the ventilating air flows are not significantly affected by the velocity of the train nor upon the size of the train and tunnel as the value for M_2 is 0.510.

4.8 VARIATION OF ACCELERATION/DECELERATION RATE

The acceleration/deceleration rate for the $Re_{max} = 4.100 \times 10^6$ case in Table 4.8 is altered to represent a more realistic value of $\pm 1\,\mathrm{ms}^{-1}$, as the higher rate is not representative of an actual underground railway. In this case the rate of acceleration and deceleration results in the train spending a longer period of time in these phases of travel, as a proportion of total travel time.

The impact of variations in ${}^{du_{tr}}\!/_{dt}$ are presented in Figure 4.16 in terms of train drag and outlet velocity coefficients.

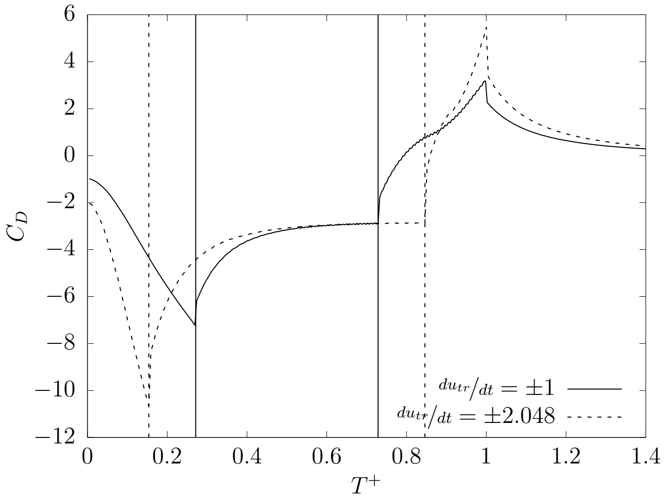

(a) Train drag coefficient (C_D).

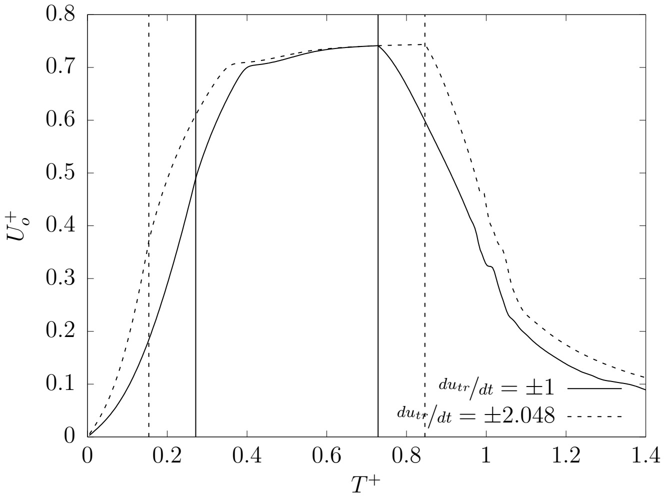

(b) Outlet velocity coefficient (U_o^+).

Figure 4.16: Results for ${}^{du_{tr}}\!/_{dt}$ variations for model M_3 with $Re_{max} = 4.100 \times 10^7$.

The solid and dashed vertical lines in Figure 4.16 indicate the start of the acceleration and deceleration phases for cases ${}^{du_{tr}}\!/_{dt} = \pm 2.048$ and ${}^{du_{tr}}\!/_{dt} = \pm 1$, respectively. The proportion of time which the train is accelerating and decelerating increases for the ${}^{du_{tr}}\!/_{dt} = \pm 1$ case. This is due to the acceleration and deceleration phases taking more than double the time in the ${}^{du_{tr}}\!/_{dt} = \pm 1$ case than in the ${}^{du_{tr}}\!/_{dt} = \pm 2.048$ case and that the time taken for the constant velocity phase reduces in the ${du_{tr}}/{dt} = \pm 1$ case.

Figure 4.16(a) shows the drag coefficient during the train motion. For ${du_{tr}}/{dt} = \pm 2.048$, the increase in the magnitude of the drag coefficient during the acceleration phase is more rapid and reaches a maximum value 48% greater than that in the ${du_{tr}}/{dt} = \pm 1$ case. Both cases reach a similar value during the constant velocity phase. During deceleration, the ${du_{tr}}/{dt} = \pm 2.048$ case again sees a more rapid increase in drag and reaches a higher value than the ${du_{tr}}/{dt} = \pm 1$ case, however the differences between the two cases in this phase are less significant. The faster rate of acceleration and deceleration for the ${du_{tr}}/{dt} = \pm 2.048$ case means that the overall tunnel velocities are higher, but not during the constant velocity phase. A higher rate of ${du_{tr}}/{dt}$ results in an increased tunnel air velocity for only a short period of time as shown in Figure 4.16(b).

The volumes of air displaced from the tunnel outlet as a proportion of the tunnel volume are 0.513 and 0.527 for the ${du_{tr}}/{dt} = \pm 2.048$ and ${du_{tr}}/{dt} = \pm 1$ cases, respectively. Although the ${du_{tr}}/{dt} = \pm 1$ outlet velocity does not reach a maximum value as fast as the ${du_{tr}}/{dt} = \pm 2.048$ case there is a higher overall volume displacement. However, this is due to the outlet velocity measurements being taken at a single point in the tunnel cross section. Overall the change is acceleration does not significantly effect the total displaced air volume.

4.9 Blockage Ratio Variation

The blockage ratio β was varied to investigate the effect on the train drag, tunnel air flows and the implications for tunnel ventilation. The model M_3 is used in this analysis since the dimensions correspond to an existing underground railway operating at high blockage ratio. The blockage ratio is defined as

$$\beta = \frac{A_{tr}}{A_t} \tag{4.7}$$

where A_{tr} and A_t are the cross sectional areas of the train and tunnel. The $Re_{max} = 4.100 \times 10^6$ case for model M_3 with a $1\,\mathrm{ms}^{-2}$ acceleration/deceleration rate is used as a base case, denoted as $\beta_{0.65}$ as the blockage ratio is around 0.65. The blockage ratio is varied following the parameters given in Table 4.10 and illustrated in Figure 4.17, where y_g and z_g are the y and z dimensions of the train-tunnel gap region between the train sides and tunnel walls, y_{tr} and z_{tr} are the y and z dimensions of the train and y_t and z_t are the y and z dimensions of the tunnel.

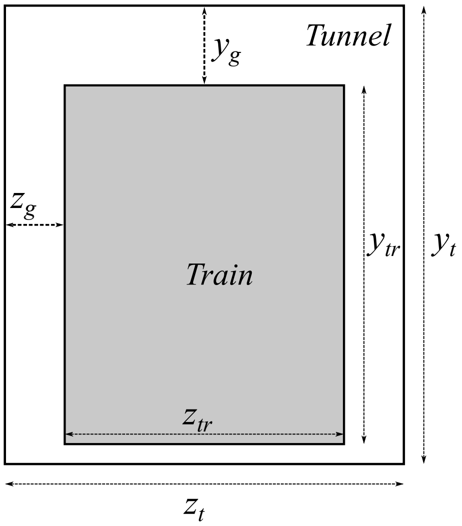

Figure 4.17: Diagram of blockage ratio variation parameters (cross sectional view in y-z plane).

Table 4.10: Blockage ratio variation parameters.

Model	y_g (m)	z_g (m)	β
$\beta_{0.65}$	0.3119	0.3369	0.65
$\beta_{0.75}$	0.2183	0.2358	0.75
$\beta_{0.78}$	0.1871	0.2021	0.78
$\beta_{0.85}$	0.1248	0.1347	0.85

As a train moves through a tunnel in an actual underground railway there are lateral movements in the z direction generated by the train motion. These changes in the lateral position of the train are not considered here and the train is positioned symmetrically in the z direction. The lateral movements induced by the train motion do not effect the blockage ratio of the train, hence the prediction of the volume of air displaced will not be adversely affected.

4.9.1 AIR FLOW PATTERNS

The air flow around the front of the train, and in the train-tunnel gap between the train side and tunnel wall, are illustrated as velocity vectors in Figure 4.18.

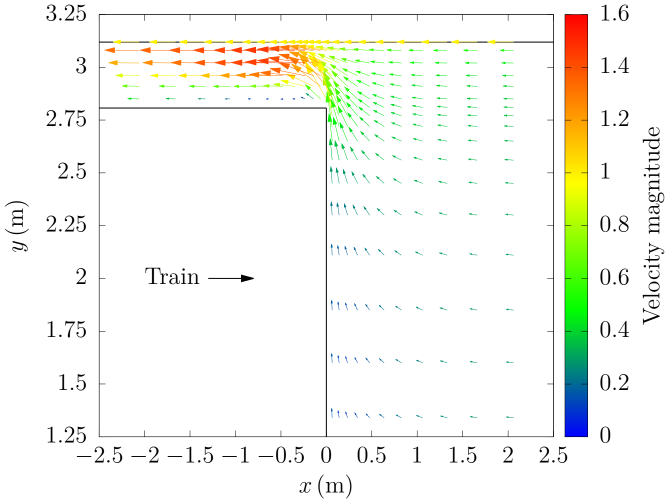

(a) $\beta = 0.65$.

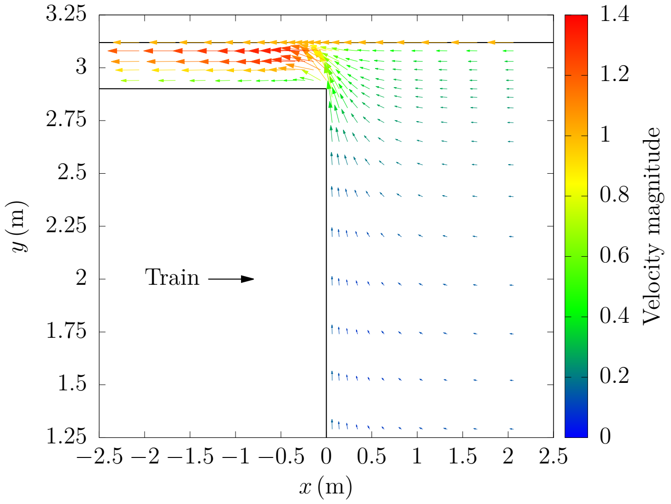

(b) $\beta = 0.75$.

Figure 4.18: Velocity vectors around the front of the train in the $x = 0\,\text{m}$ plane at $T^+ = 0.5$ for various blockage ratios.

Figure 4.18(a) shows the flow patterns for a blockage ratio of $\beta = 0.65$. The flow around the train and through the train-tunnel gap generates a small recirculating region at the blunt corner of the train. At a higher blockage ratio of $\beta = 0.75$, shown in Figure 4.18(b), the recirculating region has essentially been eliminated. The narrowing of the train-tunnel gap constricts the growth of the recirculating region. The air flow through the train-tunnel gap is reduced due to the increased constriction, and the increasing influence of friction from the train sides and tunnel wall. The maximum normalised velocity magnitude in the gap drops from 1.6 to 1.4.

4.9.2 Effect on Drag and Velocity

The train drag and tunnel outlet velocity coefficients during and after the train motion are shown in Figure 4.19.

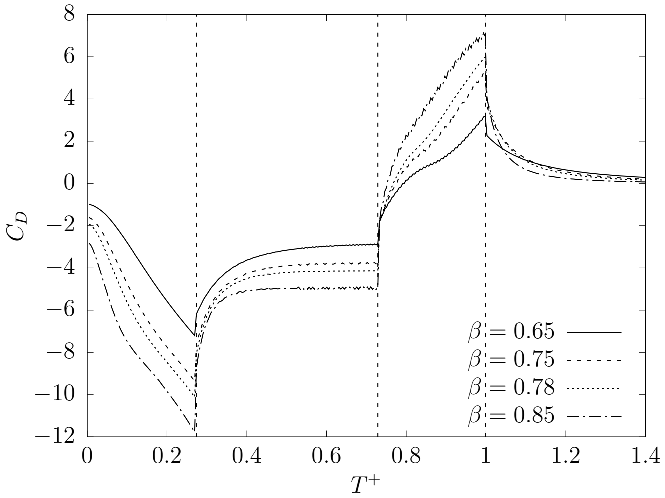

(a) Train drag coefficient (C_D).

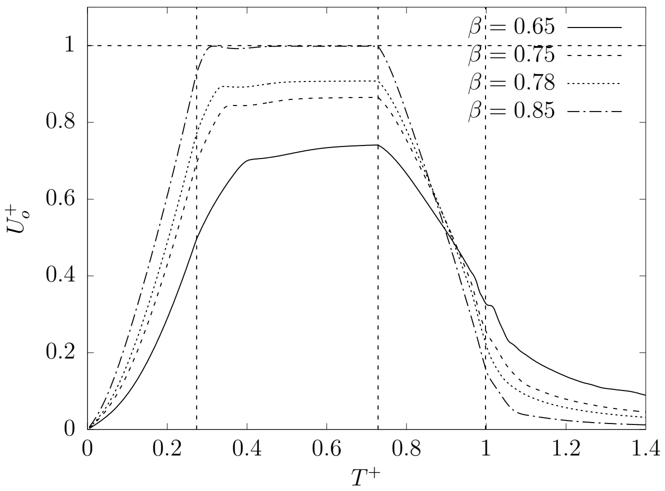

(b) Tunnel outlet velocity coefficient (U_o^+).

Figure 4.19: Train drag and tunnel outlet velocities for various blockage ratios.

The drag coefficient, shown in Figure 4.19(a), for each blockage ratio exhibits the same behaviour but with increased magnitude for higher blockage ratios. Increasing the blockage ratio from 0.65 to 0.85, a 30% increase, increases the drag experienced by the train through the whole period of travel. During the acceleration phase this means an increase in the average drag coefficient of 100%. During the constant velocity phase there is an increase of 49% in the average drag. During the deceleration phase, the train experiences an increased period of positive drag which would have to be opposed by the train brakes. The drag increases by a factor of 4 during the deceleration phase. During the constant velocity phase, the drag coefficient asymptotes to a constant value more rapidly, with increasing blockage ratio.

Tunnel outlet velocities, shown in Figure 4.19(a), also indicate a similar behaviour regardless of blockage ratio, but with increased magnitude. During the acceleration phase, higher blockage ratios mean that the maximum outlet velocity is reached more rapidly and the maximum attained velocity is higher. In the case of $\beta = 0.85$, this is close to the maximum train velocity, indicated by the horizontal line at $U_o^+ = 1$. During the constant velocity phase, an increase of 36% in the outlet velocity is observed for an increase in the blockage ratio from 0.65 to 0.85. During the deceleration phase, the outlet velocities decrease more rapidly at higher blockage ratios due to the train blocking the induced air flows from moving past the train to the outlet. Towards the end of the deceleration, the lower blockage ratio cases give higher velocities than the higher blockage ratio cases. This trend continues after the train has stopped. It is this behaviour which creates the higher positive drag coefficients during the deceleration phase.

4.9.3 PRESSURE DIFFERENCE

The pressure difference between the front and back of the train is shown in Figure 4.20. The pressure difference between the front and back of the train contributes to the pressure drag on the train. Additionally, the magnitude of the pressure difference is a result of the air flow through the train-tunnel gap.

The pressure difference during the acceleration phase increases for the duration of the phase. For higher blockage ratios, the pressure difference increases strongly. The

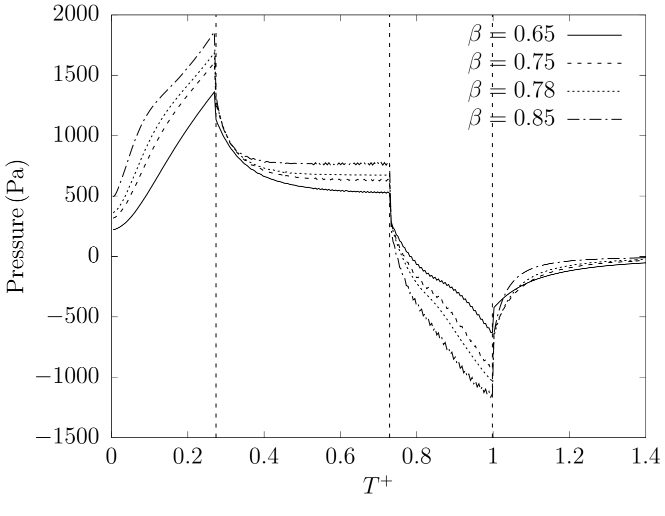

Figure 4.20: Pressure difference between the train front and back for various blockage ratios.

strong dependence on the blockage ratio during the acceleration phase indicates the dominance of pressure effects [135], due to the train acting to overcome the inertia of the air within the tunnel. The pressure difference drops rapidly at the end of the acceleration phase, and asymptotes towards a constant value. The higher blockage ratios tend towards a constant value more rapidly than lower blockage ratios. The pressure differences for all blockage ratios are in general lower during this phase, due to the train no longer acting to accelerate the air, and the greater influence of viscous effects. During the deceleration phase the direction of the pressure differences acts negatively, due to the moving body of air behind the train. As the train is slowing, this body of air acts upon the back of the train, thus creating a positive pressure on the back of the train. At higher blockage ratios, the greater induced air flows increases the magnitude of the pressure difference.

The changes in pressure throughout the train motion do not indicate that unsafe pressure changes are created at any blockage ratio. The safe level of pressure change is given by the International Union of Railways [72] as 4 kPa in a 4 s period. However, as the model used in this study is idealised and lacks any geometrical changes, in practice unsafe pressure changes may be generated.

4.9.4 Train-tunnel gap velocity

Figure 4.21 shows train-tunnel gap velocity coefficients for various blockage ratios.

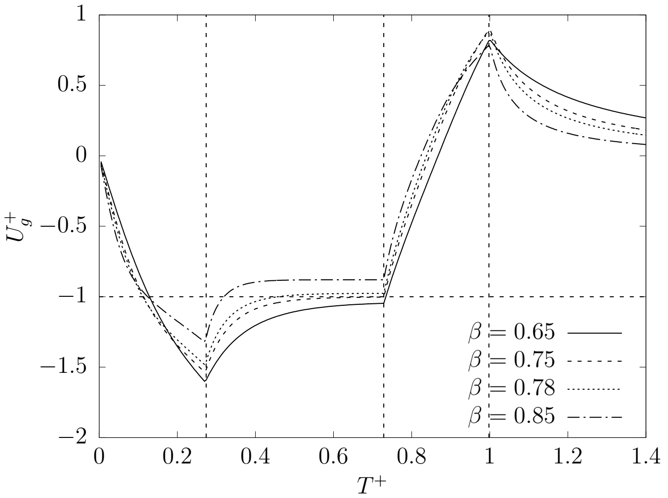

Figure 4.21: Train-tunnel gap velocity coefficients (U_g^+) for various blockage ratios.

The air flows through the train tunnel gap effect the pressure and viscous drag and the tunnel outlet velocity. A greater flow of air through the gap decreases the effect of pressure drag, and also reduces the outlet velocity. During the acceleration phase, there is initially only small differences between the various blockage ratios. Towards the end of the phase, the effect of friction decreases the flow of air through the gap, thus increasing the pressure difference and outlet velocity. The air flow during the cruising phase asymptotes to a constant value more rapidly at higher blockage ratios, reflecting the trend in pressure difference, drag coefficient and outlet velocity. The differences in the air flow are more significant than during the acceleration phase. During the deceleration phase, the differences are again smaller.

4.9.5 Viscous and Pressure Drag

The effect of the pressure difference and train-tunnel gap velocity can be highlighted though examination of the pressure and viscous components of train drag. Figure 4.22 shows the total drag coefficient decomposed into its pressure and viscous components given as averages across the three phases of motion.

During the acceleration phase, the pressure drag increases significantly, by about

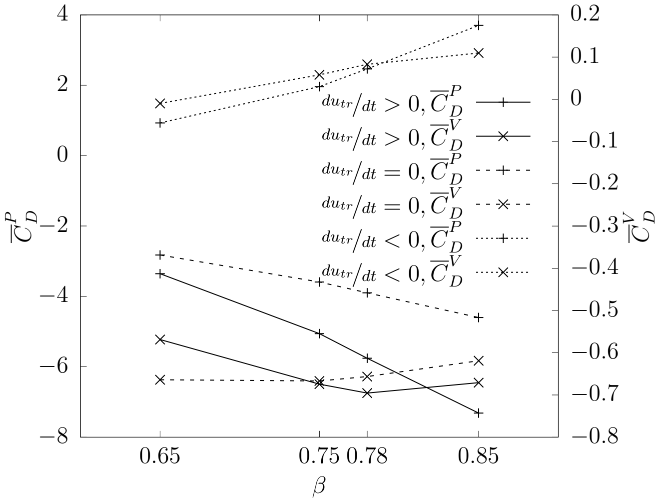

Figure 4.22: Average train pressure ($\overline{C}_D^P$) and viscous ($\overline{C}_D^V$) drag coefficients for various blockage ratios.

200% across the range of blockage ratios. The viscous drag, however, increases by only 25% up to $\beta = 0.78$, after which point decreases slightly. A similar pattern is observed during the cruising phase, although the changes are less significant with pressure drag increasing by around 160%. However, viscous drag does not increase, and drops slightly at about $\beta = 0.75$. The narrowing of the train-tunnel gap causes the increase in the magnitude of the pressure drag, but the reduction in air flow through the gap decreases the shear forces on the train sides, at about $\beta = 0.75$.

During deceleration, the increase in viscous drag is not significant as the air flow through the train-tunnel gap does not exhibit major changes. However, due to the constricted size of the train-tunnel gap, the effect on the pressure drag is therefore more significant.

4.9.6 Air displacement

Figure 4.23 shows the air volumes displaced from the tunnel and average drag coefficients for the three phases of the train motion. The air volumes and drag coefficients are also presented normalised by the respective value for the $\beta = 0.65$ case, denoted as V^* and $\overline{C}_D^*$, to allow for the changes to be compared.

The increase in air flow volume during the acceleration and constant velocity phases are most significant. The air flow volume during deceleration shows a fairly

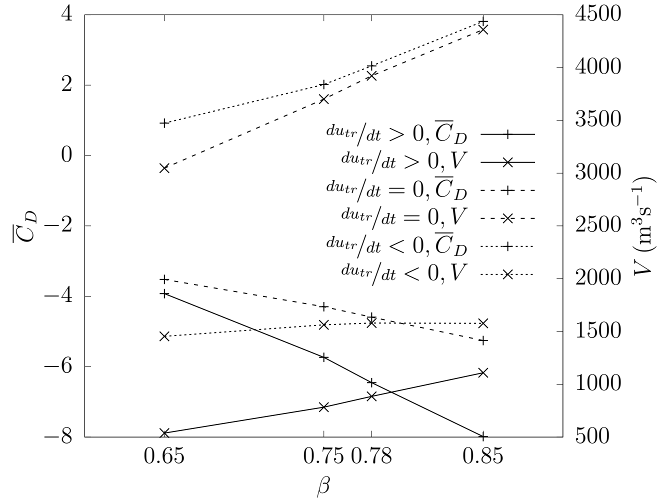

(a) Air displacement (V) and average train drag coefficient ($\overline{C}_D$).

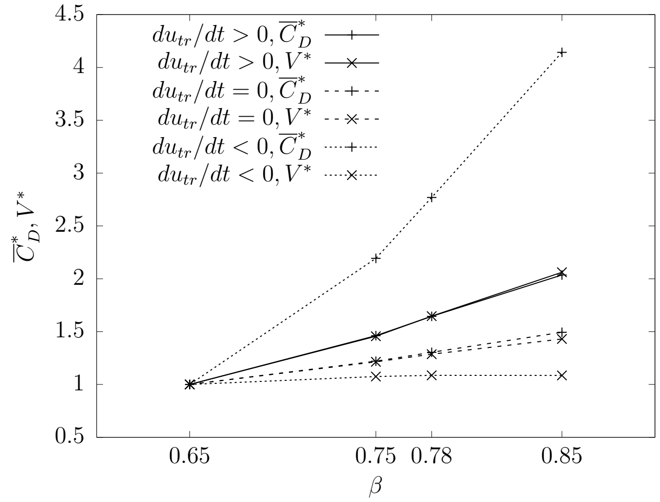

(b) Normalised air displacement and average train drag coefficient, (V^*) and ($\overline{C}_D^*$).

Figure 4.23: Tunnel outlet air displacement and the average train drag coefficient as functions of blockage ratio.

insignificant increase, and negligible increases during deceleration are observed after $\beta = 0.75$. This is due to the restricted size of the train-tunnel gap region constricting the flow of air from the back to the front of the train.

This shows that the drag and outlet air flow volumes increase in an almost identical manner during the acceleration and constant velocity phases but that the drag during deceleration increases very significantly (by about 400%) and that air flows show little change. Overall the air flow and drag increase by 200% during acceleration and by 40% during constant velocity.

Table 4.11 shows the total volume of air displaced from the tunnel outlet, also expressed as a fraction of the tunnel volume. As the blockage ratio is increased by 15%, from 0.65 to 0.75, the fraction of the tunnel volume displaced increases by 20%, from 0.52 to 0.63. A 30% increase in blockage ratio, from 0.65 to 0.85, increases air displacement by 40%, from 0.52 to 0.73. This implies a linear relationship between total air displacement and blockage ratio.

Table 4.11: Total air displacement for various β.

β	$V\,(\mathrm{m}^3)$	V/V_t
0.65	5039.40	0.527
0.75	6047.71	0.633
0.78	6387.44	0.668
0.85	7046.84	0.737

4.10 SUMMARY

In this chapter the transient, three-dimensional air flows in an underground railway have been modelled using computational fluid dynamics. A scale model was developed, based on published literature, and validated with available experimental data. The model was scaled geometrically and it was found that the flow behaviour was similar in both cases, thus demonstrating the validity of the numerical model. Reynolds number scaling was carried out to observe the behaviour of the air flows with similar trends found throughout the ranges tested.

The train and tunnel lengths were varied and it was found that both strongly influenced the air flows in the tunnel. The train total drag was strongly influenced by the tunnel length through increasing the pressure drag while the train length had a less significant impact, predominately increasing the viscous drag. A longer train was found to increase the tunnel outlet velocities by about 30% during the constant velocity phase while increasing the train drag by about 7.5%. Overall only small differences were found in air displacement from the tunnel outlet.

The effect of increasing the blockage ratio was found to increase the air velocities at the tunnel outlet almost to the train maximum velocity for $\beta = 0.85$. It was found that drag increases by about 50% during the constant velocity phase, 100% during acceleration and 300% during deceleration. Total air flow volumes displaced form the tunnel increase at broadly the same rate as the drag for acceleration and constant velocity phases. During deceleration, the increase in displaced air volume plateaus at around $\beta = 0.75$. The effect of pressure drag was found to be more significant than viscous drag.

The forces acting upon the train, the pressure difference across the train and the air velocities in the train-tunnel gap have been highlighted. The behaviour during deceleration is shown as being distinct from the other phases of travel; the body of air behind the train acts as a positive force upon it and air flows are restricted from moving from the back to the front of the train. This will create a force against which the train brakes will need to work. The positive drag also indicates that the train blocks the movement of air flows ahead of it, thus minimising the potential for ventilating flows.

In this chapter it has been shown that the alteration of the blockage ratio can increase ventilating air flows during train motion, and it has been also shown that there is an associated and proportional effect on the train drag. The different behaviour of the pressure and viscous drag components have also been shown, and related to the air flows around the train. The following chapter will consider how through changing the shape of the train the air flows around the train may be altered, to effect changes in the outlet velocity and the pressure and viscous drag.

5

Enhancing the piston effect by means of train shape alterations

5.1 INTRODUCTION

In Chapter 4 it was shown how the train and tunnel lengths and the blockage ratio determine the air displacement generated by a train moving through a tunnel. Moreover, the effect of these factors on train drag was also shown, in terms of both total train drag, and the pressure and viscous components.

The piston effect is an important factor in the ventilation of many underground railways, and a number of studies have considered the influence of ventilation and the piston effect upon underground railway temperatures and energy use. Ampofo et al. [3] considered various methods of delivering cooling in a UK underground railway system and show that increasing the ventilation rate can significantly reduce the temperature in tunnels and trains. Eckford & Pope [42] investigated increasing the ventilation rate using mechanical ventilation, train induced flows and draught relief and found that increasing the air exchange by 60%, by any means, reduced the temperatures by 4 °C. Gonzalez et al. [51] carried out a numerical investigation of the airflows in a station within a network of tunnels and shafts, and found that the influence of the piston effect could give energy savings of up to 3%. Yuan & You [149] carried out an experimental and numerical investigation of the air velocity and temperature conditions on an underground station platform and optimised the ventilation to give a lower platform temperature. Ono et al. [106] considered the operation of mechanical ventilation based on the scheduling of trains. Train induced air flows were found to be sufficient for ventilation for the majority of the day with mechanical ventilation only required at peak periods. Casals et al. [27] presented a breakdown of the energy consumption in a Barcelona underground station. The authors found that ventilation accounted for 14% of the energy consumption but believed that this could be reduced by 30% if the train induced air flows could be better harnessed for ventilation purposes.

The influence of train geometry upon the piston effect have been considered in terms of improving ventilation and reducing undesirable pressure effects. Ricco et al. [117] investigated, numerically and experimentally, the pressure waves generated by a train passing through a tunnel. They noted that the size of a separation bubble at the train nose increases the effective blockage ratio of the train, which in turn increases the pressure peaks, and is influenced by the shape of the nose. Gilbert et al. [49] carried out an experimental study into the gusts generated by trains in tunnels, finding that they are strongly dependent on the length and the cross sectional area of the tunnel. Choi & Kim [29] investigated increasing the nose length and cross sectional area of a tunnel to reduce the drag of a subway train with reductions of 50% found from either method.

In previous studies, the impact of the piston effect upon underground railway conditions and energy use have been investigated as well as the aerodynamics of trains in tunnels. The literature establishes that the piston effect benefits underground railway conditions and that the blockage ratio is a major influencing factor upon the air flows.

In this chapter a mechanism for increasing the train induced ventilating air flows, but which does not have a large negative effect upon the train aerodynamics, is investigated. Instead of increasing the absolute blockage ratio, alterations to the shape of the train front are made to effect a change in the air flows generated by a moving train. This is referred to as altering the aerodynamic resistance of the train. Through changing the shape of the train without increasing the blockage ratio, the aim is to increase air flows but with a reduced impact on train performance.

Two means of altering the aerodynamic resistance are presented in this chapter. The first is a train fin, positioned at the front of the train, within the train-tunnel gap. The fin increases the frontal blockage ratio of the train, but not the blockage ratio along the whole length of the train. The second means is a train aerofoil positioned within the train-tunnel gap, which alters the patterns of the air flows at the front of the train. The train fin and aerofoil are illustrated in Figure 5.1.

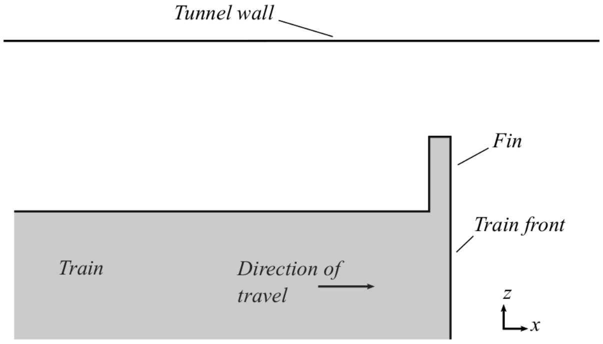

(a) Train fin.

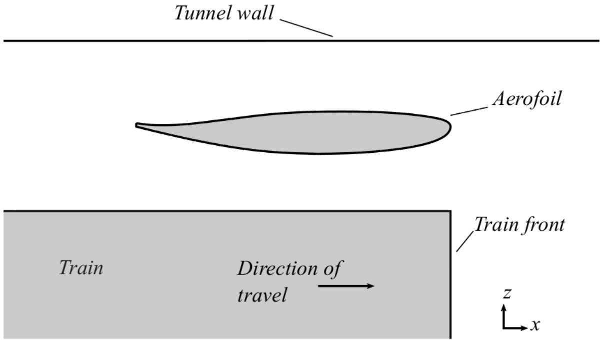

(b) Train aerofoil.

Figure 5.1: Sketches of a train fin and aerofoil positioned at the front of a train, between the train side and the tunnel wall.

Through varying the size of the train fin to block varying proportions of the train-tunnel gap, the effect of the fin on the air volumes displaced by the train, and the effect on train performance due to changes in the train drag can be determined. Similarly, by positioning the train aerofoil at a variety of angles, the effect on air displacement and performance may also be found.

In this chapter, first a benchmark numerical model of a train-tunnel configuration is developed and verified with available experimental data. The effect of varying the aerodynamic resistance using a train fin and aerofoil is studied with consideration given to the air displacement and aerodynamic work done by the train. The effect of the fin and aerofoil on the air flow patterns and pressure and viscous forces acting upon the train is shown. The effect of fin size and aerofoil angle and the implications of regenerative braking are discussed.

The aim of this chapter is to investigate the concept of using a fin or aerofoil to alter the air flows around a train for the purposes of enhancing the piston effect. Further aspects of a fin or aerofoil configuration will need to be considered further before application, including the size and position relative to the front and side of the train and how it may be accommodated within the constraints of a particular train-tunnel configuration. As such, the results are intended to provide insight into the effects of a fin or aerofoil on the air flows around trains for a general train-tunnel configuration, not a specific case.

Results obtained presented in this chapter were published, in part, in Cross et al. [35].

5.2 METHODOLOGY

A transient two-dimensional (2-d) computational fluid dynamics (CFD) simulation was used to model the induced air flows generated by the train movement in a tunnel. The work within this chapter consists of two parts; the verification and study of a benchmark configuration without a fin or aerofoil and the examination of the effect of a fin or aerofoil on the benchmark configuration.

5.2.1 Benchmark configuration

The benchmark modelling domain is a 2-d horizontal cross section of an idealised train-tunnel configuration. The model represents a train as a blunt ended rectangle positioned symmetrically between smooth tunnel walls, with the tunnel ends open to the atmosphere. The air flows around a train are 3-d in nature, in particular the air flows at the corners of a train will vary significantly from that between the corners. The 2-d model is used by assuming that the flow through the train gap does not vary significantly with the vertical position, away from the corners of the train. Moreover, the flows represented in the 2-d model are taken to represent the flows in a general train-tunnel configuration, not a specific case, and as such are considered sufficient for the purposes of this study. Additionally, a three-dimensional model of the train-tunnel configuration with an aerofoil would entail using a mesh of a prohibitively small size, given the computational resources available. The model is geometrically simple to avoid interference from other factors. Figure 5.2 shows the modelling domain and characteristic lengths.

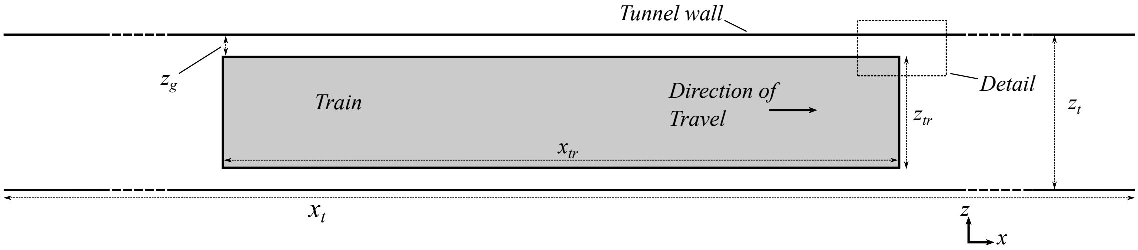

Figure 5.2: Schematic diagram of the modelling domain with characteristic lengths, also showing the aerofoils used in the aerofoil configuration.

The train length (x_{tr}) and width (z_{tr}) are 50 m and 2.48 m, respectively, and the tunnel length (x_t) and width (z_t) are 500 m and 2.96 m, respectively. The width of the gap between the train side and tunnel wall, the train-tunnel gap (z_g), is 0.24 m on each side, so that the train is positioned symmetrically within the tunnel. The length of the train allows the air flow though the train-tunnel gap to become fully developed and the tunnel length allows the transient changes in air flow behaviour to be observed. The dimensions are based on available data from the Victoria Line, London Underground, UK, a currently operating underground railway [132, 97].

The train is initially positioned with the rear of the train 10 m from the tunnel entrance portal. It is accelerated for 10 s at 1 ms^{-2}, travels at a cruising speed of 10 ms^{-1} for 32.5 s then decelerates for 10 s at -1 ms^{-2}. The final position of the train is with the front of the train 15 m from the tunnel exit portal. The total travel time and distance are 52.5 s and 425 m, respectively.

5.2.2 Mesh generation

The numerical mesh representing the modelling domain was created in Ansys ICEM CFD [12]. The mesh was formed in three regions; a near field region around the train and two far field regions to the front and rear of the train. The near field region was formed using a triangular cell mesh with a very high density of cells, particularly around the fins or aerofoils. The two far field regions required a less dense mesh and a quad cell mesh was used in this case. The boundary layers are resolved by using inflation layers at the walls throughout the three regions.

The numerical modelling of the air flow was performed using the Ansys Fluent commercial CFD software package [10]. The train movement was simulated using the dynamic layering option in the dynamic meshing component of Ansys Fluent, following the approach used by [69]. The movement of the train is achieved by the near field region moving forward at the specified train speed, defined by a user defined function (UDF), with layers of cells added to the far field region behind the near field region and removed from the region in front of the near field region. This process allowed the more complex near field region to remain unaltered with the only mesh changes occurring in the simpler far field regions. The use of dynamic layering is possible in the far field regions as they are formed of quad cell mesh [11].

5.2.3 Numerical conditions

For the unsteady, incompressible fluid flow in an underground railway, the Reynolds-averaged Navier Stokes equations are solved using Ansys Fluent. The k-ϵ RNG turbulence model is used in this work as it has been used previously for the investigation of train induced air flows where it performed well [143, 70]. Near wall modelling used the standard wall function, a wall function approach, to reduce the computational time in the transient calculations. The first cell height on the walls are chosen during mesh generation so that the non-dimensional y^* value is maintained in the recommended range of $30 \leq y^* \leq 300$. The time step for the unsteady calculation is set at 0.025 s, and this has been found to be a sufficient size through a time step independence study.

At the tunnel entry and exit portals, an outlet boundary condition of 0 Pa was applied. This is given relative to an operating pressure set as atmospheric pressure. This allows for the dynamic pressure to vary at the openings while the static pressure is fixed, such as when the train approaches an opening of the tunnel. This approach was used by Khayrullina et al. [84].

Ansys Fluent uses the finite volume method on an unstructured mesh to solve the governing equations. In this work the PISO pressure-velocity coupling method is adopted to solve the governing equations, the QUICK interpolation scheme is used for the discretisation of the convection terms and the PRESTO scheme to treat the pressure interpolation. This approach was used by Huang et al. [69]. The continuity, momentum, k and ϵ residual equations were monitored as the convergence criteria and set as 1×10^{-5}. A convergence criteria of 1×10^{-5} ensured that the changes in monitored flow quantities between iterations exhibited only small changes, while maintaining computational efficiency. A smaller convergence criteria showed minimal changes in flow quantities. Additionally, the velocity was monitored at various points within the domain as was the train drag. Mass conservation within the computational domain was also monitored to ensure conservation at every time step.

5.2.4 Alteration of the train shape

In order to change the air flows around the train, the train shape is altered by the addition of a train fin and aerofoil. These alterations are incorporated into the benchmark configuration and the mesh generated in a similar manner. A high density of cells was applied to the region around the fin and aerofoil to properly capture the behaviour of the flow in these regions.

5.3 VERIFICATION

The verification of the benchmark configuration was carried out using data from the work of Gralewski [53]. This study was an investigation of the flow behaviour in the train-tunnel gap. The author used a test rig consisting of a moving and stationary wall and a fan to generate a pressure gradient to simulate the conditions in a train-tunnel gap. A series of tests were carried out with a range of wall speeds and imposed pressure gradients. The verification presented here compares five of the experimental cases with points within the transient simulation. The five verification cases are within the cruising phase of the train motion at 13.25 s, 14.25 s, 15.50 s, 17.50 s and 23.00 s.

5.3.1 VELOCITY PROFILES

Figure 5.3 shows velocity profiles in the train-tunnel gap for the five verification cases.

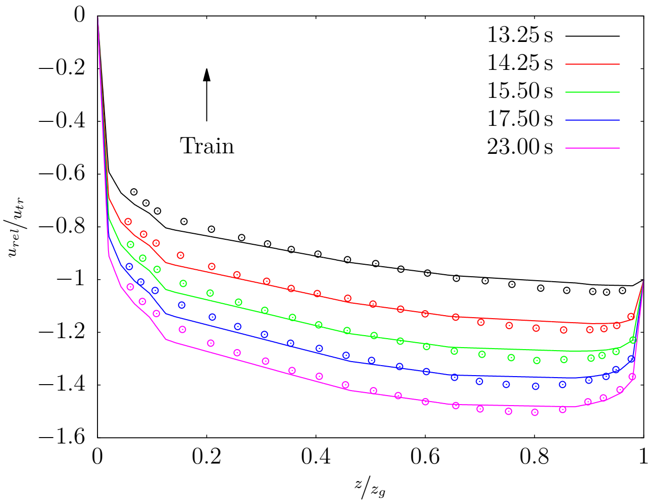

Figure 5.3: Velocity profiles between the train side and tunnel wall for the five verification cases (Numerical —, Experimental ∘). The arrow indicates the direction of train movement.

The velocity in Figure 5.3 is given as u_{rel}/u_*, where u_{rel} is the velocity of the air relative to the train and u_* is a reference velocity, in this case the velocity of the train. The profiles are presented as a function of the normalised distance between the train side and tunnel wall z/z_g, where $z/z_g = 0$ is at the train side and $z/z_g = 1$ is at the tunnel wall. The profiles from the numerical results are measured midway between the front and back of the train. The experimental and numerical results agree well for the five cases investigated. Particularly good agreement is found towards the tunnel wall with some slight deviation near the side of the train. The numerical model represented the cross section of a train in two dimensions, including the train ends, compared with the laboratory rig which simulated conditions in the train-tunnel gap, without the end effects. The small discrepancies between the numerical and experimental velocity profiles are in part due to the differences between the numerical and experimental configurations.

The velocity profiles shown in Figure 5.3 can be classified into two types; a type A which is driven by the pressure gradient along the train and opposed by the friction at the walls and a type B which is driven by the friction of the tunnel wall and it is opposed by the pressure gradient [53]. The verification case at t = 13.25 s is of type B while the remainder are of type A. During the acceleration phase, the pressure gradient dominates the flow within the train-tunnel gap and thus forms a parabolic velocity profile [53]. Once the cruising phase is entered, the velocity profile begins to flatten as the pressure gradient decreases and the friction effect at the walls begin to dominate. This leads to the profile seen for the case at $t = 13.25\,\mathrm{s}$. The profiles then progressively flatten further towards the case at $t = 23.00\,\mathrm{s}$, after which little further change was observed through the remaining period of the cruising phase.

5.3.2 VOLUME FLOW RATE AND PRESSURE GRADIENT

The normalised volume flow rate, $\dot{V}/u_* z_g$ where $\dot{V}$ is the volume flow rate, and the pressure gradient $z_g(dp/dx)$ where p is the pressure, are shown in Figure 5.4 for the five verification cases. The pressure gradient is measured between the front and back of the train.

The normalised volume flow rate shows excellent agreement between the experimental and numerical results across all cases investigated, with an average error of 6.6%. The pressure gradient shows good agreement but with a larger discrepancy towards the cases at t = 13.25s and at t = 23.00s. This is due to the numerical

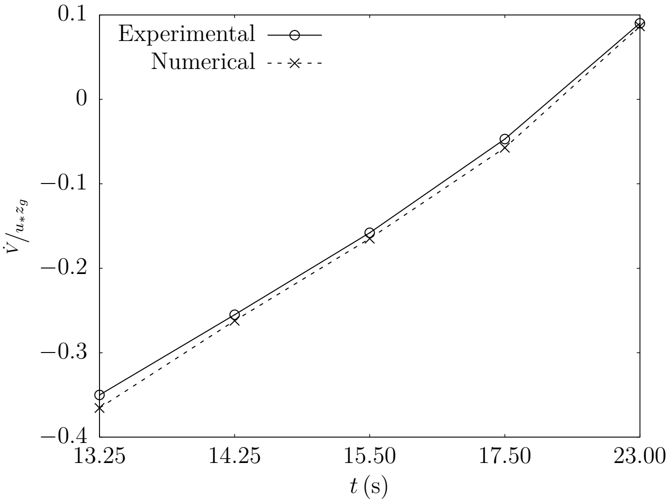

(a) Normalised volume flow rate.

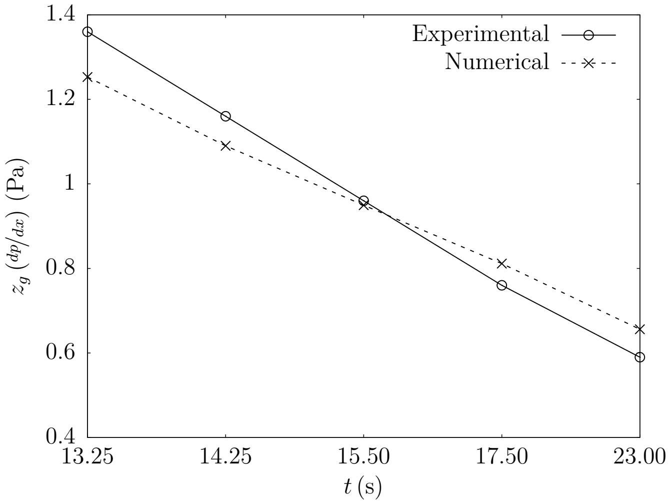

(b) Pressure gradient.

Figure 5.4: Normalised volume flow rate and pressure gradient as a function of time for the five verification cases.

configuration representing the whole train rather than just the train-tunnel gap, and as such pressure losses are generated at the front and back of the train, which are not present in the experimental configuration. The average error for the pressure gradient is 6.5%.

These results illustrate the characteristics of the flow behaviour. As the time progresses, the pressure gradient decreases as the flow profile develops from type A to type B. Simultaneously, the volume flow rate relative to the train changes from negative, as expected from a type A profile, to positive as expected from type B.

5.4 Benchmark configuration

The results from the benchmark configuration, without an attached fin or aerofoil, are used as a basis for comparison with the fin and aerofoil configurations. Figure 5.5 illustrates the air flow around the front of the train and in the train-tunnel gap.

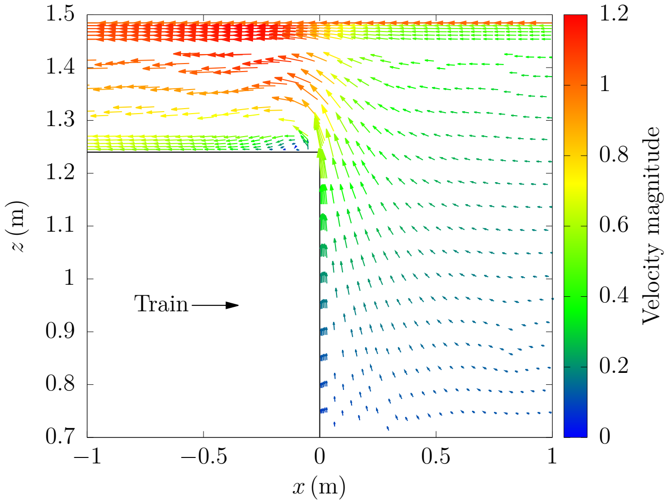

Figure 5.5: Velocity vectors around the front of the train at $t = 26.25\,\mathrm{s}$ for the benchmark configuration.

The velocity vectors shown in Figure 5.5 are drawn in the moving reference frame, i.e. relative to the train, at $t = 26.25\,\mathrm{s}$, midway through the cruising phase. The vectors are coloured by normalised velocity magnitude relative to the train, normalised by the maximum velocity of the train. As the train moves through the tunnel, air is displaced in front of the train and out of the tunnel portal ahead of the train, and a proportion is displaced through the train-tunnel gap. A small recirculation region is observed at the front of the train, in the train-tunnel gap. In the train-tunnel gap, the air velocity is greater towards the tunnel wall, as observed in the velocity profiles in Figure 5.3.

Transient results of the aerodynamic power and volume flow rate are shown in Figure 5.6.

The aerodynamic power (P) is defined as the power required by the train due to

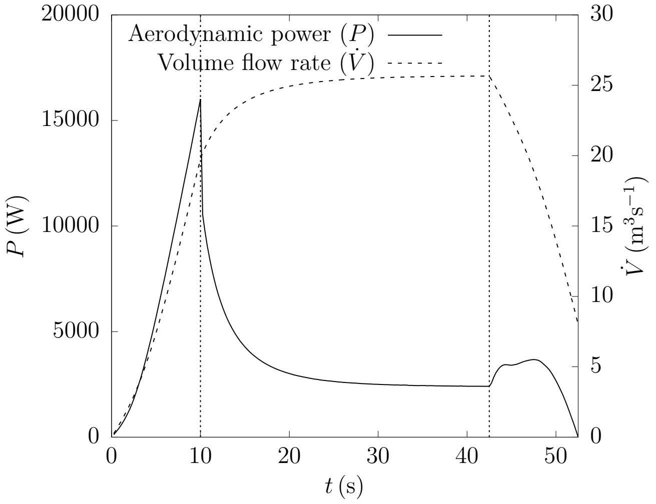

Figure 5.6: Transient aerodynamic power (P) and volume flow rate ($\dot{V}$) as a function of time.

the drag force due to the air acting upon the train, and is calculated by

$$P(t) = F_x(t) \cdot u_{tr}(t) \tag{5.1}$$

where F_x is the total force acting upon the train, and fin or aerofoil, and u_{tr} is the speed of the train. The volume flow rate ($\dot{V}$) was calculated at the tunnel exit portal, ahead of the train. The dotted vertical lines indicate the end of the acceleration phase and the end of the cruising phase.

During the acceleration phase of the train, the power increases steeply throughout the phase as does the volume flow rate. Once the train has stopped accelerating, the power drops sharply and tends towards a steady value towards the end of the cruising phase. During the cruising phase, the volume flow rate continues to rise and tends towards a steady value near the end of the phase. During deceleration, the volume flow rate decreases as the train slows while the power increases slightly, due to the body of air behind the train continuing to move at a faster speed than the train, thus creating a force acting upon the back of the train, before decreasing once the speed of this body of air matches that of the train. The aerodynamic power is represented as a positive quantity during deceleration as the drag force of the air is acting against deceleration, just as the drag force acts against acceleration and cruising in those phases of motion. The aerodynamic power during deceleration does not require the consumption of energy, but results in losses. Such losses are often in the form of heat, or if regenerative braking is used a certain proportion will be converted into electricity.

The total volume of air displaced by the train and the total aerodynamic power, referred to as the aerodynamic work (W), are used to compare the benchmark configuration with the aerofoil configuration cases. The total volume of air (V) is calculated at the tunnel exit portal, ahead of the train, using

$$V = \int_{t_1}^{t_2} \dot{V}(t)dt \tag{5.2}$$

and the aerodynamic work (W), work done by the train due to air drag, is calculated by

$$W = \int_{t_1}^{t_2} P(t)dt \tag{5.3}$$

where t_1 and t_2 are the start and finish times of the interval over which the quantity is calculated. In practice the train traction systems will be required to do work equivalent to the aerodynamic work, either in the form of providing traction or braking. The train requires energy in order to do work and so any changes in the aerodynamic work will directly influence the energy requirements of the train. Alternatively, during deceleration energy losses will occur, often in the form of heat.

The total air displacement due to the train and the aerodynamic work for the benchmark configuration are $1071.50\,\text{m}^3$ and $201971.87\,\text{kg m}^2\text{s}^{-2}$, respectively. The air displacement and aerodynamic work occur in different proportions depending on the phase of train motion. Figure 5.7 shows the proportion of the total air displacement and aerodynamic work for each phase of the train motion.

The largest proportion of air displacement and aerodynamic work occurs during the cruising phase, which is due to this being the longest phase of the motion of the train. However, the proportions of air displacement and aerodynamic work for each phase do not occur in proportion to the phase length. As a proportion of the total, 32% of the aerodynamic work occurs during acceleration and 54% during the cruising phase, while these phases account for 19% and 62% of the total time. This

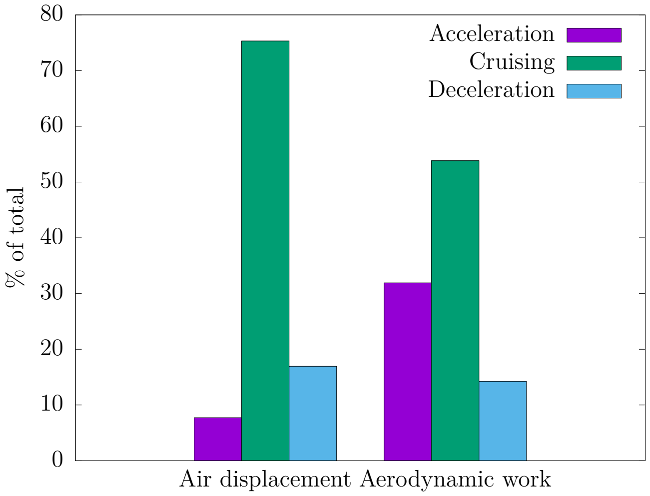

Figure 5.7: Proportion of air displacement and aerodynamic work occurring in each phase of the train motion.

indicates that a large proportion of aerodynamic work occurs during the acceleration of the train. Conversely, 7% of the air displacement occurs during the acceleration and 75% during the cruising phase, thus showing that a larger proportion of air displacement occurs during the cruising phase.

5.5 FIN CONFIGURATION

The fin configuration is consists of a simple alteration to the benchmark configuration. The fin is a regular shaped appendage on the front of the train, which extends into the train-tunnel gap on both sides of the train. A sketch of the train fin on one side of the train is shown in Figure 5.8, with characteristic dimensions. The location of the sketch within the benchmark configuration is shown in Figure 5.2.

The width of the fin, x_f, is kept constant in all cases at 0.05 m. The height of the fin, z_f, is varied so that the fin blocks between 10% and 80% of the train-tunnel gap. The results in this section are presented in terms of the proportion of the train-tunnel gap blocked, for which a gap blockage ratio is defined as

$$\beta_g = \frac{z_f}{z_g} \tag{5.4}$$

and therefore ranges between 0.1 and 0.8.

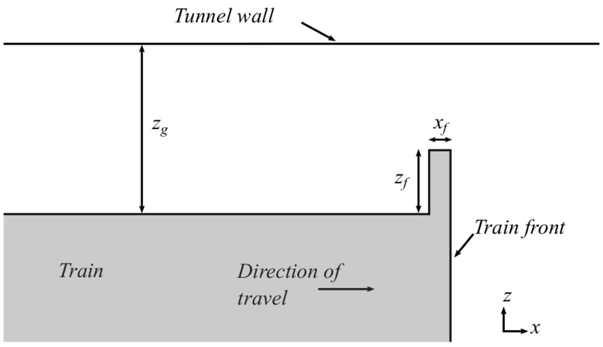

Figure 5.8: Sketch of the train fin configuration, showing characteristic dimensions.

The only similar device of which the author is aware was presented by Yoshimura et al. [147]. This consisted of a retractable fin attached to a train on the Yamanashi Maglev Test Line in Japan, the purpose of which was to act as an aerodynamic brake in the open air.

In this section the air flow patterns around the front of the train are presented and the effect of the train fin is shown. The consequential effect on the pressure and viscous forces is explained and the effect on aerodynamic work and air displacement, during the acceleration, cruising and deceleration phases and over the total time are shown.

5.5.1 Air flow patterns

The effect of the train fin is to alter the aerodynamic resistance of the train and hence the air flow around the train. In particular, the size of the fin alters the air flow and the pressure and viscous drag upon the train.

Figure 5.9 shows velocity vectors around the front of the train for $\beta_g = 0.2$ and $\beta_g = 0.4$ at $t = 26.25\,\mathrm{s}$.

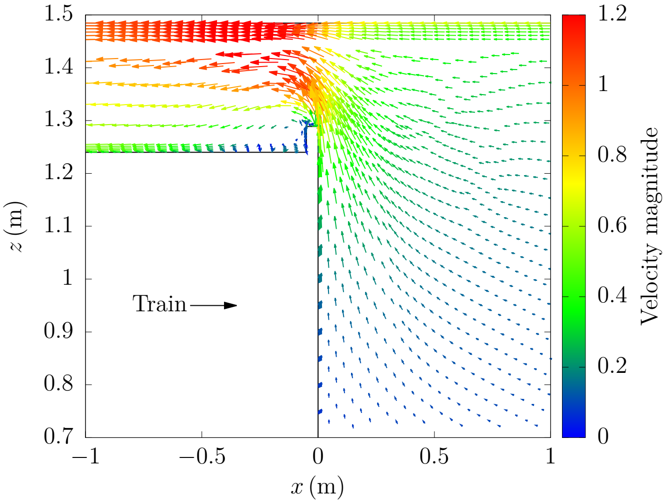

(a) $\beta_g = 0.2$.

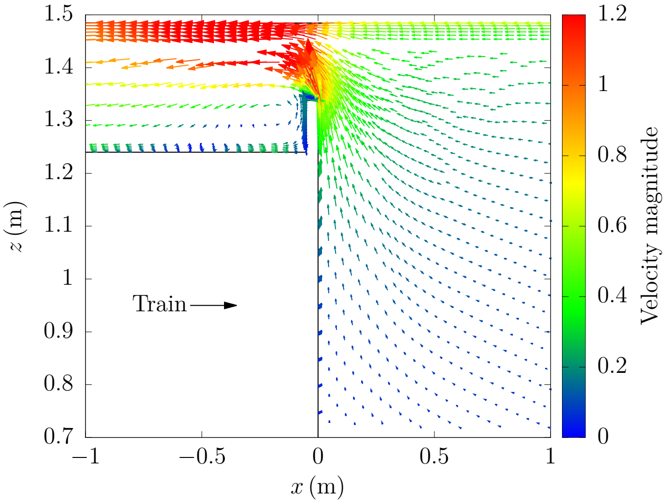

(b) $\beta_g = 0.4$.

Figure 5.9: Velocity vectors around the front of the train at $t = 26.25\,\text{s}$ for various gap blockage ratios (β_g).

For $\beta_g = 0.2$, the recirculating region at the front of the train has expanded, compared with that shown in Figure 5.5 for the benchmark configuration. For $\beta_g = 0.4$, the recirculating region increases in proportion to the increase in the fin size, and the strongest velocities in the train-tunnel gap are concentrated at the tunnel wall.

Figure 5.10 shows velocity vectors around the front of the train for $\beta_g = 0.6$ and $\beta_g = 0.8$.

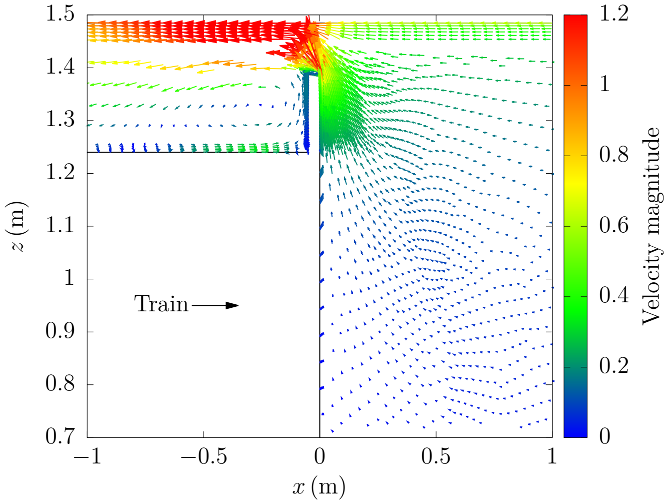

(a) $\beta_g = 0.6$.

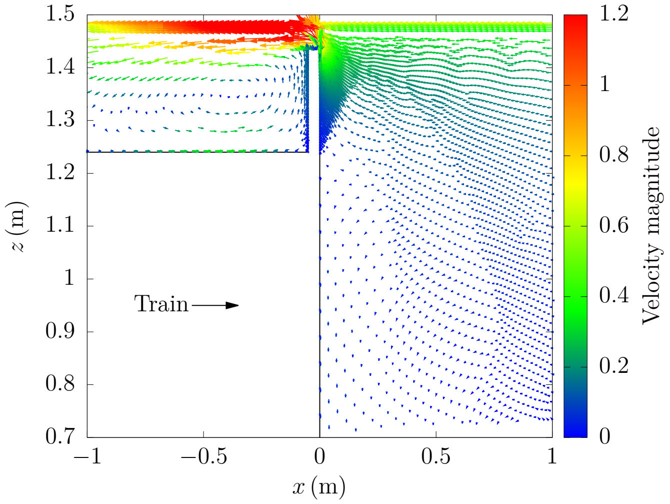

(b) $\beta_g = 0.8$.

Figure 5.10: Velocity vectors around the front of the train at $t = 26.25\,\text{s}$ for various gap blockage ratios (β_g).

As β_g approaches 0.8, the recirculating region expands to occupy most of the width of the train-tunnel gap. The air velocity through the gap at the front of the train becomes restricted to the region close to the tunnel wall, and much of the air ahead of the train is moving at a velocity close to that of the train.

5.5.2 PRESSURE AND VISCOUS FORCES

The alterations to the air flow patterns around the front of the train induced by the train fin result in changes in the air flows in front of and to the back of the train, and the pressure and viscous forces acting upon the train. In this case the pressure force acts upon the front and back of the train and the viscous force upon the sides of the train. The forces are presented in terms of the aerodynamic power done by the train calculated using either the pressure or viscous force in place of the total force upon the train in equation (5.1), and normalised by the value from the benchmark configuration. These are referred to as the normalised aerodynamic power due to the pressure force, P_P^+, and the normalised aerodynamic power due to the viscous force, P_V^+. Figure 5.11 shows P_P^+ and P_V^+ and the air flow rates at the tunnel exit portal, ahead of the train, and through the train-tunnel gap relative to the train, $\dot{V}_o^+$ and $\dot{V}_g^+$, calculated using equation (5.4), normalised by the value from the benchmark configuration, as a function of β_g. These results are shown at $t = 26.25\,\text{s}$, as is the case for the air flow patterns shown in Figures 5.9 and 5.10.

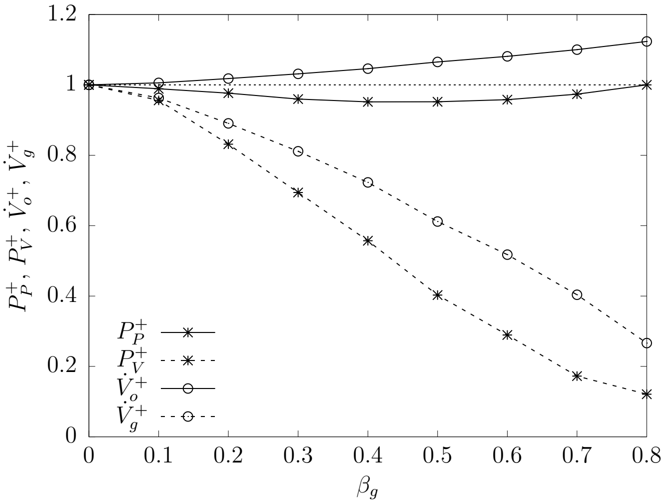

Figure 5.11: Normalised aerodynamic powers (P_P^+, P_V^+) and air flow rates ($\dot{V}_o^+$, $\dot{V}_g^+$) at $t = 26.25\,\text{s}$, as a function of the gap blockage ratio (β_g).

The air velocity through the train-tunnel gap drops significantly as the gap blockage ratio increases, to around 0.3 of the benchmark configuration value at $\beta_g = 0.8$. The reduction in air flow through the train-tunnel gap results in a reduction in the aerodynamic power due to the viscous force, which drops to about 0.15 of the benchmark configuration value. The decrease in air flow through the train-tunnel gap results in a greater proportion of displaced air moving ahead of the train and through the tunnel exit portal. The reduction in the aerodynamic power due to the viscous force has an effect on the aerodynamic power due to the pressure force. The viscous force acting upon the train side contributes to the overall pressure force acting upon the front and back of the train, which in this case reduces the pressure difference between the front and back of the train. This is known as the viscous pressure drag [135]. The aerodynamic power due to the pressure force decreases with increasing β_g, but after $\beta_g = 0.4$ increases due to the increased size of the fin counteracting the reduction in viscous pressure drag.

5.5.2.1 Aerodynamic work due to the pressure force

The aerodynamic work due to the pressure force W_P, work done by the train due to the pressure forces acting upon the train, is calculated using equations (5.1) and (5.3), with the pressure force used in place of the total force. The results in this section are presented as normalised work due to the pressure force, $W_P^+ = W_P/W_P^*$, where W_P^* is the reference aerodynamic work from the benchmark configuration.

Figure 5.12 shows the normalised work due to the pressure force for the acceleration, cruising and deceleration phases, as a function of β_g. The dotted horizontal line at $W_P^+ = 1$ indicates the value of the benchmark configuration.

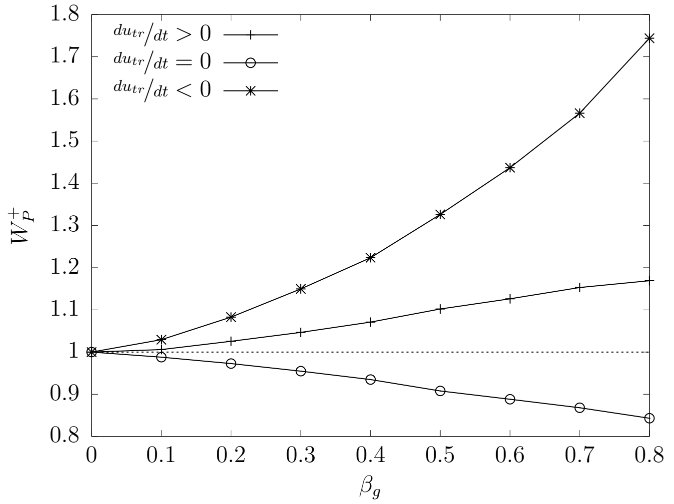

Figure 5.12: Normalised aerodynamic work due to the pressure force (W_P^+) as a function of the gap blockage ratio (β_g).

During the acceleration phase, the aerodynamic work increases with increasing β_g, to about 75% greater than the benchmark configuration value. The rapid increase is due to the inertia of the air, which the train must do work upon to overcome. During the cruising phase, the aerodynamic work decreases steadily to about 0.85 of the benchmark value. The reduction is due to the effect of the fin reducing the viscous pressure drag. The pattern observed in the aerodynamic power, due to the pressure force, and shown in Figure 5.11, is not seen here as the fin has most effectiveness in reducing the power at the start of the cruising phase. Thus, the largest fins reduce the power significantly during the initial stages, which has a significant effect upon the work. The aerodynamic work increases with increasing β_g during the deceleration phase, to about 18% greater than the benchmark configuration. This increase is due to the body of air behind the train, which is moving faster due to the fin size, acting upon the back of the train.

5.5.2.2 Aerodynamic work due to the viscous force

The aerodynamic work due to the viscous force W_V, work done by the train due to the viscous forces acting upon the train, is calculated using equations (5.1) and (5.3), with the viscous force used in place of the total force. The results in this section are presented as normalised work due to the viscous force, $W_V^+ = W_V/W_V^*$, where W_V^* is the reference aerodynamic work from the benchmark configuration.

Figure 5.13 shows the normalised work due to the viscous force for the acceleration, cruising and deceleration phases, as a function of β_g. The dotted horizontal line at $W_V^+ = 1$ indicates the value of the benchmark configuration.

During all phases, the aerodynamic work due to the viscous force is reduced as the fin size is increased. The restriction created by the fin at the front of the train reduces the air flow through the train-tunnel gap during all phases of the motion, and this results in a decrease in the aerodynamic work. The decrease in aerodynamic work during the acceleration and cruising phases follow a similar trend with increasing β_g, albeit with lower values for the cruising phase. The decrease during the deceleration phase is less significant, reducing to 0.5 of the benchmark configuration, compared with the range 0.1–0.15 for the other phases. The difference is due to the position of the fin at the front of the train, which restricts flow through the train-tunnel gap

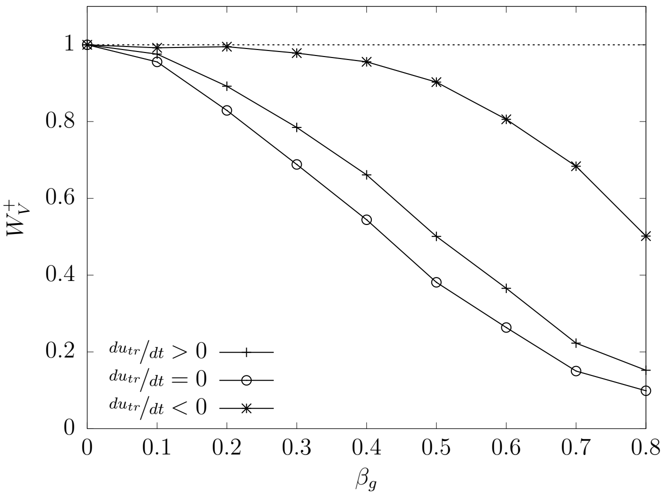

Figure 5.13: Normalised aerodynamic work due to the viscous force (W_V^+) as a function of the gap blockage ratio (β_g).

during acceleration and cruising, but during deceleration, when the air moves from the back of the train to the front, the fin has a far lower effectiveness. It may be conjectured that if an additional fin was positioned at the back of the train in the same manner, a similar reduction in aerodynamic work could be achieved during deceleration.

5.5.3 Air displacement and aerodynamic work

The displaced air volume through the tunnel exit portal and total aerodynamic work done by the train and fin are calculated using equations (5.1)–(5.3) and normalised using the value from the benchmark configuration. These are referred to as the normalised air displacement (V^+) and aerodynamic work (W^+). The air displacement and total aerodynamic work are given separately for the three phases of the train motion and the total travel time.

5.5.3.1 Acceleration phase

Figure 5.14 shows the normalised displaced air volume and aerodynamic work for the acceleration phase for various gap blockage ratios.

During the acceleration phase, the train does work to overcome the inertia of the air, which is initially in a quiescent state. For β_g up to 0.5 the aerodynamic

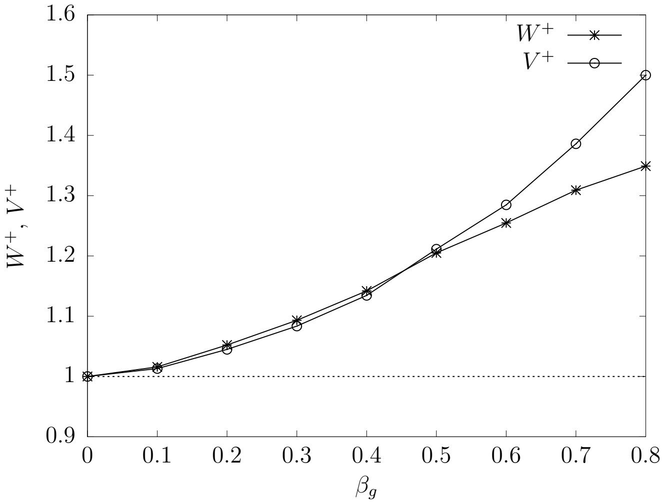

Figure 5.14: Normalised displaced air volume (V^+) and aerodynamic work (W^+) during the acceleration phase as a function of gap blockage ratio (β_g).

work and air displacement vary in a very similar manner, increasing by around 20%. Above $\beta_g = 0.5$ the increase in air displacement continues at a higher rate than the aerodynamic work, resulting in a 35% increase in aerodynamic work and a 50% increase in air displacement compared with the benchmark configuration. This is due to the larger fins blocking a greater proportion of the train-tunnel gap, resulting in a greater air flow rate ahead of the train, which simultaneously decreases the work due to the viscous force, thus mitigating the increase in the work due to the pressure force.

5.5.3.2 CRUISING PHASE

Figure 5.15 shows the normalised displaced air volume and aerodynamic work for the cruising phase for various gap blockage ratios.

The air displacement and aerodynamic work vary in an unrelated manner, during the cruising phase. The air displacement increases linearly, increasing by about 14% at $\beta_g = 0.8$, compared with the benchmark configuration. In contrast, the aerodynamic work deviates from the benchmark configuration value by less than 2% for all β_g. Between $\beta_g = 0$ and 0.4 the aerodynamic work increases by less than 0.5%, after which it decreases so that at $\beta_g = 0.8$ the aerodynamic work is about 1% less than the value for the benchmark configuration. The difference in the behaviour

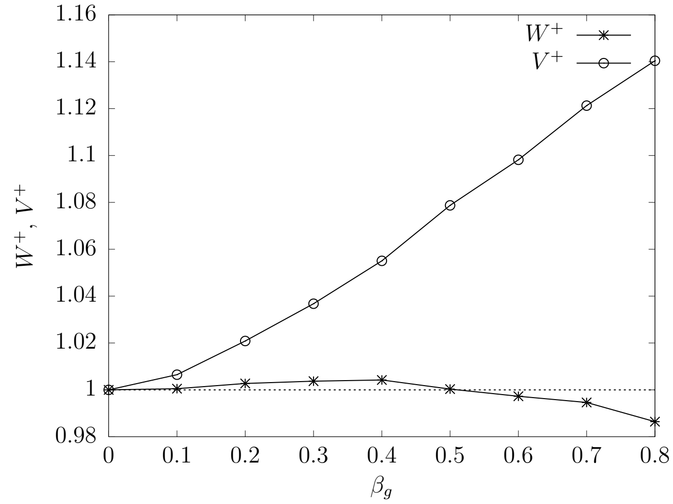

Figure 5.15: Normalised displaced air volume (V^+) and aerodynamic work (W^+) during the cruising phase as a function of gap blockage ratio (β_g).

of the aerodynamic work and air displacement is due to decreases in the work due to the pressure and viscous forces resulting from increasing the size of the fin, which simultaneously causes an increase in the air displacement due to less air passing through the train-tunnel gap.

5.5.3.3 DECELERATION PHASE

Figure 5.16 shows the normalised displaced air volume and aerodynamic work for the deceleration phase for various gap blockage ratios.

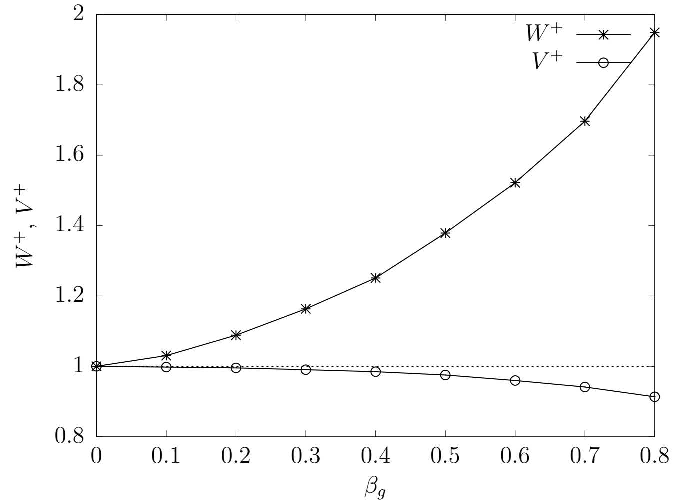

Figure 5.16: Normalised displaced air volume (V^+) and aerodynamic work (W^+) during the deceleration phase as a function of gap blockage ratio (β_g).

The aerodynamic work during the deceleration phase acts against the train, in the direction of travel. Therefore, if the aerodynamic work increases, this results in work which must be done by the train to stop to increase. The aerodynamic work shown in Figure 5.16 increases for increasing values of β_g, hence increasing the work required for braking. The larger fin size also reduces the air flow through the train-tunnel gap, and hence the overall air displacement. The increase in aerodynamic work is significant—about 95% for $\beta_g = 0.8$. This is due to the fin generating a greater flow of air during the acceleration and cruising phases, which retains momentum into the deceleration phase, and acts upon the back of the train as it slows.

5.5.3.4 Total travel time

The aerodynamic work over the total travel time is calculated using equation (5.3). During the acceleration and cruising phases, the effect of the aerodynamic work acts against the direction of train motion and work to be done by the train propulsion system. During the deceleration phase, the aerodynamic work acts in the direction of train motion, but because the train is slowing, this causes the train braking system to do work. The type of braking system must be carefully considered while calculating the contribution of aerodynamic work during the deceleration phase to the overall aerodynamic work.

Braking systems in underground railway trains are generally composed of two different types—dynamic brakes and friction brakes. Friction brakes use the friction between two surfaces to convert the train kinetic energy in order to stop the train. Dynamic brakes use the train traction motors as generators, which are driven by the rolling train, and converts the train kinetic energy into electrical energy. Dynamic braking systems also use friction brakes for the final stop. The electrical energy generated by dynamic brakes must be dissipated, and is either lost or captured for useful work. Traditionally, the electrical energy was dissipated by passing the current through resistors, which convert the electrical energy into heat—this is known as rheostatic braking. The conversion of the train kinetic energy into heat energy generates a significant heat load in the underground railway environment. In place of dissipating the electrical energy through resistors, the heat load may be reduced by either transmitting the generated electricity into the electrical supply system or by storing the electricity, for useful work—this is known as regenerative braking.

The aerodynamic work during braking can therefore be considered either as a positive contribution to the overall aerodynamic work in the case of rheostatic braking, or as a negative contribution in the case of regenerative braking. Here, it is assumed that the regenerative braking is 100% efficient. Considering the aerodynamic work to be a negative contribution in the case of regenerative braking reduces the overall aerodynamic work compared with the rheostatic braking case, as the aerodynamic work during deceleration partially offsets the aerodynamic work during acceleration and cruising phases.

Figure 5.17 shows the normalised displaced air volume and aerodynamic work, for rheostatic and regenerative braking, over the total travel time for various gap blockage ratios.

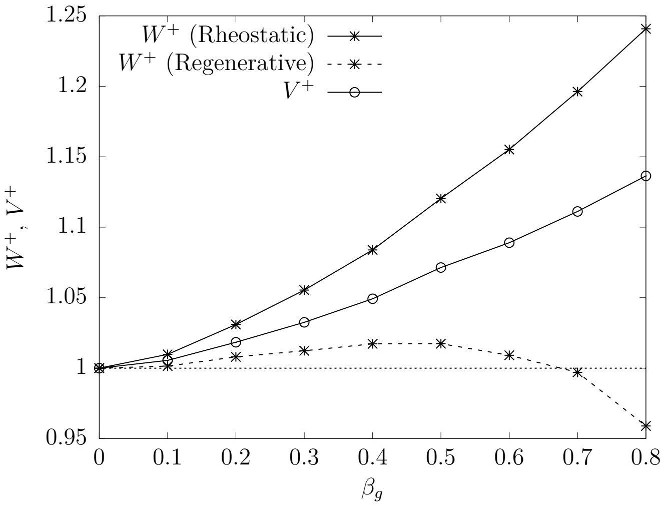

Figure 5.17: Normalised displaced air volume (V^+) and aerodynamic work (W^+), for rheostatic and regenerative braking, over the total time as function of gap blockage ratio (β_g).

Over the total time, increasing the gap blockage ratio to 0.8 increases the air displacement by about 14% compared with the benchmark configuration. If a rheostatic braking system is assumed then the aerodynamic work increases by about 25%. If regenerative braking is used then the aerodynamic work increases at a significantly lower rate, to about 2% at for a gap blockage ratio of 0.5. For higher gap blockage ratios, the aerodynamic work decreases to about 4% less than the benchmark configuration for $\beta_g = 0.8$. The effect of regenerative braking is clear, as the capturing of the train energy offsets the aerodynamic work in the acceleration and cruising phases. Therefore, significant increases in air displacement can be achieved with only a small or no increase in aerodynamic work if regenerative braking is used.

5.6 Aerofoil configuration

The aerofoil configuration consists of an aerofoil positioned in the train-tunnel gap, at the front of the train. The aim of the aerofoil is to alter the aerodynamic resistance, but to have a lower impact on the aerodynamic work of the train than the train fin. A sketch of the train fin on one side of the train is shown in Figure 5.8, with characteristic dimensions. The location of the sketch within the benchmark configuration is shown in Figure 5.2.

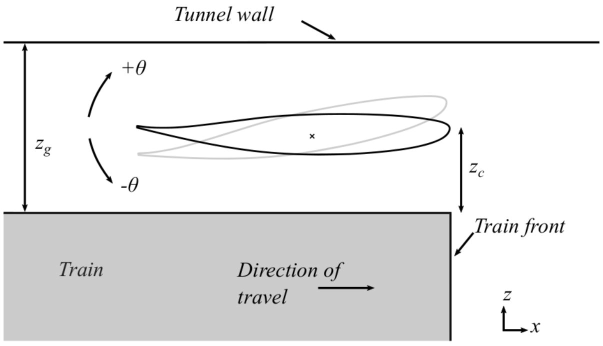

Figure 5.18: Sketch of the train aerofoil configuration, showing characteristic dimensions.

The distance from the aerofoil tip to the train side, z_c, is 0.12 m, when the aerofoil is positioned at an angle of inclination of 0°. The dimensions of the train and tunnel, as well as the transient motion of the train, remain the same as in the benchmark configuration. The aerofoil chosen is the NASA LS(1)-0413 aerofoil as it has been investigated in the context of touring cars [99] and the ground effect [150]. The aerofoil section shape is shown in Figure 5.19.

The aerofoil is inverted as shown in Figure 5.19, with the upper side adjacent to the tunnel wall and the lower surface adjacent to the train side. When the aerofoil

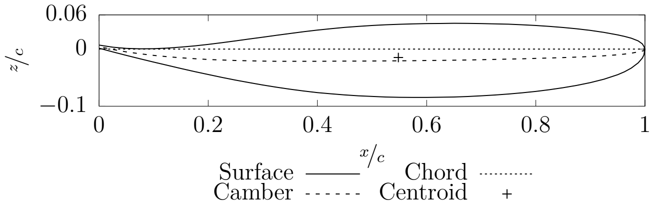

Figure 5.19: Section shape of the NASA LS(1)-0413 aerofoil.

is at an angle of inclination of 0° the leading point of the aerofoil is coincident with the front of the train and the chord line is midway between the train side and tunnel wall to ensure that the effect from either does not dominate. The chord length c is chosen as 0.40 m. In practice, an attachment would be required to fix the aerofoil to the side of the train. However, as a 2-d simulation is used in this chapter, any possible attachment is omitted.

The aerofoil configuration is tested with the aerofoil at a series of different angles of inclination, θ. The addition of the aerofoil and variation of angle of inclination varies the gap blockage ratio. Here, the gap blockage ratio is defined as

$$\beta_g = \frac{z_a}{y_g}, \tag{5.5}$$

where z_a is the width of the train-tunnel gap occupied by the aerofoil. For $\theta = 0°$ the gap blockage ratio is around 0.21 which increases to about 0.57 for $\theta = 20°$. The angles of inclination tested are shown in Table 5.1, along with the equivalent gap blockage ratios.

Table 5.1: Tested angles of inclination and equivalent gap blockage ratio for both positive and negative inclinations.

	Gap blockage ratio (β_g)	
Angle of inclination (θ)	$-\theta$	$+\theta$
0°	0.21	0.21
±2°	0.21	0.21
±6°	0.21	0.21
±10°	0.27	0.33
±16°	0.45	0.51
±20°	0.51	0.57

The aerofoil is rotated about its centroid, as shown in Figure 5.19. A positive angle of inclination indicates that the trailing edge of the aerofoil is rotated away from the train side while a negative angle indicates the converse. The gap blockage ratio for each angle of inclination are very similar whether a positive or negative inclination is used.

In this section the air flow patterns around the front of the train are presented and the effect of the train aerofoil is shown. The consequential effect on the pressure and viscous forces is explained and the effect on aerodynamic work and air displacement, during the acceleration, cruising and deceleration phases and over the total time are shown.

5.6.1 Air flow patterns

The effect of the train aerofoil is to alter the aerodynamic resistance of the train and hence the air flow around the front of the train. In particular, the angle of inclination of the aerofoil alters the proportion of air displaced ahead of and towards the back of the train, and the pattern of air flow around the front of the train. The alteration of the air flows therefore also influences the forces acting upon the train, and hence the aerodynamic work. Depending on the angle of inclination, the addition of the aerofoil may improve the aerodynamic characteristics of the train.

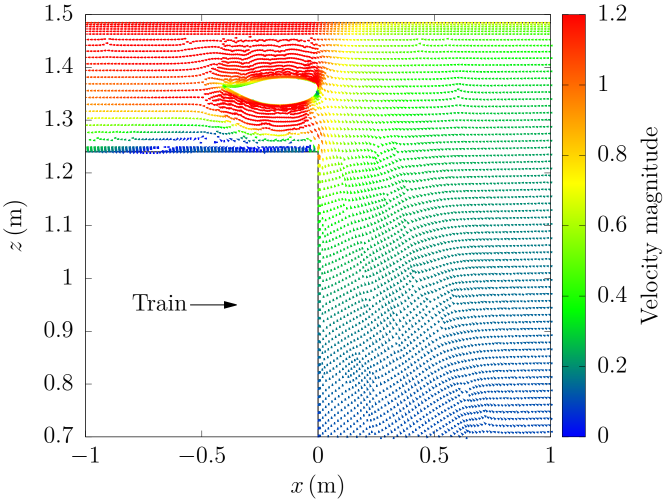

Figure 5.20: Velocity vectors around the front of the train at $t = 26.25\,\mathrm{s}$ for $\theta = 0\,°$.

Figure 5.20 shows the air flow behaviour around the front of the train for the aerofoil configuration with a $\theta = 0°$ angle of inclination.

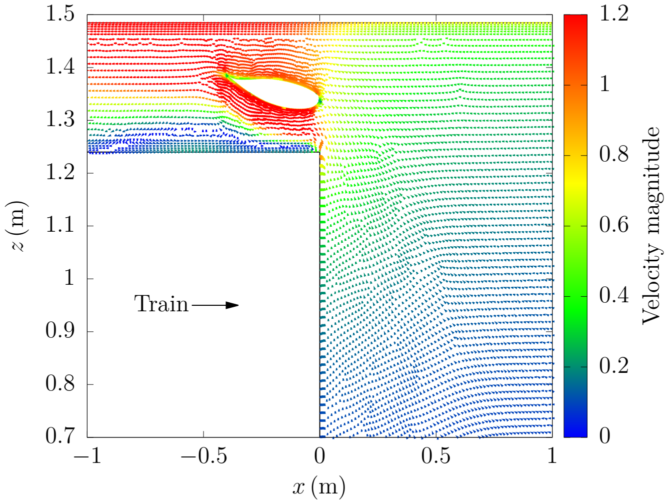

(a) $\theta = 6°$.

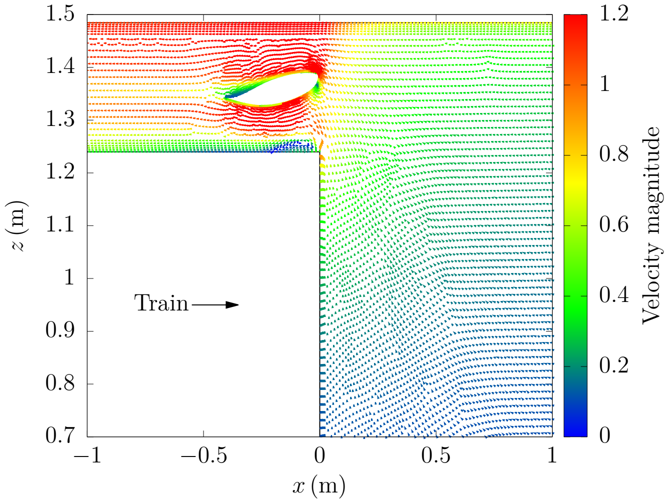

(b) $\theta = -6°$.

Figure 5.21: Velocity vectors around the front of the train at $t = 26.25\,\mathrm{s}$ for various aerofoil angles of inclination (θ).

The air flow in Figure 5.20 can be compared with that in the benchmark configuration, shown in Figure 5.5. The aerofoil has encouraged the movement of air through the train-tunnel gap, observed in the increased magnitude of the air flow. The air flow adjacent to the train side has a lower relative velocity, and the small recirculation region present at the front of the train in the benchmark configuration has elongated. The shape and angle of the aerofoil directs the strongest air flow away from the side of the train, and towards the tunnel wall. The aerofoil has had the effect of streamlining the blunt shape of the train in the benchmark configuration, allowing the air to flow around the train with greater ease.

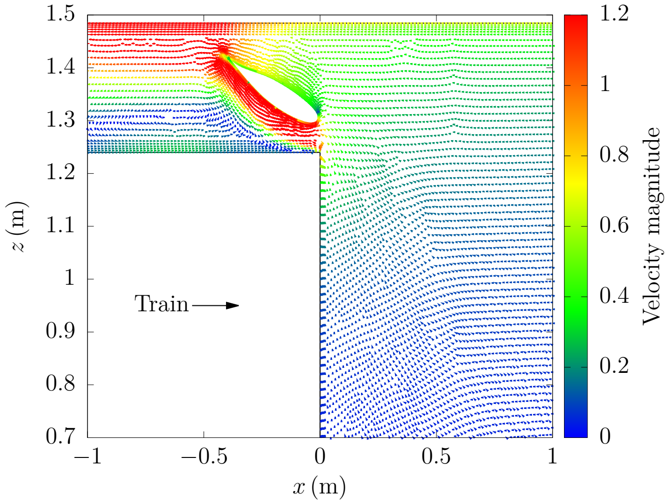

(a) $\theta = 16°$.

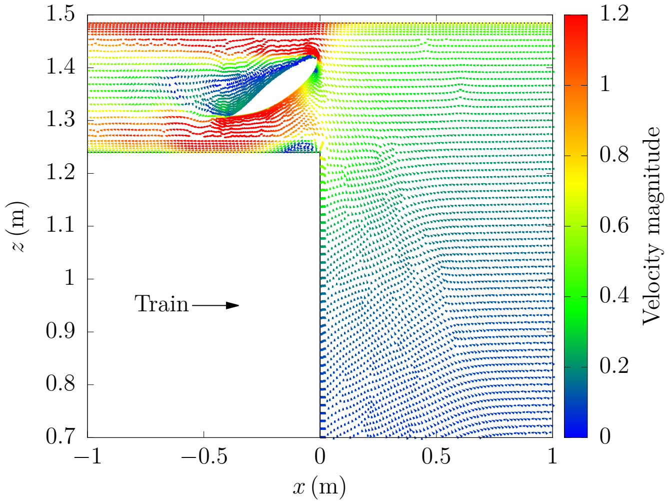

(b) $\theta = -16°$.

Figure 5.22: Velocity vectors around the front of the train at $t = 26.25\,\mathrm{s}$ for various aerofoil angles of inclination (θ).

Figure 5.21 shows the flow behaviour around the front of the train for the aerofoil configuration with $\theta = 6°$ and $\theta = -6°$ angles of inclination. For $\theta = 6°$, the positive angle of inclination directs the air flowing through the train-tunnel gap towards the tunnel wall, compared with the $\theta = 0°$ case. The result of the redirection the the air flow is to increase the size of the recirculating region, to occupy a larger width of the train-tunnel gap. For $\theta = -6°$, the negative angle of inclination directs the air flow towards the train side, thus created a small recirculating region at the very front of the train. The strongest air flows are distributed more evenly through the train-tunnel gap than in the $\theta = 6°$ case, and are generally of lower strength.

Figure 5.22 shows the flow behaviour around the front of the train for the aerofoil configuration with $\theta = 16°$ and $\theta = -16°$. For the $\theta = 16°$ case, the angle of the aerofoil directs the air flow towards the tunnel wall. There is now no recirculation region at the front of the train, but a larger region directly behind the aerofoil. In contrast, in the $\theta = 6°$ case, the negative angle of inclination causes strong air flows to be directed towards the train side and tunnel wall. In this case there is a small recirculating region at the front of the train, and a large recirculating region directly behind the aerofoil.

5.6.2 PRESSURE AND VISCOUS FORCES

The alterations to the air flow patterns around the front of the train induced by the train aerofoil results in changes in the air flows around the train, and hence the pressure and viscous forces acting upon the train. The forces are presented in terms of the normalised aerodynamic power done by the train due to the pressure force, P_P^+, and the normalised aerodynamic power due to the viscous force, P_V^+.

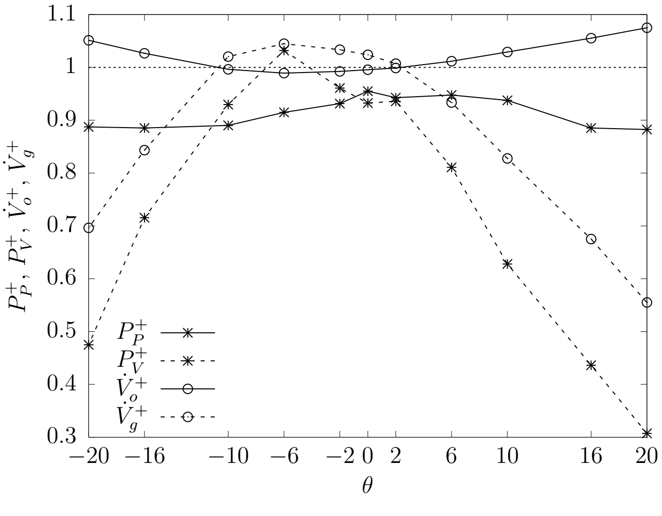

Figure 5.23: Normalised aerodynamic powers (P_P^+, P_V^+) and air flow rates ($\dot{V}_o^+$, $\dot{V}_g^+$) at $t = 26.25\,\mathrm{s}$, as a function of the aerofoil angle of inclination (θ).

Figure 5.23 shows P_P^+ and P_V^+ and the air flow rates at the tunnel exit portal, ahead of the train, and through the train-tunnel gap relative to the train, $\dot{V}_o^+$ and $\dot{V}_g^+$, as a function of the angle of inclination, θ. These results are shown at $t = 26.25\,\mathrm{s}$, the mid point of the train motion. The benchmark configuration is indicated by the horizontal dotted line.

At $\theta = 0$, the impact of the aerofoil has been to increase the air flow through the train-tunnel gap compared with the benchmark configuration, and hence to reduce the air displacement ahead of the train. The increase in air flow through the train-tunnel gap results in a decrease in the power due to the pressure force. Although the air flow through the train-tunnel gap increases, the effect of the aerofoil directing the air flow away from the side of the train reduces the power due to the viscous force. At $\theta = 6$, the air flow through the train-tunnel gap has been reduced due to the increased angle of inclination, which results in a larger air displacement ahead of the train, and a lower power due to the viscous force. The power due to the pressure force is also lower than the benchmark configuration, due to the reduction in the viscous pressure force. In contrast at $\theta = -6$, the air flow through the train-tunnel gap increases, and as a results so does the power due to the viscous force. The air displacement ahead of the train reduces due to the greater flow of air through the train-tunnel gap, which also reduces the power due to the pressure force. At $\theta = 16$ and $\theta = -16$, the aerofoil decreases the air flow through the train-tunnel gap significantly, which in turn reduces the power due the viscous force. The large angle of inclination acts to increase the air displacement ahead of the train. The power due to the pressure force does not increase significantly due to the reduction in the viscous pressure force, which results in a lower pressure difference between the front and back of the train.

5.6.2.1 Aerodynamic work due to the pressure force

Figure 5.24 shows the normalised work due to the pressure force, W_P^+, for the acceleration, cruising and deceleration phases, as a function of aerofoil angle of inclination. The dotted horizontal line at $W_P^+ = 1$ indicates the value of the benchmark configuration.

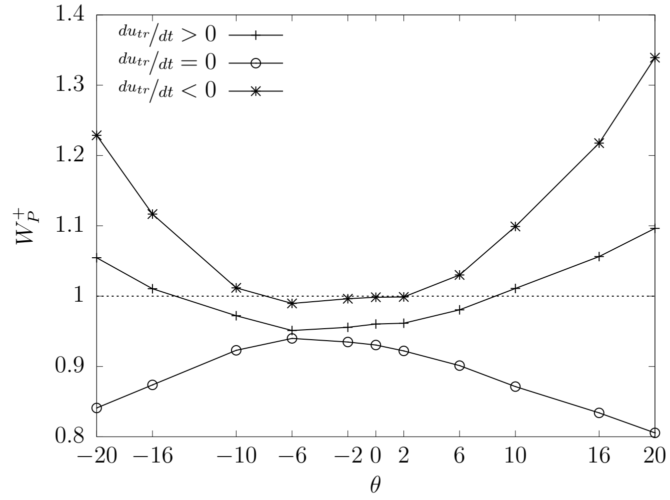

Figure 5.24: Normalised aerodynamic work due to the pressure force, W_P^+, as a function of the aerofoil angle of inclination (θ).

During the cruising phase, the aerofoil acts to reduce the value of W_P^+ for all aerofoil angles. This reduction is due to the reduction in the viscous pressure force. A maximum reduction of 19% is achieved with an aerofoil angle of 20°. The reduction is lower for the corresponding negative angle of $-20°$ due to the negative angle of inclination directing the flow of air towards the side of the train, thus resulting in a higher viscous pressure drag. During the acceleration phase, the aerofoil reduces W_P^+ for the angles $-10° \leq \theta \leq 6°$, due to either reduction in the viscous pressure force, or the aerofoil angle of inclination creating a smoother path for the air flow around the train. During the deceleration phase, the effect of the aerofoil is to generally increase the value of W_P^+. In this case, it is the effect of the body of air moving from behind the train and acting upon the back region of the train as it slows which creates the increase in the value of W_P^+. At higher angles of θ, a greater air flow is induced in the tunnel during the acceleration and cruising phases of train motion and so leads to a greater force acting upon the train during deceleration.

5.6.2.2 Aerodynamic work due to the viscous force

Figure 5.25 shows the normalised aerodynamic work due to the viscous force, W_V^+, for the acceleration, cruising and deceleration phases, as a function of the aerofoil angle. The dotted horizontal line at $W_V^+ = 1$ indicates the value of the benchmark configuration.

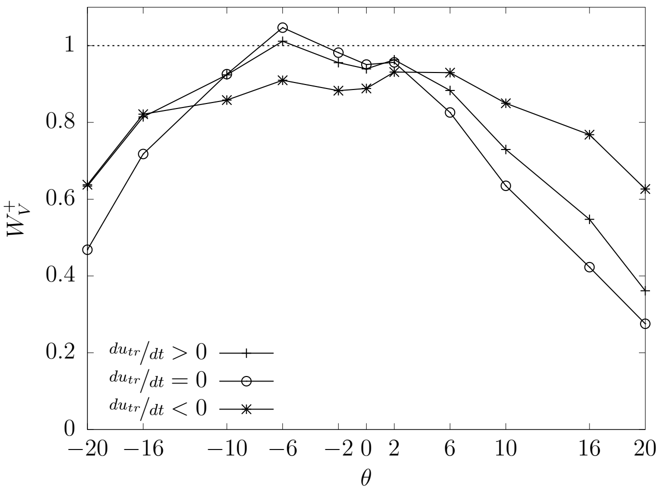

Figure 5.25: Normalised aerodynamic work due to the viscous force, W_V^+, as a function of the aerofoil angle of inclination (θ).

Generally the effect of the aerofoil is a reduction in W_V^+ for all phases of the train motion and most aerofoil angles. During the acceleration and cruising phases, this is due to the aerofoil directing the air flow away from the sides of the train and the aerofoil reducing the flow of air through the train-tunnel gap. At $\theta = -6°$, the aerofoil increases the air flow through the train-tunnel gap, thus increasing W_V^+. During deceleration, the reduction is due to the increase in air flow through the train-tunnel gap from the back to the front of the train, so the velocity is relatively closer to that of the train wall velocity for a larger proportion of this phase.

5.6.3 Air displacement and aerodynamic work

The displaced air volume and total aerodynamic work done by the train and aerofoil are calculated using equations (5.1)–(5.3) and normalised by dividing the result by the value from the benchmark configuration. These are referred to as the normalised air displacement V^+ and aerodynamic work W^+. The air displacement and total aerodynamic work are given for the total time of train travel and separately for the three phases of the train motion.

5.6.3.1 Acceleration phase

Figure 5.26 shows the normalised displaced air volume and aerodynamic work for the acceleration phase for various aerofoil angles of inclination.

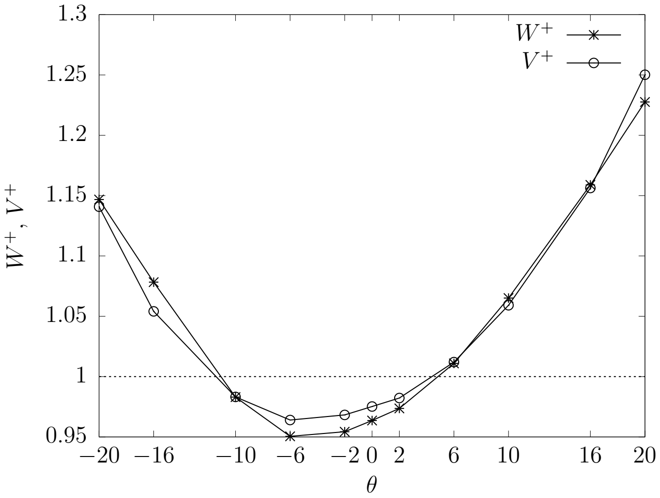

Figure 5.26: Normalised displaced air volume (V^+) and aerodynamic work (W^+) during the acceleration phase, as a function of aerofoil angle of inclination (θ).

The displaced air volume and aerodynamic work vary in a similar manner during the acceleration phase. Aerofoil angles $-10° \leq \theta \leq 2°$ decreases the aerodynamic work and air displacement while aerofoil angles $6° \leq \theta \leq 20°$, $-16°$ and $20°$ increases the aerodynamic work and air displacement. Thus no increase in air displacement is possible without also increasing the aerodynamic work.

5.6.3.2 Cruising phase

Figure 5.27 shows the normalised displaced air volume and aerodynamic work done by the train for the cruising phase for various aerofoil angles of inclination.

Except for the angles $-10° \leq \theta \leq 2°$, air displacement increases during the cruising phase of motion. A maximum increase of 9.1% is found for an aerofoil angle of 20°. For the decrease in displacement observed for $-10° \leq \theta \leq 2°$, the decrease is by a maximum of 1.4%. For all aerofoil angles, a significant reduction in work is observed with a maximum reduction of 8.9% for an angle of 20°.

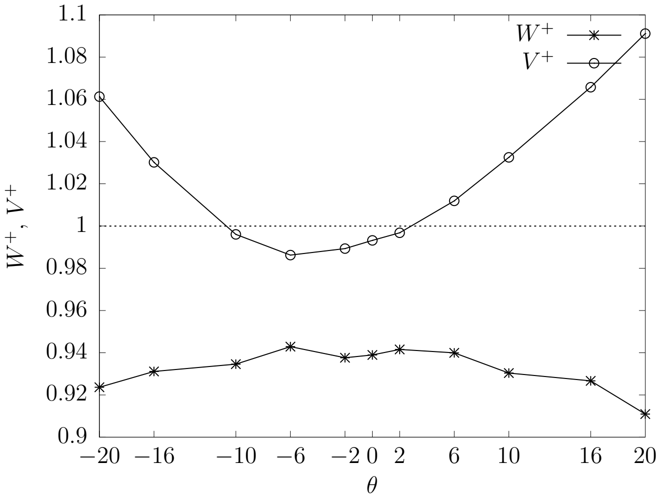

Figure 5.27: Normalised displaced air volume (V^+) and aerodynamic work (W^+) during the cruising phase, as a function of aerofoil angle of inclination (θ).

5.6.3.3 Deceleration phase

Figure 5.28 shows the normalised displaced air volume and aerodynamic work for the deceleration phase for various aerofoil angles of inclination.

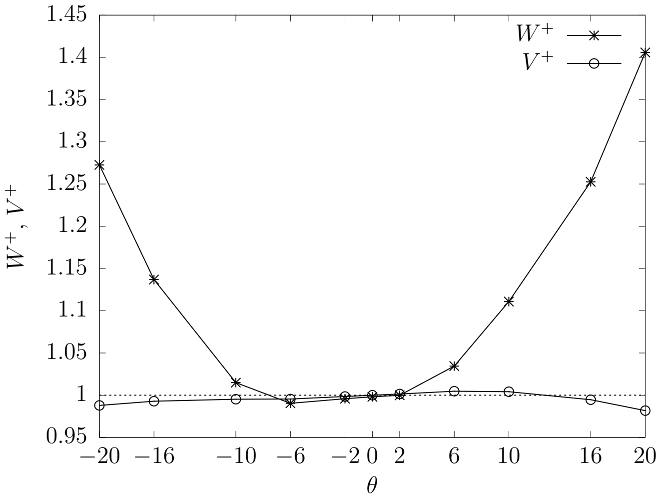

Figure 5.28: Normalised displaced air volume (V^+) and aerodynamic work (W^+) during the deceleration phase, as a function of aerofoil angle of inclination (θ).

The displaced air shows little variation with aerofoil angle, changing by less than 1% for $-16° \leq \theta \leq 16°$ and with a small increase in air displacement observed for $0 \leq \theta \leq 6°$. A maximum decreases in air displacement of 1.8% and 1.2% are found for angles of inclination of $-20°$ and $20°$, respectively. The aerodynamic work increases significantly for $10^\circ \leq \theta \leq 20^\circ$, -20° and -16° and with a maximum increase of 40%.

5.6.3.4 Total travel time

In the same way as discussed for the train fin, the aerodynamic work over the total travel time can be considered in the case where the train is equipped with either rheostatic or regenerative brakes. In the case of rheostatic brakes, the aerodynamic work is considered to be a positive contribution to the total aerodynamic work while in the case of regenerative brakes the aerodynamic work is considered to be a negative contribution as it reduces the overall work required to be done by the train.

Figure 5.29 shows the normalised displaced air volume and aerodynamic work done by the train for the total travel time for various aerofoil angles of inclination, for both the rheostatic and regenerative cases. The dotted horizontal line at $W^+, V^+ = 1$ indicates the value of the benchmark configuration.

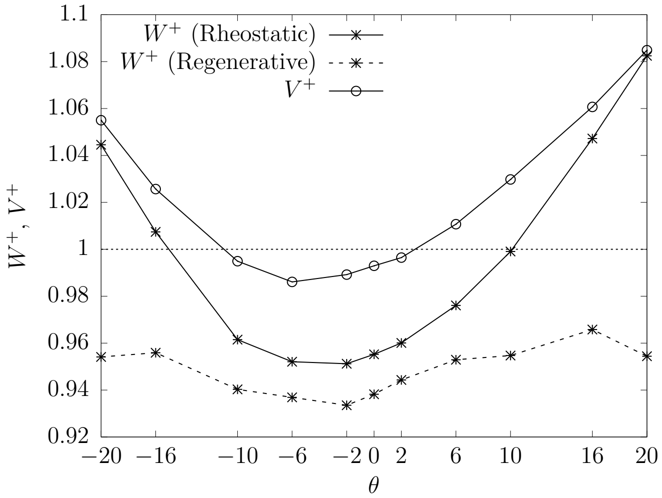

Figure 5.29: Normalised displaced air volume (V^+) and aerodynamic work (W^+), for rheostatic and regenerative braking, over the total time, as a function of aerofoil angle of inclination (θ).

The air displacement is greater for angles $6^\circ \leq \theta \leq 20^\circ$ and for -16° and -20° than the value of the benchmark configuration. In the rheostatic case the aerodynamic work is lower than the benchmark configuration for aerofoil angles $-10^\circ \leq \theta \leq 10^\circ$. Therefore an increase in displaced air is achieved without increasing the aerodynamic work for aerofoil angles of 6° and 10°. An angle of 6° increases the air displacement by 2.4% and a 10° angle by 3.0%. A maximum increase in air displacement is found to be 5.5% for an angle of 20° but this also increases the aerodynamic work by a similar proportion.

In the rheostatic case the air displacement can be increased without also increasing the aerodynamic work done by the train. This is due to the reduction in work done by the train due to the pressure and viscous forces as a consequence of the changes in the flow patterns induced by the aerofoil. The reduction of these forces counteract the increase in aerodynamic work due to the aerofoil displacing a larger air volume. In the regenerative case, the aerodynamic work is lower than the benchmark configuration for all aerofoil angles of inclination. This allows the air displacement to be increased by up to around 8% without increasing the aerodynamic work.

The increase in air displacement is lower for a negative aerofoil inclination than for the corresponding positive aerofoil angle. This is due to the angle of the aerofoil encouraging a greater air flow through the train-tunnel gap from the front of the train to the back. This reduces the volume of air displaced by the train through the tunnel exit portal.

5.6.4 Comparison of the results for the fin and aerofoil

To consider the performance of the train fin and aerofoil, the normalised displaced air volume and aerodynamic work done by the train, over the total time, are compared. Figure 5.30 shows the aerodynamic work as a function of the displaced air volume for the rheostatic braking case.

In the case of rheostatic braking, aerodynamic work and displaced air volume exhibit a positive linear relationship, where the aerodynamic work is always greater than the value from the benchmark configuration. The train aerofoil shows a weak positive linear relationship, where for $V^+ \lesssim 1.03$ a decrease in aerodynamic work is found. Therefore in the rheostatic case, only a small increase in air displacement can be achieved without increasing the aerodynamic work.

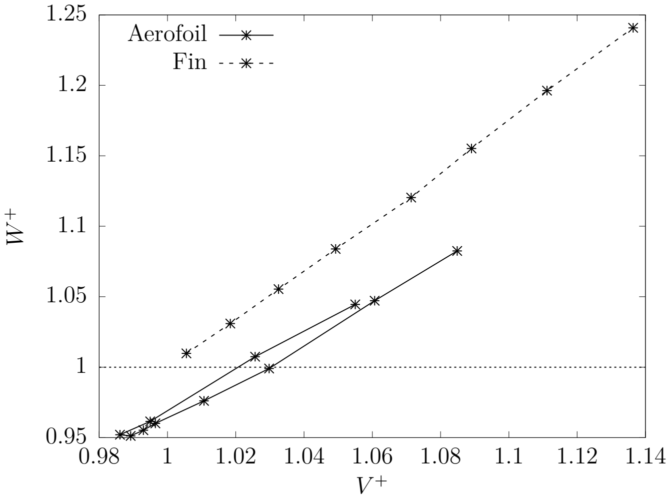

Figure 5.30: Change in normalised aerodynamic work (W^+) as a function of normalised displaced air volume (V^+), for the fin and aerofoil configurations, with rheostatic braking.

Figure 5.31 shows the aerodynamic work as a function of the displaced air volume for the regenerative braking case.

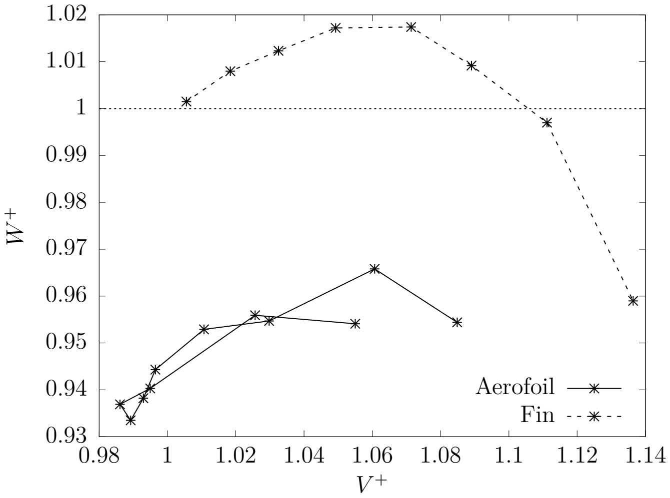

Figure 5.31: Change in normalised aerodynamic work (W^+) as a function of normalised displaced air volume (V^+), for the fin and aerofoil configurations, with regenerative braking.

In the regenerative braking case for the train fin, a large increase in air displacement can be achieved while decreasing aerodynamic work. For $V^+ \lesssim 1.1$, the aerodynamic work is found to increase, but only be a maximum of around 2%. In the case of the train aerofoil, the aerodynamic work is found to decrease for any value of V^+, and a maximum increase in air displacement of about 8% can be achieved.

5.6.5 Aerofoil combinations

The angle of the aerofoil selected results in different increases or decreases in air displacement and aerodynamic work depending on the phase of motion of the train. Therefore, instead of using a fixed angle throughout the train travel, a selection of different angles during each phase could be used to achieve a particular level of performance. In this work, 11 aerofoil angles have been tested which means that it is possible to analyse the performance of 1331 different combinations. To calculate the performance of all possible combinations, the air displacement and aerodynamic work from each phase are totalled for all the possible aerofoil combinations. This does not take account of the transition from one angle to another, for instance it does not consider the effect of a particular angle upon another phase of motion, but is considered sufficient for the purposes of illustrating the possible performance in terms of displaced air and aerodynamic work of different aerofoil combinations. Figure 5.32 shows the normalised air displacement and aerodynamic work for all 1331 possible aerofoil combinations for the rheostatic braking case, and Figure 5.33 for the regenerative braking case. The points are coloured by the aerofoil angle during the cruising phase, as it is during this phase that the majority of air is displaced and aerodynamic work is done.

5.6.5.1 Rheostatic braking

Figure 5.32 shows the normalised air displacement and aerodynamic work for all 1331 possible aerofoil combinations for the rheostatic braking case.

The dashed lines in Figure 5.32 indicate the displaced air volume and aerodynamic work from the benchmark configuration. The dashed lines create four regions, labelled A, B, C and D. Points in regions A, B, C and D represent aerofoil combinations which reduce aerodynamic work and increase air displacement, reduce aerodynamic work and reduce air displacement, increase aerodynamic work and increase air displacement and increase aerodynamic work and decrease air displacement, respectively.

Figure 5.32 shows that an aerofoil angle of 20° during the cruising phase produces

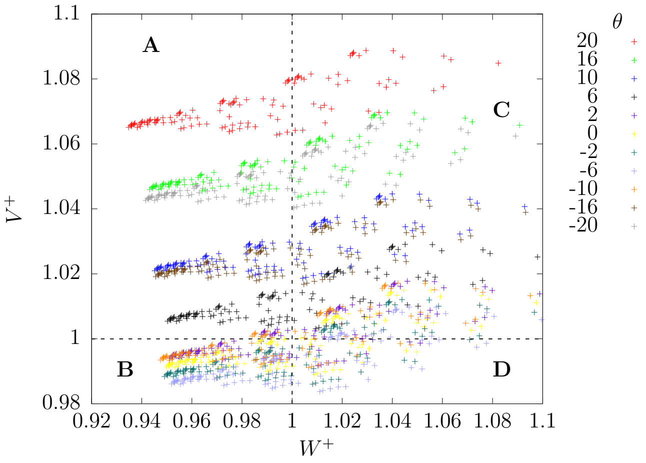

Figure 5.32: All possible aerofoil combinations, coloured by inclination angle θ during the cruising phase, in the rheostatic braking case.

an increase in displaced air of between 6% and 8% without any increase in aerodynamic work. An aerofoil angle of 16° or $-20°$ may increase the displaced air by between 5% and 6%, 10° or $-16°$ by between 2% and 3% and 6° by 1%, with the reduction in aerodynamic work ranging from negligible to about 6.5%. The other angles of inclination generally do not increase the overall air displacement. Three examples of aerofoil angle combinations are given in Table 5.2 with the resulting normalised air displacement and aerodynamic work.

Table 5.2: Selected examples of aerofoil combinations with rheostatic braking.

	Aerofoil angle (°)				
Case	Acceleration	Cruising	Deceleration	W^+	V^+
A_1	-20	20	2	0.9988	1.0798
A_2	6	20	2	0.9554	1.0698
A_3	2	20	2	0.9435	1.0698

Case A_1 is a combination of aerofoil angles which gives maximum air displacement while not increasing aerodynamic work. The displaced air is increased by about 8% with the aerodynamic work being reduced but by a negligible amount. Case A_2 gives an increase in air displacement of about 7% and a reduction in aerodynamic work of 4.5%. Case A_3 gives the same increase in air displacement as case A_2, 7%, but a greater reduction in aerodynamic work of 5.5%.

The aerodynamic work is lower for case A_3 than case A_2, however the air displacement is the same for both cases. This is due to the lower angle of inclination used during the acceleration phase for case A_3 which reduces the air displacement negligibly and aerodynamic work significantly, since a small proportion of air displacement and a large proportion of aerodynamic work occurs during acceleration, as shown in Figure 5.7.

5.6.5.2 REGENERATIVE BRAKING

Figure 5.33 shows the normalised air displacement and aerodynamic work for all 1331 possible aerofoil combinations for the regenerative braking case.

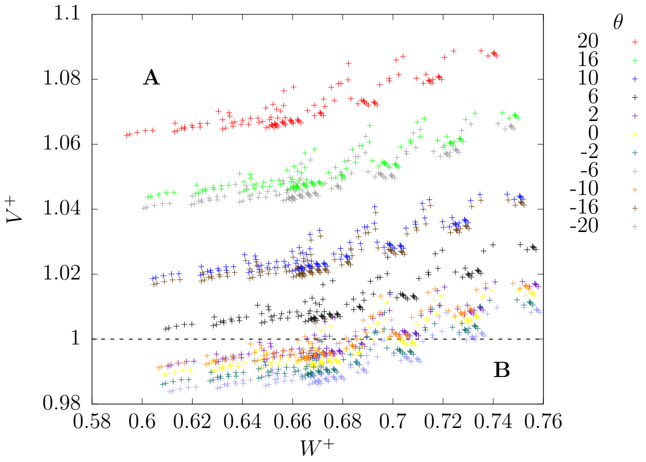

Figure 5.33: All possible aerofoil combinations, coloured by inclination angle θ during the cruising phase, in the regenerative braking case.

In this case the aerodynamic work is reduced for all aerofoil angle combinations, by a minimum of 24%. Regions A and B shown in Figure 5.33 represents aerofoil combinations which increase and decrease the air displacement, respectively. There is a maximum possible increase in the air displacement of about 9%.

5.7 SUMMARY

This chapter has evaluated the effect of having a fin or aerofoil placed on the sides of a train by investigating the train generated air displacement and aerodynamic work done by the train. A 2-d computational model was developed and verified with experimental data for a train running through a tunnel, and a series of test cases were performed with a fin of different sizes and the aerofoil at a variety of angles of inclination.

A fin was found to increase the air displacement generated by the train by up to 14%, but only with a large increase in the aerodynamic work. Through considering the use of regenerative braking, the increase in aerodynamic work can be minimised and even reduced for large fins.

In the case of rheostatic braking, an aerofoil at a fixed angle of 10° throughout the motion of the train was found to increase the air displacement by 3% while not increasing the aerodynamic work done by the train. The increase in air displacement without increasing aerodynamic work done by the train is possible due to the changes in the flow patterns induced by the aerofoil and thus the forces acting upon the train. If regenerative braking is used, it was found that any aerofoil angle would reduce the aerodynamic work.

It was shown that by using different aerofoil angles in the three phases of the train motion, further increases in air displacement are possible without increasing the aerodynamic work in the rheostatic braking case. This is possible due to the uneven distribution of the air displacement and aerodynamic work within the three phases of train motion, so a high angle may be used during cruising where air displacement is high, but during acceleration, a lower angle of inclination may be used as the air displacement within this phase is much less significant. It was found that an increase in air displacement of 8% could be achieved along with no increase in aerodynamic work. In the regenerative braking case, an increase in air displacement of 8.8% can be achieved, with a decrease in aerodynamic work of about 24%.

This chapter shows that altering the aerodynamic resistance using a fin or aerofoil can increase the ventilating air flows while not increasing aerodynamic work. While this has been illustrated in a 2-d study, further work is required to understand how this may behave in a three-dimensional situation. Consideration could also be given to the detailed design of the aerofoil and its operation as well as the possibility of using multiple aerofoils at different locations upon the train.

In practice, most trains currently in operation will have some form of aerodynamic shaping, rather than the blunt shape used in this study. Therefore, the effect of an aerofoil on a contemporary train may vary from the results shown in this study. However, as Ricco et al. [117] have shown, flow separation occurs even with fairly streamlined shapes, so the effect of an aerofoil may still be beneficial in terms of reducing aerodynamic work and increasing air flow. In particular, using an aerofoil on a streamlined train may be relatively more effective at increasing the air flow and less effective and reducing the aerodynamic work.

The addition of an aerofoil to a train will generate practical challenges. The design and operation of any attachment would be required to pose no danger to the safety of passengers or staff and to the integrity of the infrastructure. Although increasing the piston effect may improve ventilation of stations, it will be necessary to ensure that any increase in the piston effect does not increase platform air velocities to an unsafe level. Although not considered in this chapter, once the train has entered the larger volume of the station, a fin or aerofoil may improve braking performance–however this would required further work.

The performance of a aerofoil will also vary in lower blockage ratio train-tunnel configurations and where the train runs above ground. In these situations the relative proportions of the pressure and viscous drag components will change, with the viscous drag becoming more dominant [134]. However, in the case of lower blockage ratios, significant pressure will still be generated ahead of the train and regions of flow recirculation will still exist [117]. While running above ground, it may be possible to determine an aerofoil angle which is optimal for this scenario.

This chapter has shown that the air displacement generated by a moving train in a tunnel can be altered by using a device to change the aerodynamic resistance of the train. In the following chapter, the effect of increasing the air displacement on the environment of an underground railway platform will be investigated.

6

The influence of piston effect enhancement on underground platform thermal conditions

The piston effect produces significant air flows within tunnels and stations in underground railways, and provide a means of ventilation for these regions. The ventilation provided in stations has a cooling effect, through displacing the station air with air from the tunnels or outside atmosphere, if the station has a higher temperature. The braking of trains releases a significant amount of heat in stations, and raises the air temperature, which is estimated to account for about 80% of the heat load in an underground railway.

As a train approaches an underground station, air is displaced into the station and out of the various tunnels and passages which allow access by trains and passengers. On departure, the piston effect sucks air from the station, this displacement causing air to be sucked into the station from the tunnels and passages. The heat dissipated during the train arrival will be partially displaced from the station by the departing train, and any residual heat from braking will be displaced by the arrival of the train. Heat from other sources, such as passengers metabolism, lighting and other equipment, will also be displaced by the piston effect during the train arrival and departure sequence.

In Chapter 5 it was shown that by altering the shape of the train, the volume of air displaced by the train could be increased by up to between 8–14% depending on whether a train aerofoil or fin is used. In this chapter, the influence of increasing the air displacement by such a proportion on thermal conditions on an underground platform is investigated. Blackhorse Road Station on the Victoria Line, part of London Underground, is used for the investigation presented in this chapter.

First, the magnitude and behaviour of air flows within the station, generated by the piston effect, are determined. A 2-d transient isothermal numerical model is used to simulate the arrival and departure of a train in the station, and the associated induced air flows. The air flow values from the 2-d model are used as boundary conditions in a 3-d model of a single platform within the same station to investigate the detailed behaviour of the air flows. The heat load due to train braking is modelled and a benchmark condition established. The influence of air flow rate and braking heat load on platform temperatures is shown for arrival and departure conditions and the associated cooling effect is presented.

6.1 Blackhorse Road Station

The underground station considered in this study is Blackhorse Road Station, on the Victoria Line, a part of London Underground. The Victoria Line was built in the 1960s to relieve the pressure on the existing underground network, with most stations acting as interchanges with other lines. On opening, temperature conditions on the Victoria Line were adequate but have since become regularly poor within central London. In 2013 an upgrade to the line was completed which increased the frequency of trains from 27 to 33 trains per hour and passenger capacity increased by 24%. It was recognised that these measures would put pressure on the thermal conditions in the stations and tunnels and therefore a parallel programme of ventilation improvements was also completed. One of the main components of this work was to increase the capacity of the ventilation fans in the mid-tunnel shafts, located between the stations, from about 35–48 $\mathrm{m^3s^{-1}}$ to 75 $\mathrm{m^3s^{-1}}$ [23]. The line, though comparatively modern by the standards of London Underground, lacks the attributes of a line designed with good ventilation in mind; in particular the passage ways leading to platforms and entrances are small and circuitous and platform areas are cramped, as shown in Figure 6.1.

(a) The northbound platform looking south.

(b) The northbound platform looking north.

Figure 6.1: Photographs of Blackhorse Road Station, Victoria Line [33].

The Victoria Line is a two track railway in twin tunnels, with a high blockage ratio of about 0.65. At Blackhorse Road Station the line is at a depth of approximately 20 m. The station consists of two platforms each serving one of the tracks, with four passageways providing access between the two platforms. Two of the passages also pass through a concourse region from which a shaft equipped with stairs and escalators provides access to the surface. Cross passages join the two tunnels just outside the station, in the northbound and southbound directions.

Blackhorse Road Station has been the focus of previous investigations. Higton [63] and Vardy [132, 133] performed field experiments and one-dimensional (1-d) numerical simulations during the 1970s on the passage of trains through Blackhorse Road Station. This work was performed primarily for the understanding of pressure transients and for the validation and simplification of the numerical models. The station dimensions, pattern of train movements and the data that have been used for validation in the present study are based on these studies. Additional information was provided in a private communication from London Underground Limited [98].

Blackhorse Road Station was used for the investigation in this chapter for several reasons. The station is part of a underground railway system which suffers from problems with thermal conditions. Moreover, the means for improving the thermal are either difficult or expensive. Finally, there is sufficient data available for for the development and verification of a numerical model in terms of dimensions and velocity results, and temperature data from other London Underground stations.

6.2 Model configuration

The work within this chapter is formed of two parts—a transient simulation using a 2-d model to establish the magnitude and behaviour of the train induced air flows, and a steady state 3-d model to investigate the effect of the air flows on thermal conditions on a single platform.

6.2.1 Two-dimensional configuration

A 2-d model was used to simulate the isothermal transient air flows generated by the train movements. Figure 6.2 shows the 2-d modelling domain and characteristic lengths employed in this investigation.

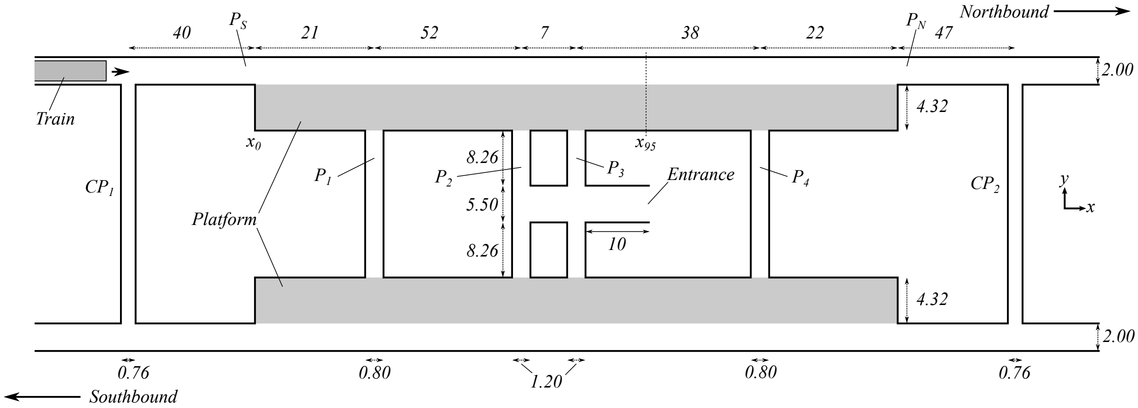

Figure 6.2: Schematic diagram of Blackhorse Road Station used for the 2-d modelling domain, dimensions in meters.

A 2-d approach was used as the 3-d behaviour of the flow is not of detailed interest in the transient case, only the bulk air flows are required. Additionally the approach also reduces the computational time required and therefore allows the modelling of the station complex and surrounding passages.

The 2-d model represents the station as a horizontal cross section. The platforms are both 140 m in length and the platform connecting passages (P_1–P_4) and the two tunnel cross passages (CP_1 and CP_2) are 22 m and 30 m long, respectively. The train was modelled travelling through the northbound platform, from south to north. The train was represented as a single unit with no gaps between the carriages, located centrally in the tunnel, with a length of 129.5 m. The dimensions of the 2-d model are chosen so that the ratios between the various opening in 3-d are preserved in the 2-d representation, so while the dimensions are not true to life the 2-d model is coterminous in meaning with the actual station. In a similar manner, the width of the train is chosen as 1.3 m so to represent the blockage ratio of the train in 3-d. The northbound tunnel extends 152 m north from cross passage CP_2 and 310 m south of CP_1, in order to allow for the movement of the train, while the southbound tunnel extends for 20 m from both cross passages. The ends of the northbound and southbound tunnels are open.

A simulation was performed which modelled the train moving through the station without stopping. This benchmark case was for the purposes of validation with data available from Vardy [132]. In this case, the train is initially positioned in the northbound tunnel, south of the station, with the back of the train 10 m from the tunnel opening. It is accelerated for 17.8 s at $1\,\mathrm{ms}^{-2}$, by which point the front of the train is 12 m south of CP_1. The train then travels at a cruising velocity of $17.8\,\mathrm{ms}^{-1}$ for 21.45 s through the station and past CP_2. The back of the train is 13 m north of CP_2 at the end of the simulation.

Two further simulations were performed to represent the arrival and stopping of a train in the station, and the departure of a train. In the case of train arrival, the train was accelerated and cruises as in the benchmark case, but after having cruised for 1.6 s until the train front is 24 m south of the southern station portal (P_S) decelerates for 17.8 s at $-1\,\mathrm{ms}^{-2}$ at which point the train is stopped midway between P_S and the northern portal (P_N). In the train departure case, the train is accelerated from the finishing position in the arrival case at 1 ms^{-2} for 17.8 s and cruises for 2.5 s at 17.8 ms^{-1}. The back of the train is 13 m north of CP_2 at the end of the simulation. Between the end of the train arrival and the start of the train departure simulations the behaviour of the flows was simulated for 30 s to represent the train waiting at the station platform. The train waiting time was estimated with data from Karekla & Tyler [80].

6.2.2 Three-dimensional configuration

The 3-d model used for steady state simulations is shown in Figure 6.3.

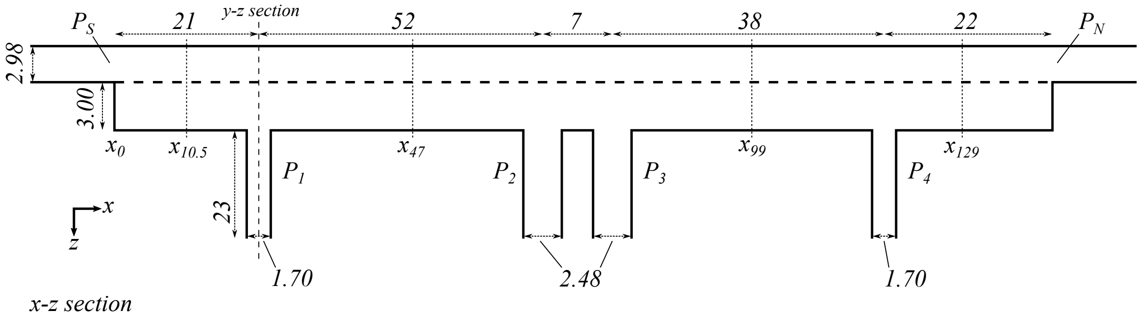

(a) Plan view.

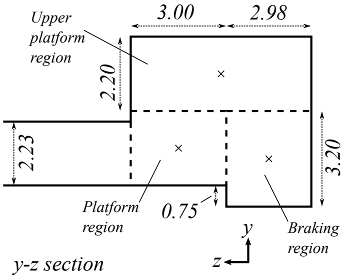

(b) Elevation view.

Figure 6.3: Schematic diagram of Blackhorse Road Station used for the 3-d modelling domain, dimensions in meters.

The 3-d modelling domain consists of the northbound platform of Blackhorse Road Station, the northern and southern sections of the northbound tunnel and the four platform entrance passages and the trench, or braking region, through which the train passes and stops adjacent to the platform. The shape of the station in y-z section is assumed to be regular rather than replicating the slightly curved shape which can be observed in Figure 6.1(a). The northern and southern sections of the northbound tunnel extend for 150 m from the southern and northern portals, respectively, and the passages leading to the platforms all extend 23 m to ensure that computational boundary effects are minimised.

6.2.3 Mesh generation

The numerical mesh representing the modelling domain in both the 2-d and 3-d models were created in Ansys ICEM CFD. The 2-d model was made up of a quad mesh and the 3-d model of a hexahedral mesh.

The 2-d case required special treatment to allow the simulation of a moving train, in a manner similar to that shown in Chapter 5. This mesh was made up of several regions; a near field region around the train, two far field regions to the front and back of the train, two boundary regions extending along the length of the near and far field regions, and regions containing the remainder of the model. The near field region was formed of a high density mesh to capture the details of the flow around the train in this region. The boundary layers were resolved by using inflation layers at the walls throughout all the regions of the mesh. The need for boundary regions allowed the train movement to be simulated while also permitting the mesh regions containing the platforms and passages to be included.

The numerical modelling of the air flow for the 2-d and 3-d models was performed using the commercial CFD software package Ansys Fluent [10]. The train movement in the 2-d simulation was modelled using the dynamic meshing method to alter the mesh in each time step. The movement of the train is achieved using the dynamic layer option to add layers of cells to the far field region to the back of the train and to remove layers of cells from the far field region at the front, as the near field region containing the train is moved at the prescribed velocity, which is defined by a user defined function (UDF). This is similar to the approach used by Huang et al. [69], albeit in 2-d. The use of dynamic layering is possible in the far field as these regions are formed of quad cell meshes [11].

6.2.4 Numerical conditions

For the steady and unsteady, incompressible fluid flow in an underground railway, the Reynolds-averaged Navier Stokes equations are solved using Ansys Fluent. The k-ϵ RNG turbulence model is used in the transient simulations as it has been successfully used previously for the investigation of train induced air flows where it was found to perform well [143, 70]. The Reynolds stress model is used to model the turbulence in the steady state simulations for improved modelling of the secondary flows present in a noncircular expansion [148]. Near wall modelling used the standard wall function, a wall function approach, to reduce the computational time in the transient calculations. The first cell height on the walls are chosen during mesh generation so that the non-dimensional y^* value is maintained in the recommended range of $30 \leq y^* \leq 300$.

In the transient simulations for tunnel openings and the station entrance, an outlet boundary condition of 0 Pa was applied given relative to an operating pressure set as atmospheric pressure. This choice allows for variations in the dynamic pressure at the openings while the static pressure is fixed, such as when the train approaches an opening of the tunnel. A similar approach was used by Khayrullina et al. [84].

In the steady state simulations, the boundary conditions for P_N and P_S and the P_1–P_4 are specified mass flow rates. The values for each boundary are taken from the results from the transient simulation.

The governing equations are solved by Ansys Fluent using the finite volume method on an unstructured mesh. In the 2-d transient simulations the SIMPLE pressure-velocity coupling method was adopted to solve the governing equations, the discretisation of the convection terms is carried out using the second-order upwind interpolation scheme and the second-order scheme to treat the pressure interpolation. The transient time step was set as 0.005 s, determined by a time step independence study. In the 3-d simulations, the coupled method was adopted to solve the governing equations.

The residual equations were monitored and the convergence criteria set as 1×10^{-5}. The convergence criteria of 1×10^{-5} ensured that the changes in monitored flow quantities between iterations exhibited only small changes, while maintaining computational efficiency. A smaller convergence criteria showed minimal changes in flow quantities. Additionally, the flow variables were monitored at various points within the domain as was the train drag in the transient case to ensure convergence. Mass conservation within the computational domain was also monitored to ensure conservation at every time step.

The initial conditions for the transient simulations of a train passing through the station and a train arriving are a quiescent velocity field. For the simulation of a departing train the initial conditions were taken as the flow field 30 s after the train had stopped.

6.2.5 Steady state conditions

The steady state, thermal, 3-d model of Blackhorse Road Station uses the results from the transient model to define the air flow conditions at the boundaries while the heat load due to train braking and the boundary thermal conditions are defined using data from literature.

6.2.5.1 Boundary air flows

As the train arrives at the northbound platform, the air flows within the station are determined by the air being pushed by the train through the south portal of the station. On train departure the station air flows are determined by the air sucked out of the station through the north portal. Therefore, if the piston effect is increased then it is these air flows which will be influenced.

The boundary air flows were defined by finding the maximum air flow through the south portal during train arrival and the north portal during train departure. To investigate the influence of different air flow rates a range of air flows were tested, greater, the same and less than the maximum value. The air flows through the openings are specified so that the air flow ratios between different openings are constant for all the air flow rates considered, i.e. increasing the air flow into the station does not change the proportion of air flowing out through a particular opening.

6.2.5.2 BOUNDARY TEMPERATURES

For the purposes of model verification, the temperatures at the boundary openings are set at 19 °C, 24 °C and 28 °C. The temperatures applied at the boundaries are considered to be tunnel air temperatures, which will generally be higher than the ambient conditions. According to data from Mortada et al. [103], the tunnel temperature equivalent ambient values are 4.4 °C, 15.3 °C and 24.1 °C. The results presented in this chapter are produced using the 24 °C boundary condition.

The thermal condition at the wall boundaries are set at a fixed temperature. As the walls in many deep underground tunnels have heated up over a period of decades, as well as the soil surrounding the tunnels, the temperatures of the walls are not significantly different to that of the air. Moreover, the wall temperature has a long lag period compared with ambient conditions. For the purposes of the steady state study a wall temperature 1 °C lower than the opening boundary temperature was selected. This value and phenomena has been observed through field measurement in the Budapest Metro by Ordódy [107] and a similar value was suggested by Botelle et al. [23] in the context of the London Underground.

6.2.5.3 PLATFORM HEAT LOAD

The heat load in an underground station is dominated by the effect of train braking. As the train approaches a platform, the braking dissipates heat into the air in the approach tunnel and then into the platform air once the train has stopped at the platform. On departure, heat on the platform will be sucked out by the train, but hot air from the approach tunnel will also be sucked into the platform. Moreover, hot air on adjacent platforms may also be sucked in.

According to Tabarra & Guan [123] the braking of a London Underground train represents the dissipation of 50 MJ of energy. To dissipate this energy rheostatic braking, used in most underground railways, uses the traction motors as generators, and the electrical energy generated during braking is dissipated through resistor grids. In newer rolling stock regenerative braking is used, where a portion of the generated electrical energy is returned to the supply network for use. The use of regenerative braking saves on traction power costs and reduces the temperature of tunnels and stations.

The resistor grids typically have temperatures, where regenerative braking is in place, between 200–280 °C in tunnels and can reach a peak of 370 °C [123]. Without regenerative braking higher temperatures would be expected. In the initial period of braking, a rise in the temperature of the resistor grids of 80 °C is typically observed, and can be as high as 105 °C. The amount of braking energy dissipated as heat depends on the temperature of the resistor grids prior to braking. If the train spends long periods in tunnels or when journeys between stations are short, the resistor grids have less ability to cool. Short dwell periods in stations, in order to increase operating capacity, and short turn around periods at terminal stations increase the initial temperature of the resistor grids at the start of the next journey, particularly if the terminal station is underground. The Transit Development Corporation [127] estimates that after 5 station stops 70% of braking energy is transferred to the air as heat and 91% after 10 stops. Tabarra & Guan [123] estimate that 1 MW of heat is released into the station box in peak rush hour.

Within the 3-d numerical model of the platform, the volume is separated into three parts—the platform, upper platform and braking regions which have volumes of 1029 m^2, 1841 m^2 and 1330 m^2, respectively. The extent of heat dissipation on the platform will alter the thermal intensity. If heat is dissipated throughout the whole platform at a rate of maximum rate of 1 MW then the thermal intensity will be about 238 Wm^{-3}. However, if the heat dissipates only in the air within the braking region then the thermal intensity would be about 751 Wm^{-3} while if heat dissipates in both the braking and platform regions this would give a thermal intensity of about 423 Wm^{-3}.

While the reasoning given here is simplistic in terms of heat dissipation being constrained to a particular region of the platform, the analysis give a range of values which are representative of the heat dissipated in an underground platform. If the thermal intensity for heat dissipation only in the braking region is neglected as an unlikely scenario, the maximum and minimum thermal intensities due to the arrival of a train are taken to be 423 $\mathrm{Wm^{-3}}$ and 178 $\mathrm{Wm^{-3}}$, respectively.

As the departing train will remove heat from the platform, but may also suck in heat from elsewhere, additional uncertainty exists relating to the heat load during train arrival. To account for this a heat load is tested lower than the calculated maximum thermal intensity.

As the magnitude of the thermal load is uncertain, a range of values were tested. Head loads of 100 $\mathrm{Wm^{-3}}$, 200 $\mathrm{Wm^{-3}}$ and 300 $\mathrm{Wm^{-3}}$ were selected based broadly on the calculated maximum and minimum thermal intensities and the uncertainty of arrival heat load. Heat loads where applied in the computational model as heat loads in the braking region.

The heat loads used here are a conservative estimate– for perspective passengers each have a metabolic rate of 207 W per person [73, 32, 13]. However, the purpose of this chapter is to investigate the influence of enhancing the piston effect on underground platform thermal conditions. Therefore testing a range of heat loads allows the impact of the piston effect to be compared in a variety of conditions, and is considered sufficient for the comparative nature of this investigation.

6.3 Station air flow behaviour

The transient air flow behaviour generated by a train moving through Blackhorse Road Station are presented to illustrate the contrasting nature of the air flows when the train is arriving or departing from the station. The representation of air flows within the station is important in order to correctly consider the effect on thermal conditions within the 3-d steady state model.

6.3.1 Verification

For the purposes of verification of the numerical results from the transient simulation of a train passing through the station without stopping are compared to the numerical results from Vardy [132]. The results presented in Vardy [132] were generated using a 1-d model of Blackhorse Road Station and surrounding tunnels which were validated with pressure data recorded in the station and tunnels. In this work the velocity data from this model are used for the purposes of validation. The velocity results from Vardy [132] are given as the average platform velocity upstream of the entrance passage, given as P_3 in this chapter as shown in Figure 6.2. These results are compared with the average velocity ($\bar{u}$) 95 m north of the P_S, just north of P_3, shown as x_{95} in Figure 6.2. The average platform velocity ($\bar{u}$) from the numerical simulation and numerical data from Vardy [132] are shown in Figure 6.4.

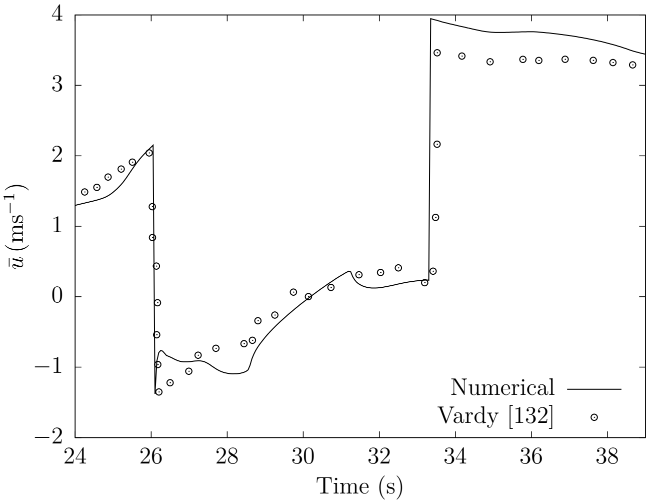

Figure 6.4: Average u velocity ($\bar{u}$) at $x = 95$ m, from the numerical simulation and Vardy [132].

The trend of the air velocity initially increases positively as the train approaches x_{95}, as the train puhses the air ahead of it. The air velocity decreases suddenly to become negative as the train front passes, due to the air flowing around the train. The air velocity then gradually decreases further until increasing after the front of the train passes P_4 through which much of the air passing down the side of the train passes, thus reducing the air velocity. The drop in velocity at 31 s is caused by the train front passing CP_2, so that much of the air passing down the side of the train passes through CP_2. As the back of the train passes x_{95}, the air velocity suddenly increases as the train sucks the air from the back of the train, after which follows a slow decrease in air velocity as the train moves on, and decreases further once the back of the train passes CP_2.

The disagreement between the current numerical results and the predictions of

Vardy [132] are due to different modelling approximations. Vardy [132] used a 1-d approach and assumed that the four passages could be grouped into two, but with the same total cross sectional area and therefore the detailed behaviour created by the four passages are not represented. In general the trends of the present results and those of Vardy [132] agree well.

6.3.2 ARRIVAL AIR FLOWS

Figure 6.5 shows the transient air flow ($\dot{V}$) during train arrival. The results are shown in terms of the air flow through the northbound platform north and south portals (P_N and P_S) and passages (P_1–P_4), which are equivalent to the opening boundaries in 3-d configuration.

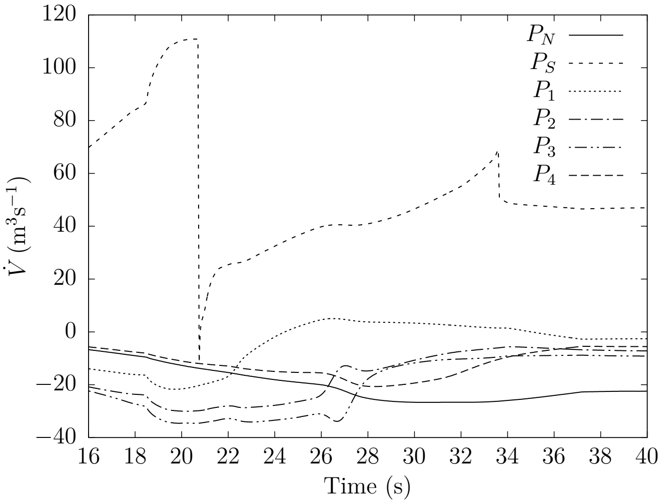

Figure 6.5: Transient air flows during the train arrival.

As the train approaches the station, air is forced into the station through P_S, and increases steadily. The largest proportion of air leaves the station through the central passages (P_2 and P_3), while the air flow is considerably lower through P_4 and P_N. As the front of the train enters the station at about 21 s the air flow through P_S drops suddenly, followed by a moderate increase until the back of the train enters the station when the air flow again drops and decreases slowly until the train stops. As the front of the train passes the central passages (P_2 and P_3), the air flow through these passages decreases and the air flow through P_4 and P_N increases, as the air flow which reaches the north end of the platform is no longer effected due to flow into the central passages.

6.3.3 Departure air flows

Figure 6.6 shows the transient air flow ($\dot{V}$) during train departure.

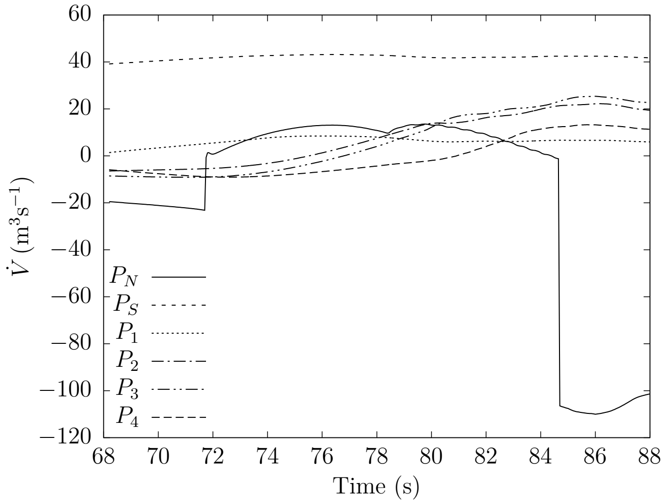

Figure 6.6: Transient air flows during the train departure.

As the train accelerates, air is forced out of the station through P_N, P_2, P_3 and P_4. The majority of air is sucked into the station through P_S and a small volume through P_1. Once the front of the train passes through P_N, the air flow through the portal drops suddenly and the air flow through the central passages declines as the train enters the northbound tunnel. As the train moves further into the tunnel, and the back of the train passes each passage, air is sucked into the station through each of the passages in sequence. As the back of the train passes through P_N, the air flow out of the station through the portal increases suddenly.

6.3.4 Boundary air flows

During train arrival, air is forced into the platform through P_S and during departures air is sucked from the platform through P_N. Figure 6.7 shows in detail the piston effect on the air flows during train arrival and departure through P_S and P_N, defined as $\dot{V}_a$ and $\dot{V}_d$, respectively.

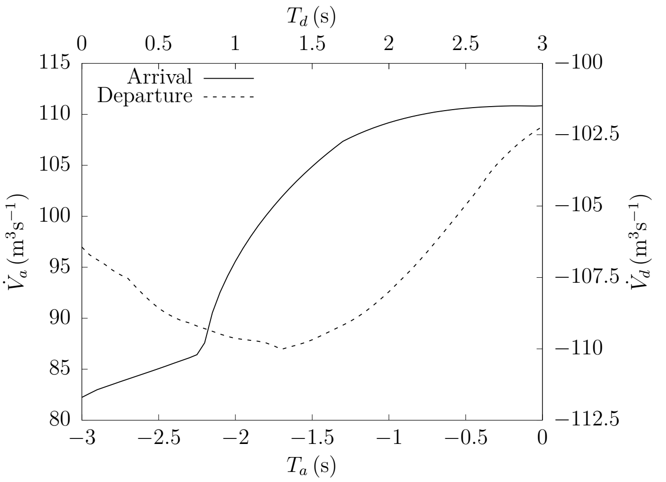

Figure 6.7: Piston effect air flows during train arrival and departure.

These results are presented as a function of T_a and T_d, respectively. T_a is the time before the front of the train passes P_S, the arrival time, and T_d is the train after the back of the train passes P_N, the departure time. Figure 6.7 shows that the maximum air flow into or out of the platform during the train arrival and departure is about $110\,\mathrm{m^3s^{-1}}$.

Table 6.1 shows the air flows during train arrival and departure, through the portal and passages, at the maximum air flow rate. The values are given as a proportion of the maximum air flow rate through P_S and P_N for arrival and departure, respectively.

Table 6.1: Maximum boundary air flows during the train arrival and departure, as a proportion of the maximum air flow rate.

	P_S	P_N	P_1	P_2	P_3	P_4
Arrival	1.00	-0.12	-0.20	-0.28	-0.32	-0.09
Departure	0.39	-1.00	0.06	0.20	0.23	0.12

The values in Table 6.1 correspond to the boundaries in the 3-d platform configuration. An air flow rate of $100\,\mathrm{m^3s^{-1}}$ during train arrival and departure is used in the 3-d configuration as a benchmark condition, and the air flows through the boundaries determined using the values in Table 6.1. To investigate the effect of different air flow rates on platform conditions, air flows of $105\,\mathrm{m^3s^{-1}}$, $110\,\mathrm{m^3s^{-1}}$, $115\,\mathrm{m^3s^{-1}}$ and $120\,\mathrm{m^3s^{-1}}$ were also tested.

If a naïve approach had been used, in which the air flow rate was defined only at a single boundary rather than at every boundary, the complex nature of the train induced air flows would not be represented within the platform and the effect on the thermal conditions would be absent.

6.4 Platform benchmark conditions

Platform benchmark conditions were established using an air flow rate of 100 $\mathrm{m^3s^{-1}}$ during train arrival and departure with a braking heat load of 300 $\mathrm{Wm^{-3}}$ and opening boundary temperature of 24 °C within the 3-d model. The benchmark conditions are presented in terms of air flow and temperature patterns.

6.4.1 Verification and validation

For the purpose of verification, results from the 3-d model were compared with measurements presented by Mortada et al. [103], taken in the Central Line in London. The Central Line has similar characteristics to the Victoria Line, being a deep level, high blockage ratio underground railway in London.

The numerical results are for an air flow rate of 100 $\mathrm{m^3s^{-1}}$ during train arrival and departure with a braking heat load of 300 $\mathrm{Wm^{-3}}$ and opening boundary temperatures of 19 °C, 24 °C and 28 °C. The results presented in Figure 6.8 show the average platform temperature as a function of ambient temperature. The numerical results are shown as a arrival-departure average for comparison with Mortada et al. [103], which is an average of the temperature during train arrival and departure.

The arrival-departure average temperature agrees well with the results from Mortada et al. [103]. For higher ambient temperatures, there is an increased variance in the temperature for arrival and departure conditions from the average.

The mesh size for both the transient and steady state simulations was validated by carrying out a mesh independence study using the h-method, through the progressive refinement of the mesh [30]. The mesh was refined until the posterior error for the u air velocity and temperature at points in the domains was below 0.5%.

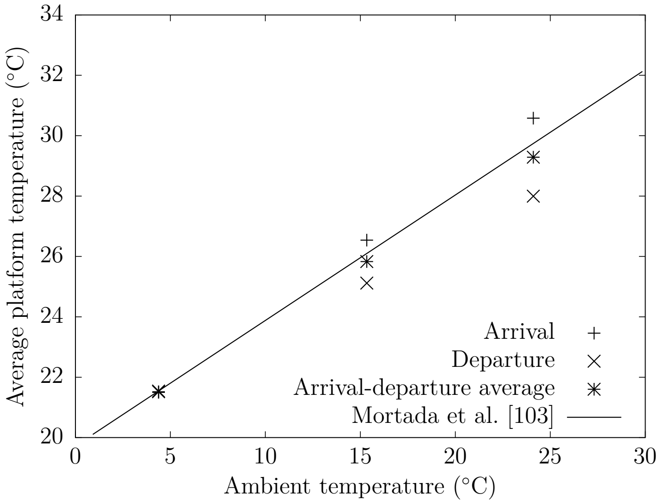

Figure 6.8: Average platform temperature, from numerical calculation and field measurements as a function of ambient temperature.

6.4.2 AIR FLOW PATTERNS

Figure 6.9 shows colour maps of u air velocity in the y–z plane for train arrival benchmark conditions. The colour maps are shown at $x = 47\,\mathrm{m}$ and $x = 99\,\mathrm{m}$, as shown in Figure 6.3.

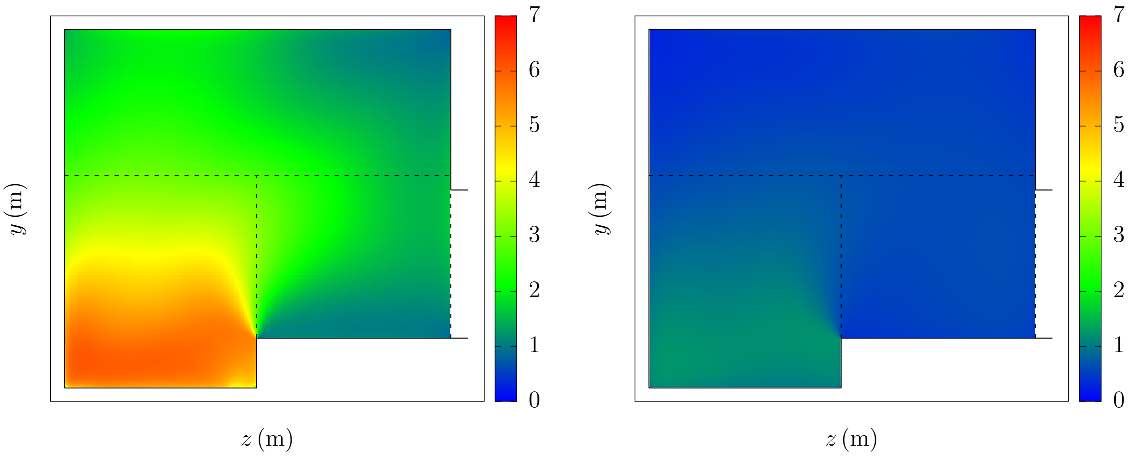

(a) $x = 47\,\mathrm{m}$.

(b) $x = 99\,\mathrm{m}$.

Figure 6.9: Colour maps of u air velocity (ms^{-1}) in the y–z plane for train arrival benchmark conditions.

At $x = 47\,\mathrm{m}$ the air flow through P_S has a significant impact on the air velocity. The air velocity within the braking region is strong, as the flow through P_S is constricted due braking region being in a trench compared to the platform region. Therefore, the air velocity in the platform and upper platform regions are considerably lower than in the braking region.

At $x = 99\,\mathrm{m}$, the air velocities are considerably weaker than at $x = 47\,\mathrm{m}$. This is due to the reduced influence of the piston effect through P_S, caused by air flow passing through the platform passages, thus reducing the effect at the north end of the platform.

Figure 6.10 shows colour maps of u air velocity in the y–z plane for train arrival benchmark conditions. The colour maps are shown at $x = 47\,\mathrm{m}$ and $x = 99\,\mathrm{m}$.

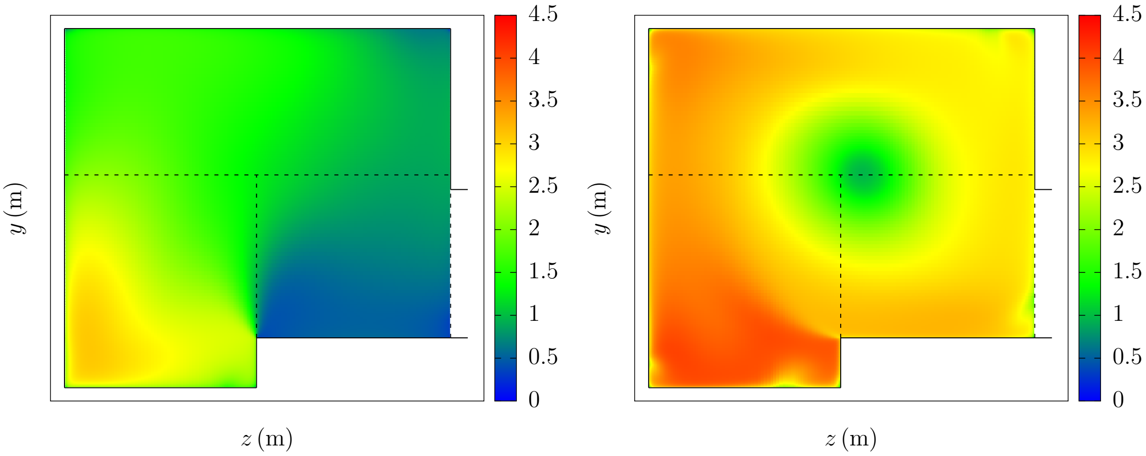

(a) $x = 47\,\mathrm{m}$.

(b) $x = 99\,\mathrm{m}$.

Figure 6.10: Colour maps of u air velocity (ms^{-1}) in the y–z plane for train departure benchmark conditions.

For departure benchmark conditions, the piston effect has the largest influence on the air velocity at $x = 99\,\mathrm{m}$, as the air is being sucked from the platform through P_N. The trench effect of the braking region constricts the highest air velocities to the braking region, but not as significantly as for the arrival conditions.

At $x = 47\,\mathrm{m}$, the air velocities are lower than at $x = 99\,\mathrm{m}$, but the difference is not as significant as for the arrival conditions. Similarly, the braking region trench constricts the highest velocities to the braking region.

The difference in air velocity patterns is due to the suction effect present with departure conditions, which encourages the flow of air through the passages and P_S. This creates a move even distribution of air velocities and results in the influence of the piston effect is felt at the extreme ends of the platform.

Figure 6.11 shows longitudinal u air velocity for train arrival and departure benchmark conditions, in the centre of the platform and braking regions, as shown in Figure 6.3.

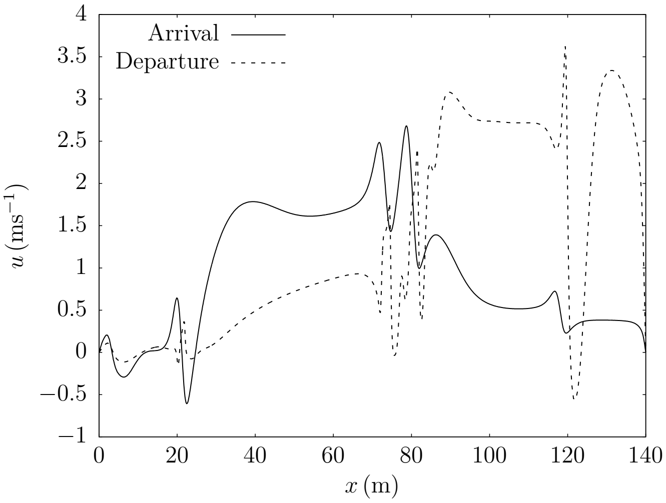

(a) Platform region.

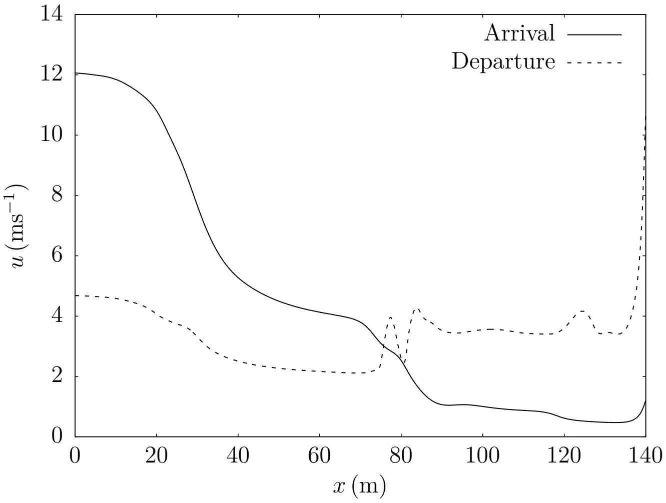

(b) Braking region.

Figure 6.11: Longitudinal u air velocity for train arrival and departure benchmark conditions.

In the platform region the velocity is higher for arrival than departure conditions south of the central passages. North of the central passage, the pattern is reversed. The central passages essentially reduce the impact of the piston effect at the extreme end of the tunnel from either P_S or P_N for arrival and departure conditions respectively.

In the braking region with arrival conditions there are velocities close to P_S which decrease significantly towards the extreme end of the platform, again being influenced by the central passages. For departure conditions the effect is less significant, with the velocity along the platform showing a more consistent pattern.

6.4.3 Temperature patterns

The patterns of air flow have a direct effect on the temperatures within the platform, due to the effect of braking heat load. The pattern of air flow effect the displacement of heat from the platform and therefore the temperatures.

Figure 6.12 shows colour maps of air temperature (°C) in the y–z plane for train arrival benchmark conditions. The colour maps are shown at $x = 47\,\mathrm{m}$ and $x = 99\,\mathrm{m}$ as shown in Figure 6.3.

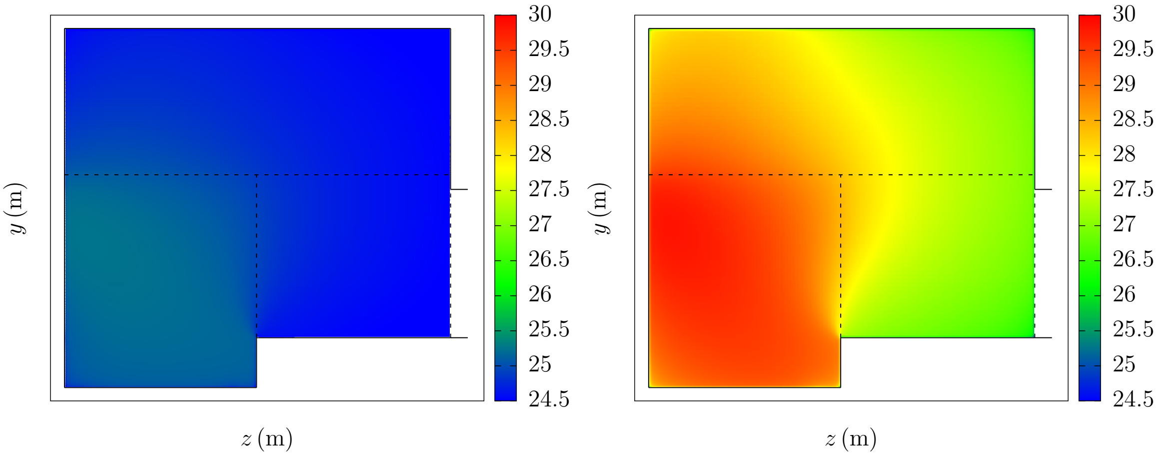

(a) $x = 47\,\mathrm{m}$.

(b) $x = 99\,\mathrm{m}$.

Figure 6.12: Colour maps of temperature (°C) in the y–z plane for train arrival benchmark conditions.

The strong velocities observed at $x = 47\,\mathrm{m}$ for arrival conditions mean that much of the braking heat is displaced and the air temperatures do not exceed the tunnel temperatures to a significant extent. However, at $x = 99\,\mathrm{m}$ the weak velocities mean that the heat from braking is not displaced effectively and the air temperatures reach upwards of 30 °C. The high temperature conditions at $x = 99\,\mathrm{m}$ are also compounded by the displacement of heat from the region south of the central passages, into the region north of the central passages.

Figure 6.13 shows colour maps of air temperature (°C) in the y–z plane for train departure benchmark conditions. The colour maps are shown at $x = 47\,\mathrm{m}$ and $x = 99\,\mathrm{m}$.

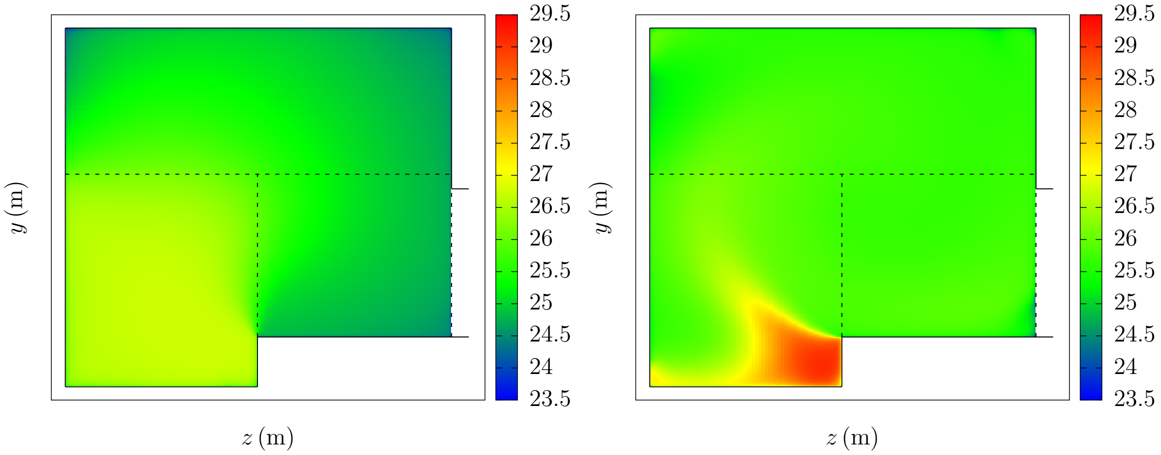

(a) $x = 47\,\mathrm{m}$.

(b) $x = 99\,\mathrm{m}$.

Figure 6.13: Colour maps of temperature (°C) in the y–z plane for the train departure benchmark conditions.

The more consistent pattern of air flow throughout the platform for departure conditions results in a more uniform pattern of air temperatures than for arrival conditions. In particular, at $x = 99\,\mathrm{m}$ the high temperatures observed for arrival conditions have been largely eliminated due to the suction of air through P_N.

Figure 6.14 shows the longitudinal air temperature for train arrival and departure benchmark conditions, in the centre of the platform and braking regions as shown in Figure 6.3.

In the platform region it can be seen that south of the central passages the air temperatures do not exceed that of the tunnel by a significant extent. The lower velocity south of the central passages has resulted in a small increase in air temperature for departure compared with arrival conditions. In the region north of the central passages, the lower air flow for arrival conditions raises the air temperature significantly compared with departure conditions. In the braking region, a similar pattern is observed, where south of the central passages the lower air flows for arrival conditions raises the air temperature compared with arrival conditions, and north of the central passages the lower air flow for arrival conditions raises temperatures, in this situation up to around 40 °C.

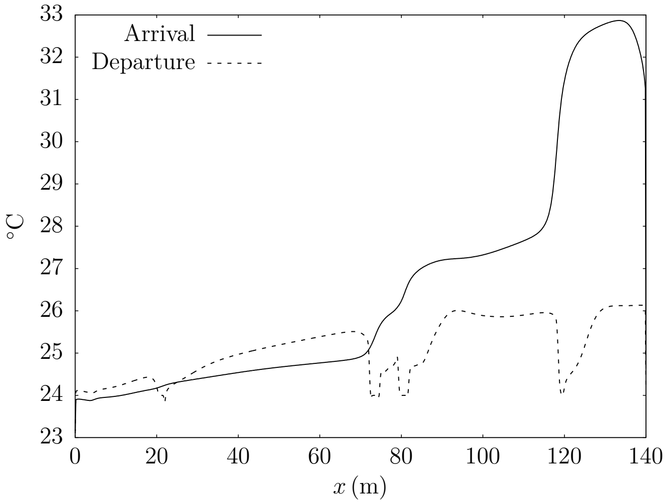

(a) Platform region.

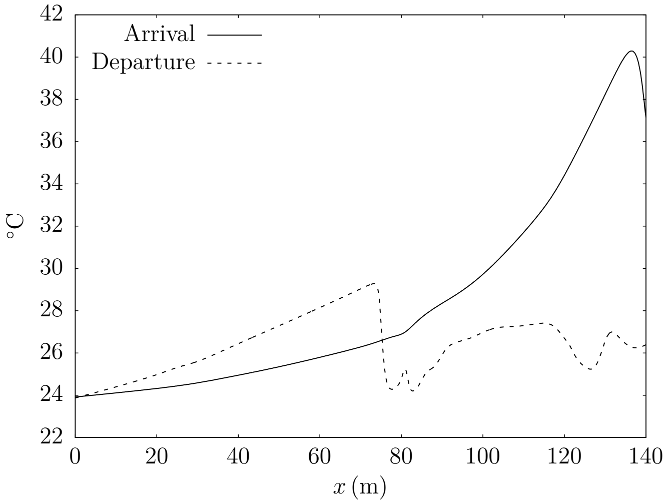

(b) Braking region.

Figure 6.14: Longitudinal air temperature for train arrival and departure benchmark conditions.

It is clear that the departure conditions are more effective at displacing heat from the platform, and thus reducing platform air temperatures, than arrival conditions. Although the arrival conditions exhibit strong velocities in the region south of the central passages, when these are reduced with departure conditions, the increase in temperature is not significant. The major difference between the two conditions is that the stronger air flow in the region north of the central passages displaces heat more effectively for departure conditions, hence removing it from the platform and reducing air temperatures significantly. Moreover, the strong air flows observed in the region south of the central passages with arrival conditions, merely displace heat into the extreme end of the platform, from which there is no means of displacement, and which then increase air temperatures significantly.

The differences in temperature between the two ends of the platform are significant, and has been observed elsewhere [151]. This is particularly the case for arrival conditions which is due to there being weak air flows north of the cross passages. In practice temperatures would not be as high as observed here, as the departing train would displace much of this heat as observed for the departure conditions. This is a result of the separate treatment of arrival and departure conditions. However, the purpose in this section was to highlight the different effect of arrival and departure conditions in displacing heat from stations.

6.5 Influence of piston effect enhancement

The influence of enhancing the piston effect—meaning to increase in this context—is shown in terms of the impact on platform air velocities and temperatures. Additionally, the cooling effect is also shown and compared with other approaches.

6.5.1 Platform air velocities

Platform air velocities are shown at $x = 47\,\mathrm{m}$ and $x = 99\,\mathrm{m}$ in the centre of the y–z plane, in platform (P) and braking (B) regions. Platform velocities are shown in Figure 6.15, where the position is denoted by a subscript and the region by a superscript, for arrival and departure conditions as a function of piston effect air flow rate.

For arrival conditions, shown in Figure 6.15(a), the velocity in the braking region at $x = 47\,\mathrm{m}$ is significantly higher than at other points, and is enhanced by higher air flow rates. The velocity in the platform region at $x = 47\,\mathrm{m}$ is significantly lower, than in the braking region. At $x = 99\,\mathrm{m}$ the velocity is weak, even with an enhanced piston effect.

For departure conditions, shown in Figure 6.15(b), although the maximum velocity is not as high as for arrival conditions, the velocity at most points is generally higher. In departure conditions the velocity at three points is higher than $2\,\mathrm{ms}^{-1}$ while in arrival conditions the velocity at three points is lower than 2 ms^{-1}.

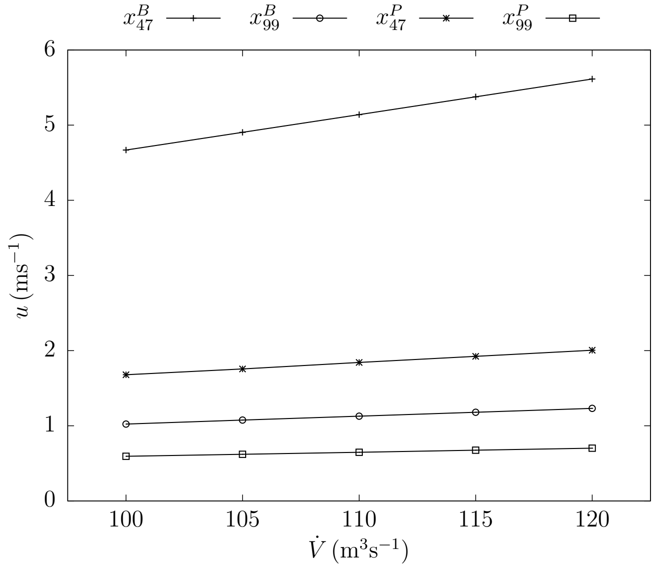

(a) Arrival conditions.

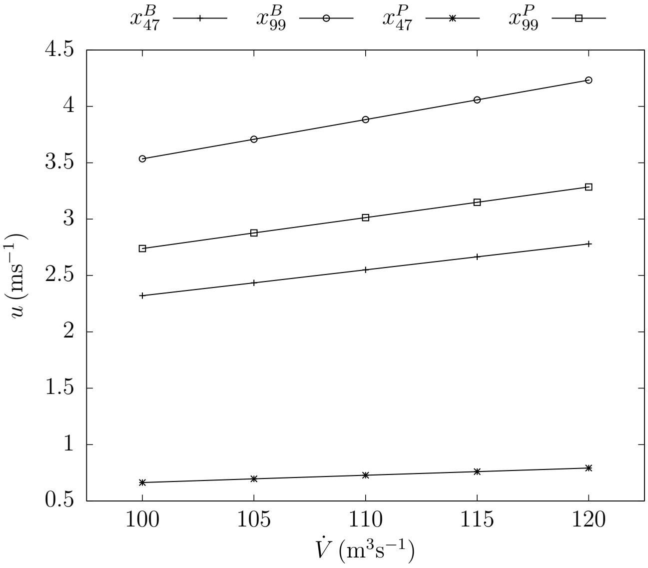

(b) Departure conditions.

Figure 6.15: Platform air velocities for arrival and departure conditions as a function of piston effect air flow.

6.5.2 PLATFORM AIR TEMPERATURES

The influence of increasing the piston effect increases the air velocities on the platform, which has an associated influence on platform temperatures. For a fixed tunnel air temperature of 24 °C air temperatures are shown for 300 Wm^{-3}, 200 Wm^{-3} and

100 Wm^{-3} braking heat loads, for arrival and departure conditions, as a function of piston effect air flow rate. Temperatures are shown at $x = 47\,\mathrm{m}$ and $x = 99\,\mathrm{m}$ in the centre of the $y - z$ plane in the braking and platform regions, and as an average temperature in the platform region (P_{ave}).

6.5.2.1 300 Wm^{-3} HEAT LOAD

Figure 6.16 shows platform air temperatures for arrival conditions for a 300 Wm^{-3} braking heat load.

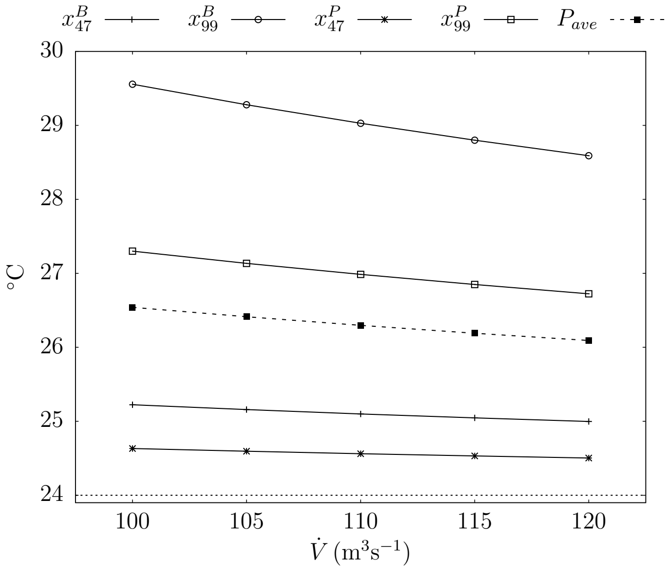

Figure 6.16: Platform air temperatures for arrival conditions as a function of piston effect air flow for a 300 Wm^{-3} heat load.

For arrival conditions, the points at the extreme end of the platform, far from P_S, have the highest air temperatures. In the region south of the central passages, the air temperature does not exceed the tunnel temperature by any more than 1.5 °C. Increasing the air flow rate by 10 m^{3}s^{-1}, from 110 m^{3}s^{-1} to 120 m^{3}s^{-1}, reduces the highest air temperature, at x_{99}^B, by 0.44 °C and the lowest air temperature, at x_{47}^P, by 0.06 °C. The average platform air temperature is reduced by 0.20 °C.

For departure conditions, shown in Figure 6.17, the points in the braking region have the highest air temperatures. The increased flow of air in the region north of the central passages has reduced the air temperatures in this region significantly. Points in the platform region are between 1.00–2.00 °C higher than tunnel air temperatures.

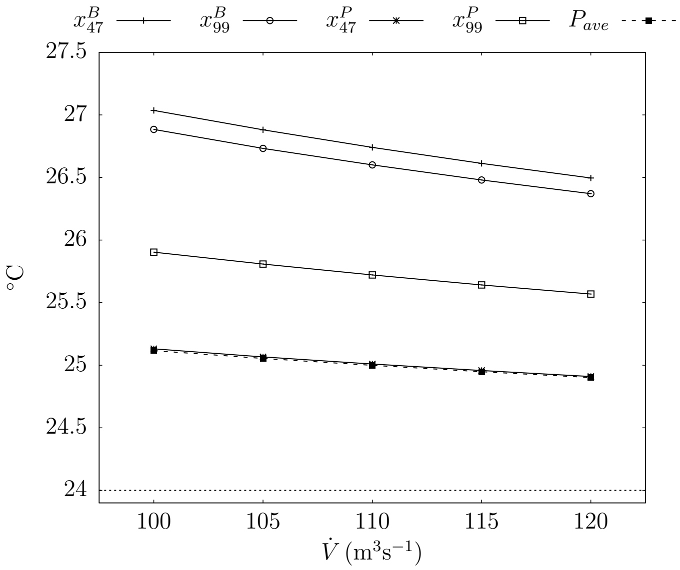

Figure 6.17: Platform air temperatures for departure conditions as a function of piston effect air flow for a 300 Wm^{-3} heat load.

For a piston effect air flow rate increased by 10 m^{3}s^{-1} the highest air temperature, at x_{47}^B, is reduced by 0.24 °C, the lowest air temperature, at x_{47}^P, by 0.10 °C. The average platform air temperature is reduced by 0.10 °C. The average platform temperature is 1.19 °C lower for departure than arrival conditions.

Generally the air temperatures are less influenced by an enhanced piston effect for departure than arrival conditions. This is due to departure conditions being more effective at heat displacement, so there is less potential for further heat displacement.

6.5.2.2 200 Wm^{-3} HEAT LOAD

Figure 6.18 shows platform air temperatures for arrival and departure conditions for a 200 Wm^{-3} braking heat load.

For a 200 Wm^{-3} braking heat load, the patterns observed in the air temperature for arrival and departure conditions are the same, although of less extreme magnitude. For arrival conditions, the points at $x = 47$ m exceed the tunnel air temperature by less than 1.00 °C. The highest air temperature is reduced by 0.29 °C, the lowest by 0.07 °C and the average by 0.13 °C, for an increase in the piston effect of 10 m^{3}s^{-1}. For departure conditions, increasing the piston effect reduces the average platform air temperature by 0.06 °C, and the highest temperature on the platform by 0.16 °C.

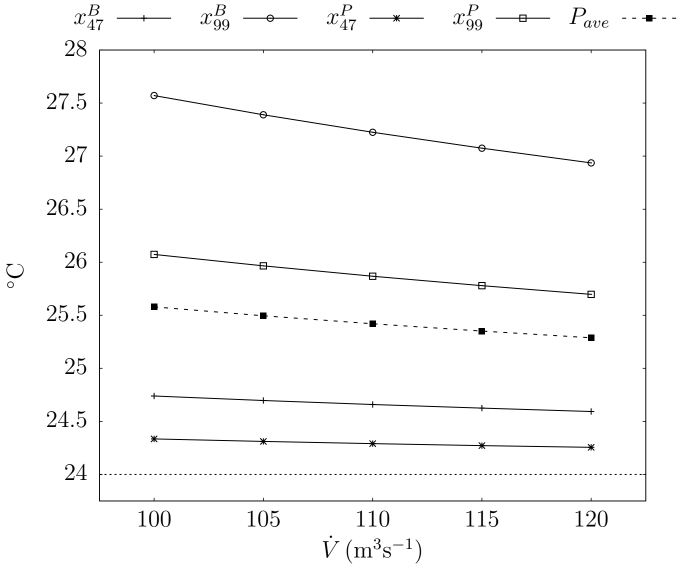

(a) Arrival conditions.

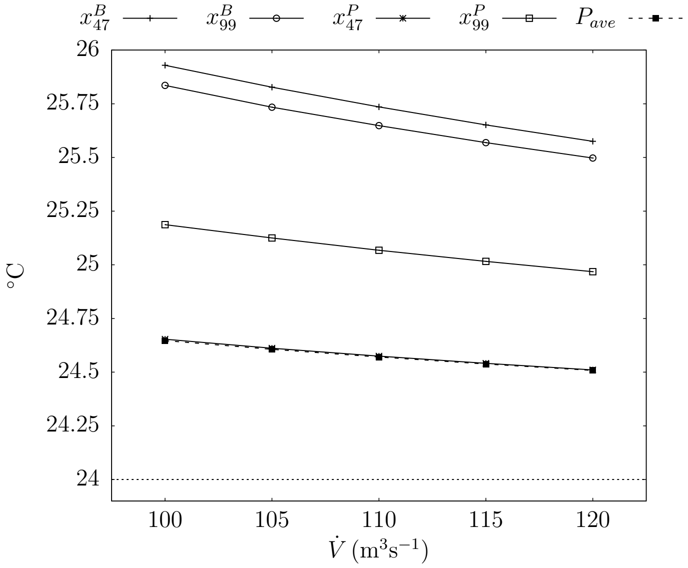

(b) Departure conditions.

Figure 6.18: Platform air temperatures for arrival and departure conditions as a function of piston effect air flow for a 200 Wm^{-3} heat load.

The lowest platform air temperature is reduced by 0.10 °C. The average platform temperature is 0.78 °C lower for departure than arrival conditions.

6.5.2.3 100 $\mathrm{Wm^{-3}}$ HEAT LOAD

Figure 6.19 shows platform air temperatures for arrival and departure conditions for a 100 $\mathrm{Wm^{-3}}$ braking heat load.

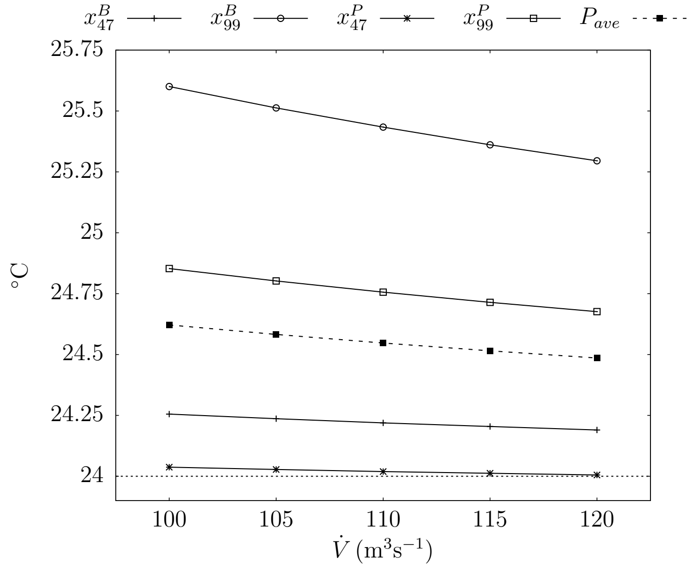

(a) Arrival conditions.

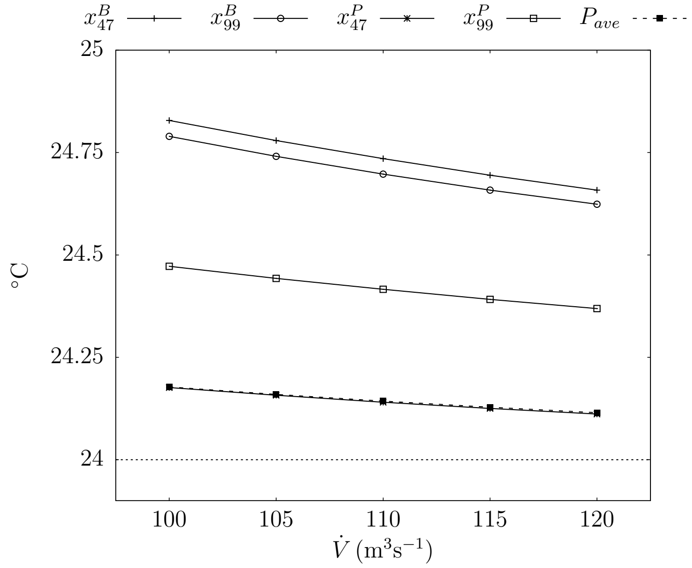

(b) Departure conditions.

Figure 6.19: Platform air temperatures for arrival and departure conditions as a function of piston effect air flow for a 100 $\mathrm{Wm^{-3}}$ heat load.

Due to the low braking heat load, the influence of increasing the piston effect, for both arrival and departure conditions, is less significant. In both conditions average platform air temperatures do not exceed tunnel air temperatures by more than 1.00 °C. For arrival conditions the highest air temperature is reduced by 0.08 °C, the lowest by 0.01 °C and the average by 0.06 °C, for an increase in the piston effect of $10\,\mathrm{m^3 s^{-1}}$. For departure conditions the highest air temperature is reduced by 0.07 °C, the lowest by 0.03 °C and the average by 0.01 °C, for the same increase in piston effect. The effectiveness of arrival and departure conditions in displacing heat show less difference due to the low heat load, with average platform temperature being 0.37 °C lower for departure than arrival conditions. Moreover, the lowest air temperature for arrival conditions is lower than that for departure conditions.

6.5.3 PLATFORM COOLING

In order to assess the influence of increasing the piston effect on platform cooling, the residual heat within the platform for benchmark conditions is compared to conditions due to a $10\,\mathrm{m^3 s^{-1}}$ increase in the piston effect. The residual heat is determined by calculating the heat balance within the platform due to fluxes into and out of the platform and heat loads, by

$$Q_r = \oint_S q\, dS + Q_b \tag{6.1}$$

where Q_r is the residual heat, Q_b the breaking heat load, q the heat fluxes through the platform boundaries and S the boundary surfaces. The difference between the residual heat for benchmark conditions and that of the increased piston effect is termed the cooling effect.

Figure 6.20 shows the cooling effect (kW) due to a $10\,\mathrm{m^3 s^{-1}}$ increase in the piston effect air flow for $100\,\mathrm{Wm^{-3}}$, $200\,\mathrm{Wm^{-3}}$ and $300\,\mathrm{Wm^{-3}}$ braking heat loads, for arrival and departure conditions. The cooling values are given increased by a factor of 24 to represent the movement into and out of the platform of 24 trains per hour, for comparison with results from Ampofo et al. [5].

The cooling due to an increased piston effect is more significant for arrival than

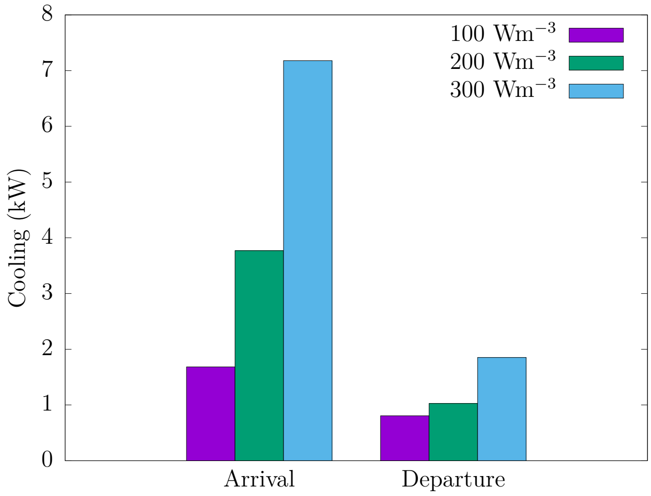

Figure 6.20: Cooling (kW) due to a 10 m^{3}s^{-1} increase in the piston effect air flow for 100 Wm^{-3}, 200 Wm^{-3} and 300 Wm^{-3} braking heat load, for arrival and departure conditions.

departure conditions. As departure conditions are more effective at heat displacement than arrival conditions, the gain achieved from increasing the piston effect is less significant.

The cooling effect for departure conditions with a 300 Wm^{-3} braking heat load is about 1.9 kW and between 0.8–1.0 kW for a 100 Wm^{-3} or 200 Wm^{-3} heat load. The cooling effect for arrival conditions with a 300 Wm^{-3} braking heat load is about a factor of three greater than that observed for departure conditions, but is unlikely to be achieved, as a proportion of the heat will have already been displaced by the departure conditions. Cooling effects of 3.8 kW and 1.7 kW are found for 200 Wm^{-3} and 100 Wm^{-3} heat loads.

As increasing the piston effect will have an influence on platform cooling during the arrival and departure of a train, the cooling effects from both conditions can be combined to arrive at a combined cooling potential. Figure 6.21 shows the combined cooling potential for 100 Wm^{-3}, 200 Wm^{-3} and 300 Wm^{-3} arrival heat loads, as a function of departure heat load.

If it is assumed that the arrival heat load is 100 Wm^{-3} then a combined cooling effect of between 2.5–3.5 kW may be achieved. If a 200 Wm^{-3} arrival heat load is assumed then a combined cooling effect of between 4.5–5.6 kW may be expected. Although a 300 Wm^{-3} arrival heat load is unlikely, a combined cooling effect of

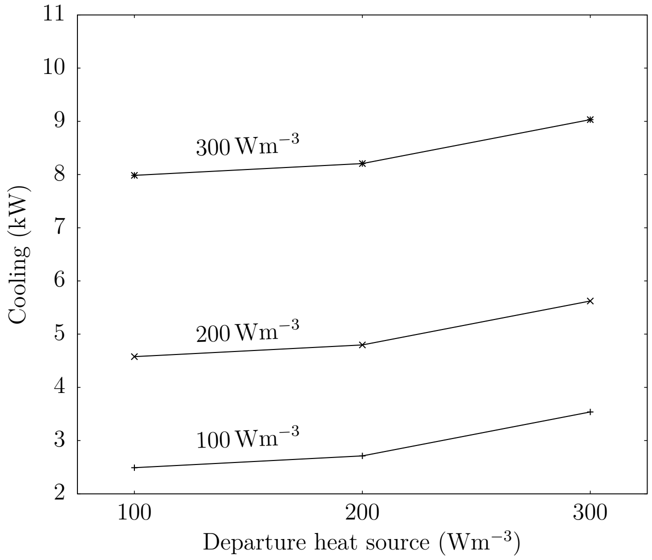

Figure 6.21: Combined cooling potential (kW) for 100 Wm^{-3}, 200 Wm^{-3} and 300 Wm^{-3} arrival heat loads, as a function of the departure heat load.

8.0–9.0 kW is possible in this case.

Ampofo et al. [5] found that by increasing the capacity of ventilation fans by 10 m^{3}s^{-1} of cooling effect of 18.2 kW could be achieved. Although significantly higher than the cooling effect found from increasing the piston effect, increasing capacity of ventilation fans is a very expensive and difficult engineering task. Moreover, the load of running the fans to achieve such a cooling effect was estimated to be in the region of 27.5 kW. Enhancing the piston effect conversely, allows the possibility of displacing heat at the source—platforms—without the requirement for large capital projects or ongoing energy demands.

6.6 Summary

In this chapter the influence of an enhanced piston effect of underground railway thermal conditions was investigated. A 2-d computational model of Blackhorse Road Station, London was developed and verified to find the magnitude and pattern of air flows induced by the arrival and departure of a train. The 2-d model was used to provide boundary conditions for a 3-d model, which was used to show patterns in air flow and temperature and investigate the influence of an enhanced piston effect on thermal conditions on the platform, particularly in relation to the braking heat load.

For train arrival conditions it was found that with a braking heat load of 300 $\mathrm{Wm^{-3}}$ the highest air temperature could be reduced by about 0.44 °C and the average platform air temperature by about 0.20 °C, for an increase in the piston effect of 10 $\mathrm{m^3s^{-1}}$. For train departure conditions, it was found that the highest air temperature could be reduced by about 0.24 °C and the average platform air temperature by about 0.10 °C.

With a braking heat load of 200 $\mathrm{Wm^{-3}}$, it was found that for train arrival conditions the highest air temperature could be reduced by about 0.29 °C and the average platform air temperature by about 0.13 °C, for a increase in the piston effect of 10 $\mathrm{m^3s^{-1}}$. For train departure conditions it was found that the highest air temperature could be reduced by about 0.16 °C and the average platform air temperature by about 0.06 °C.

These reductions compare with that found by Ampofo et al. [5], where it was found that by increasing ventilation fans by 10 $\mathrm{m^3s^{-1}}$ a reduction in air temperature of 0.12 °C could be achieved.

The combined cooling effect of an enhanced piston effect was calculated. For an arrival heat load of 100 $\mathrm{Wm^{-3}}$ then cooling of between 2.5–3.5 kW may be achieved. Similarly, for a 200 $\mathrm{Wm^{-3}}$ arrival heat load a cooling effect of between 4.5–5.6 kW may be expected. These cooling effects can be achieved using little or no energy, and compare favourably with other potential options such as the enhancement of ventilation fans.

7

Conclusion

In this final chapter the findings from the previous chapters are brought together and compared with the objectives set out in the introduction to this thesis. The broad objective of the research was to investigate the potential of enhancing the piston effect air flows for the improvement of underground railway thermal conditions and energy efficiency. The implications of the study as a whole are discussed and finally a range of possible extensions to this research that could be considered for future work are presented.

7.1 CONCLUSIONS

1. The influence of geometric and kinematic parameters were investigated to determine the influence on the piston effect air flows and train drag. The effect of increasing the blockage ratio from $\beta = 0.65$ to $\beta = 0.85$ found that the air flow in the tunnel is increased significantly—the air velocities at the tunnel outlet were found to be almost equal to the train maximum velocity at $\beta = 0.85$.

   It was found that the train drag increases by about 50% during constant velocity, 100% during acceleration and 300% during deceleration. The total air volumes displaced form the tunnel increase at broadly the same rate as the train drag for acceleration and constant velocity phases. During deceleration, the increase in displaced air volume plateaus at about $\beta = 0.75$. The effect of drag during deceleration is a result of the body of air behind the train acting on the back of the train. In this case the drag must be overcome by the train brakes in order to stop the train. Conversely, during the acceleration and cruising phases, the effect of the drag must be overcome by the train traction systems.

The effect of pressure drag was found to be more significant than viscous drag. The effect of increasing the blockage ratio increases the pressure drag significantly. At the highest blockage ratios, the restriction of air flow through the train-tunnel gap reduces the viscous drag.

The train and tunnel lengths were varied and it was found that both strongly influenced the air flows in the tunnel. The train drag was strongly influenced by the tunnel length through increasing the pressure drag while the train length had a less significant impact, as it predominately increases the viscous drag. A longer train was found to increase tunnel outlet velocities by about 30% and generates an increase in drag of about 7.5%, during the constant velocity phase. Overall no differences were found in the fraction of the tunnel volume displaced from the tunnel outlet.

Although increasing the blockage ratio was found to significantly increase the piston effect air flows, the train drag was also found to increase by a similar proportion. This would be an undesirable consequence for the energy demand of trains.

2. A train fin was proposed which protrudes from the side of the train into the train-tunnel gap, in order to increase the piston effect air flow. A fin was investigated in an attempt to derive the benefit of increasing the blockage ratio, without the negative effect of increased drag. The train fin had the

effect of altering the aerodynamic resistance.

The train fin was found to have altered the air flow around the train significantly. Generally, the air displacement was found to increase by about 14%, but with a large increase in the aerodynamic work of about 25%.

The effect of the train fin on the aerodynamic work due to the pressure and viscous forces differs significantly from the behaviour which results from increasing the overall blockage ratio. The train fin restricts the air flow through the train-tunnel gap, therefore reducing the aerodynamic work due to the viscous forces during the acceleration, cruising and deceleration phases. Moreover, during the cruising phase, the decrease in the viscous force also reduces the viscous pressure drag, resulting in a reduction in the aerodynamic work due to the pressure force. Therefore, the aerodynamic work increases mostly due to increases during the acceleration and deceleration phases.

3. In place of the train fin, a train aerofoil was investigated to reduce the increase in aerodynamic work during the acceleration and deceleration phases. The aerofoil generally reduces the air flow through the train-tunnel gap and thus reduces the aerodynamic work due to the viscous force. The aerodynamic work due to the pressure force is reduced significantly during the cruising phase and is also reduced during the acceleration phase for an aerofoil angle of $-10° \leq \theta \leq 6°$. During deceleration the aerodynamic work due to the pressure force increases, except for $-6° \leq \theta \leq 2°$, where small reductions are achieved. An aerofoil at a fixed angle of 10° throughout the motion of the train was found to increase the air displacement by 3% while not increasing the aerodynamic work done by the train. The increase in the air displacement without increasing the aerodynamic work done by the train is possible due to the changes in the air flow patterns induced by the aerofoil and thus the forces acting upon the train. At a fixed angle of 10°, increases in aerodynamic work during the acceleration phase could be counteracted by decreases during the cruising phase, thus reducing the overall aerodynamic work done by the train.

4. It was shown that by using different aerofoil angles in the three phases of the train motion, further increases in the air displacement are possible without increasing aerodynamic work in the rheostatic braking case. This is possible due to the uneven distribution of the air displacement and aerodynamic work within the three phases of train motion. Therefore a large angle of inclination may be used during cruising where the air displacement is high, but during acceleration, a lower angle of inclination may be used as the air displacement within this phase is much less significant than the aerodynamic work. It was found that an increase in air displacement of 8% could be achieved along with no increase in aerodynamic work.

5. The aerodynamic work done during braking can be considered as a positive contribution to the aerodynamic work, in the case of rheostatic braking, or a negative contribution in the case of regenerative braking. Considering the aerodynamic work to be a negative contribution reduces the overall aerodynamic work compared with the rheostatic braking case, as the aerodynamic work during deceleration partially off-sets the aerodynamic work during acceleration and cruising phases. If regenerative braking is assumed, then the train fin increases the aerodynamic work by about 2% and the air displacement by about 7%. For $\beta_g = 0.8$, the air displacement increases by about 14% and the aerodynamic work reduces by about 4%. For the train aerofoil, if regenerative braking is used it is found that any aerofoil angle reduces the aerodynamic work. A maximum increase in air displacement of 8.8% can be achieved, with a significant decrease in aerodynamic work of about 24%

6. The conditions in Blackhorse Road Station, London were investigated to consider the influence of an increased piston effect air flow upon platform thermal conditions.

   For train arrival conditions it was found that with a braking heat load of $300\,\mathrm{Wm^{-3}}$, the highest air temperature could be reduced by about $0.44\,^{\circ}\mathrm{C}$ and the average platform air temperature by about $0.20\,^{\circ}\mathrm{C}$, for an increase

> in the piston effect of 10 m^{3}s^{-1}. For train departure conditions, it was found that the highest air temperatures could be reduced by about 0.24 °C and the average platform air temperature by about 0.10 °C.
>
> With a braking heat load of 200 Wm^{-3}, it was found that for train arrival conditions that the highest air temperature could be reduced by about 0.29 °C and the average platform air temperature by about 0.13 °C, for an increase in the piston effect of 10 m^{3}s^{-1}. For train departure conditions, it was found that the highest air temperatures could be reduced by about 0.16 °C and the average platform air temperature by about 0.06 °C.
>
> These reductions compare with that found in the literature, where it was found that by increasing ventilation fans by 10 m^{3}s^{-1} then a reduction in air temperature of 0.12 °C could be achieved.
>
> The combined cooling effect of an enhanced piston effect was found by considering the cooling effects for both arrival and departure conditions. For an arrival heat load of 100 Wm^{-3} then a combined cooling of between 2.5–3.5 kW may be achieved. Similarly, for a 200 Wm^{-3} arrival heat load, a cooling effect of between 4.5–5.6 kW may be expected. These cooling effects can be achieved using little or no energy, and compare favourably with other potential options, such as the enhancement of ventilation fans.

This study has demonstrated that enhancement of the piston effect is possible, in a way which does not effect the performance of the train. Moreover, it has been shown that by increasing the piston effect, the thermal conditions in stations may be improved, by low energy means. Nevertheless, there are aspects of this study which are limited. The proposed train fin and aerofoil have only been investigated in a preliminary manner, and require further development in design, operation and practical implementation. Further, the influence of an enhanced piston effect has only been shown in steady state. Finally, the influence and of the piston effect has only been considered due to a single train in an isolated platform, whereas in reality the influence will be felt over the whole system. These topics would benefit from future study.

7.2 FUTURE WORK

1. In this study a train fin and aerofoil were investigated to consider the effect on train air displacement and aerodynamic work. This study was carried out using a verified 2-d numerical simulation, and although verified with available data, only limited conclusions can be drawn from the results as to how a fin or aerofoil may perform in a realistic, 3-d scenario. Therefore, consideration of the train fin and aerofoil in a 3-d computational study would be useful.

2. It would be worthwhile to consider the use of a train fin or aerofoil from an experimental perspective. This would not only provide useful insight into the influence of such devices on the air flows but would also provide data for the verification of numerical models. Such an investigation would need to be carried out in a facility able to replicate a train moving through a tunnel.

3. The influence of an enhanced piston effect on station thermal conditions was only evaluated in a steady state simulation. Full consideration of a train arrival and departure, in a transient simulation, would allow the full effect of the enhancement to be represented. Moreover, the uncertainty in the arrival and departure heat loads could be reduced by using the results from a train departure scenario as the initial conditions for an arrival scenario.

4. This study has considered the influence of an enhanced piston effect, induced by a single train, on thermal conditions in an isolated platform. In reality, there will be trains arriving and departing simultaneously, in multiple stations across a system. Therefore, the influence of an enhanced piston effect may effect conditions across many stations and tunnels. Consideration of the effect of an enhancement on the air flows, temperatures and train energy demand across a network could be carried out using well established 1-d modelling methods. This would give a valuable insight into the wider influence of an enhancement to the piston effect

5. Although the use of a train fin or aerofoil was considered in this study for the

increase in ventilating air flows, there are other applications for which they could be used. Instead of considering the devices for the increase in air flow it may be possible for the use to be solely for the reduction of aerodynamic work, and hence energy. Alternatively, in place of increasing air flows then the aerofoil could be used to reduce air flows, which can cause significant issues on platforms, when safety thresholds may be breached.

References

[1] Abbaspour, M., Jafari, M. J., Mansouri, N., Moattar, F., Nouri, N., & Allahyari, M. (2008). Thermal comfort evaluation in Tehran metro using Relative Warmth Index. *International Journal of Environmental Science & Technology*, 5(3), 297–304.

[2] Abi-Zadeh, D., Casey, N., Sadokierski, S., & Tabarra, M. (2003). King's Cross St Pancras Underground Station Redevelopment. In *Underground Construction Conference Proceedings* (pp. 641–653).

[3] Ampofo, F., Maidment, G., & Missenden, J. (2004a). Underground railway environment in the UK Part 1: Review of thermal comfort. *Applied Thermal Engineering*, 24(5), 611–631.

[4] Ampofo, F., Maidment, G., & Missenden, J. (2004b). Underground railway environment in the UK Part 2: Investigation of heat load. *Applied Thermal Engineering*, 24(5-6), 633–645.

[5] Ampofo, F., Maidment, G., & Missenden, J. (2004c). Underground railway environment in the UK: Part 3: Methods of delivering cooling. *Applied Thermal Engineering*, 24(5–6), 647–659.

[6] Ampofo, F., Maidment, G., & Missenden, J. (2011). Application of groundwater cooling scheme for London Underground network. *International Journal of Refrigeration*, 34(8), 2042–2049.

[7] Anderson, J. D. (1995). *Computational fluid dynamics.* McGraw-Hill, 1st edition.

[8] Anderson, R., Maxwell, R., & Harris, N. G. (2009). Maximizing the potential for metros to reduce energy consumption and deliver low-carbon transportation in cities.

[9] Ansuini, R., Larghetti, R., Vaccarini, M., Carbonari, A., Giretti, A., Ruffini, S., Guo, H., & Lau, S. L. (2012). Hybrid modeling for energy saving in subway stations. In *First Building Simulation and Optimization Converence*, number September (pp. 425–432).

[10] ANSYS Inc (2015a). *ANSYS Fluent*. Canonsbury, PA: ANSYS Inc, 15 edition.

[11] ANSYS Inc (2015b). *ANSYS Fluent Theory Guide*. Canonsburg, PA: ANSYS Inc, 15 edition.

[12] ANSYS Inc (2015c). ICEM CFD.

[13] ASHRAE (2010). *ASHRAE Standard 55-2010 (Thermal Environmental Conditions for Human Occupancy)*. American Society of Heating, Refrigerating and Air-Conditioning Engineers.

[14] ASHRAE (2015). HVAC Applications.

[15] ASHRAE (2016). *ASHRAE Standard 62.1-2016 (Ventilation for Acceptable Indoor Air Quality)*. American Society of Heating, Refrigerating and Air-Conditioning Engineers.

[16] Auvity, B., Bellenoue, M., & Kageyama, T. (2001). Experimental study of the unsteady aerodynamic field outside a tunnel during a train entry. *Experiments in Fluids*, 30(2), 221–228.

[17] Baron, A., Molteni, P., & Vigevano, L. (2006). High-speed trains: Prediction of micro-pressure wave radiation from tunnel portals. *Journal of Sound and Vibration*, 296(1–2), 59–72.

[18] Baron, A., Mossi, M., & Sibilla, S. (2001). The alleviation of the aerodynamic drag and wave effects of high-speed trains in very long tunnels. *Journal of Wind Engineering and Industrial Aerodynamics*, 89(5), 365–401.

[19] Bellenoue, M., Auvity, B., & Kageyama, T. (2001). Blind hood effects on the compression wave generated by a train entering a tunnel. *Experimental Thermal and Fluid Science*, 25(6), 397–407.

[20] Bellenoue, M., Morinière, V., & Kageyama, T. (2002). Experimental 3-D simulation of the compression wave, due to train–tunnel entry. *Journal of Fluids and Structures*, 16(5), 581–595.

[21] Bendelius, A. G. (1976). Aerodynamic and thermodynamic evaluation of the Atlanta subway system. In *Proceedings of the 2nd International symposium on aerodynamics and ventilation of vehicle tunnels* (pp. 1–20).

[22] Bennett, D. (2004). *Architecture of the Jubilee Line Extension.* Thomas Telford, London, 1st edition.

[23] Botelle, M., Payne, K., & Redhead, B. (2010). Squeezing the heat out of London's Tube. *Proceedings of the Institution of Civil Engineers - Civil Engineering*, 163(3), 114–122.

[24] Boussinesq, J. (1877). Essai sur la theories des eaux courantes. *Memoires presents par divers savants a l'Academic des Science de l'Institut National de France*, 23(1).

[25] Brown, W. G. (1966). Basic Theory of Rapid-Transit Tunnel Ventilation. *Journal of Engineering for Industry*, 88(1), 1.

[26] Camelli, F. E., Byrne, G., & Löhner, R. (2014). Modeling subway air flow using CFD. *Tunnelling and Underground Space Technology*, 43, 20–31.

[27] Casals, M., Gangolells, M., Forcada, N., Macarulla, M., & Giretti, A. (2014). A breakdown of energy consumption in an underground station. *Energy and Buildings*, 78, 89–97.

[28] Chaudhry, H. N., Hughes, B. R., & Ghani, S. A. (2012). A review of heat pipe systems for heat recovery and renewable energy applications. *Renewable and Sustainable Energy Reviews*, 16(4), 2249–2259.

[29] Choi, J.-K. & Kim, K.-H. (2014). Effects of nose shape and tunnel cross-sectional area on aerodynamic drag of train traveling in tunnels. *Tunnelling and Underground Space Technology*, 41, 62–73.

[30] Chung, T. J. (2002). *Computational Fluid Dynamics.* Cambridge: Cambridge University Press.

[31] CIBSE (2005). Guide B: Heating, Ventilating, Air Conditioning and Refrigeration.

[32] CIBSE (2006). *Guide A: Environmental Design.* Chartered Institution of Building Services Engineers.

[33] Cross, D. (2014). Unpublished photographs.

[34] Cross, D., Hughes, B., Ingham, D., & Ma, L. (2015). A validated numerical investigation of the effects of high blockage ratio and train and tunnel length upon underground railway aerodynamics. *Journal of Wind Engineering and Industrial Aerodynamics*, 146, 195–206.

[35] Cross, D., Hughes, B., Ingham, D., & Ma, L. (2017). Enhancing the piston effect in underground railways. *Tunnelling and Underground Space Technology incorporating Trenchless Technology Research*, (pp. 71–81).

[36] Developmental Science Inc. (1971a). Subway aerodynamic test (SAT) facility.

[37] Developmental Science Inc. (1971b). Vent and station test (VST) facility design.

[38] Developmental Science Inc. (1972a). Subway aerodynamic and thermodynamic test (SAT) facility, single-track aerodynamics.

[39] Developmental Science Inc. (1972b). Vent and station test facility design, Chicago Transit Authority scale model vent shaft testing.

[40] Di Perna, C., Carbonari, A., Ansuini, R., & Casals, M. (2014). Empirical approach for real-time estimation of air flow rates in a subway station. *Tunnelling and Underground Space Technology*, 42, 25–39.

[41] Douglas, J., Gasiorek, J., Swaffield, J., & Jack, L. (2005). *Fluid Mechanics*. Pearson, 5th edition.

[42] Eckford, D. C. & Pope, C. W. (2006). Cooling of Underground Railways. *International Symposium on Aerodynamics and Ventilation of Vehicle Tunnels*, 1, 409–424.

[43] El-Bialy, E. M. & Khalil, E. E. (2010). Experimental and Numerical Investigation of Indoor Environmental Quality in a Subway Station. In *Tenth International Congress of Fluid Dynamics* (pp. 1–6).: ICFD.

[44] Fanger, P. O. (1970). *Thermal comfort : analysis and applications in environmental engineering*. Copenhagen: Danish Technical Press, 1st edition.

[45] Fox, J. & Henson, D. (1971). The prediction of magnitudes of pressure transients generated by a train entering a single line tunnel. *ICE Proceedings*, 49, 53–63.

[46] Fukuchi, G. & Nishizawa, S. (1967). Estimation of the aerodynamic drag of a train in a long tunnel. *Quarterly Report of the Japanese National Railway Technical Research Institute*, 8.

[47] Gelman, V. (2009). Braking energy recuperation. *IEEE Vehicular Technology Magazine*, 4(3), 82–89.

[48] Gerhardt, H. & Krüger, O. (1998). Wind and train driven air movements in train stations. *Journal of Wind Engineering and Industrial Aerodynamics*, 74-76, 589–597.

[49] Gilbert, T., Baker, C., & Quinn, A. (2013a). Aerodynamic pressures around high-speed trains: The transition from unconfined to enclosed spaces. *Pro-*

ceedings of the Institution of Mechanical Engineers, Part F: Journal of Rail and Rapid Transit, 227(6), 609–622.

[50] Gilbert, T., Baker, C. J., & Quinn, A. (2013b). Gusts caused by high-speed trains in confined spaces and tunnels. *Journal of Wind Engineering and Industrial Aerodynamics*, 121, 39–48.

[51] Gonzalez, M. L., Vega, M. G., Oro, J. M. F., & Marigorta, E. B. (2014). Numerical modeling of the piston effect in longitudinal ventilation systems for subway tunnels. *Tunnelling and Underground Space Technology*, 40, 22–37.

[52] González-Gil, A., Palacin, R., & Batty, P. (2013). Sustainable urban rail systems: Strategies and technologies for optimal management of regenerative braking energy. *Energy Conversion and Management*, 75, 374–388.

[53] Gralewski, Z. A. (1979). *The aerodynamic drag of tube vehicles travelling at subsonic speeds*. PhD thesis, Loughborough University.

[54] Han, J., Kwon, S.-b., & Chun, C. (2016). Indoor environment and passengers' comfort in subway stations in Seoul. *Building and Environment*, 104, 221–231.

[55] Hara, T. (1961). Aerodynamic force on a high speed train at a tunnel entrance. *Japanese Society of Mechanical Engineers Bulletin*, 4.

[56] Hara, T. (1965). Method of measuring the aerodynamic drag of train. *Japanese Society of Mechanical Engineers Bulletin*, 8.

[57] Hara, T. (1967). Aerodynamic drag of train. *Quarterly Report of the Japanese National Railway Technical Research Institute*, 8.

[58] Hara, T. & Ohkushi, J. (1962). Model test on aerodynamic phenomena of a high speed train entering a tunnel. *Quarterly Report of the Japanese National Railway Technical Research Institute*, 3.

[59] Hara, T., Ohkushi, J., & Nishimura, B. (1967). Aerodynamic drag of trains. *Quarterly Report of the Japanese National Railway Technical Research Institute*, 8.

[60] Henson, D. (1969). *Pressure transients in railway tunnels.* PhD thesis, University of Leeds.

[61] Henson, D. & Fox, J. (1974a). First paper: An investigation of the transient flows in tunnel complexes of the type proposed for the Channel Tunnel. *Proceedings of the Institution of Mechanical Engineers*, 188, 153–161.

[62] Henson, D. & Fox, J. (1974b). Socond paper: Application to the Channel Tunnel of a method of calculating the transient flows in complex tunnel systems. *Proceedings of the Institution of Mechanical Engineers*, 188, 162–167.

[63] Higton, N. N. (1978). *Pressure transients in railway tunnel complexes.* PhD thesis, University of Leeds.

[64] HM Railway Inspectorate (1996). HS(G) 153/3- Railway Safety Principles and Guidance.

[65] Hong, W. & Kim, S. (2004). A study on the energy consumption unit of subway stations in Korea. *Building and Environment*, 39(12), 1497–1503.

[66] Howe, M. S. (2004). On the design of a tunnel-entrance hood with multiple windows. *Journal of Sound and Vibration*, 273(1–2), 233–248.

[67] Howe, M. S., Iida, M., & Fukuda, T. (2003). Influence of an unvented tunnel entrance hood on the compression wave generated by a high-speed train. *Journal of Fluids and Structures*, 17(6), 833–853.

[68] Hu, S.-C. & Lee, J.-H. (2004). Influence of platform screen doors on energy consumption of the environment control system of a mass rapid transit system: case study of the Taipei MRT system. *Energy Conversion and Management*, 45(5), 639–650.

[69] Huang, Y.-d., Gao, W., & Kim, C.-N. (2010). A numerical study of the train-induced unsteady airflow in a subway tunnel with natural ventilation ducts using the dynamic layering method. *Journal of Hydrodynamics, Ser. B*, 22(2), 164–172.

[70] Huang, Y.-d., Gong, X.-l., Peng, Y.-j., & Kim, C.-N. (2013). Effects of the solid curtains on natural ventilation performance in a subway tunnel. *Tunnelling and Underground Space Technology*, 38, 526–533.

[71] Huang, Y.-d., Gong, X.-l., Peng, Y.-j., Lin, X.-y., & Kim, C.-N. (2011). Effects of the ventilation duct arrangement and duct geometry on ventilation performance in a subway tunnel. *Tunnelling and Underground Space Technology*, 26(6), 725–733.

[72] International Union of Railways (2005). *Determination of railway tunnel cross-sectional areas on the basis of aerodynamic considerations*. Paris, France.

[73] ISO 8996:2004 (2004). *Ergonomics of the thermal environment — Determination of metabolic rate*. International Organization for Standardization.

[74] Jenkins, K., Gilbey, M., Hall, J., Glenis, V., & Kilsby, C. (2014). Implications of climate change for thermal discomfort on underground railways. *Transportation Research Part D: Transport and Environment*, 30, 1–9.

[75] Jia, L., Huang, P., & Yang, L. (2009). Numerical simulation of flow characteristics in a subway station. *Heat Transfer-Asian Research*, 38(5), 275–283.

[76] Juraeva, M., Jin Ryu, K., Jeong, S.-H., & Song, D. J. (2013). Influence of mechanical ventilation-shaft connecting location on subway tunnel ventilation performance. *Journal of Wind Engineering and Industrial Aerodynamics*, 119, 114–120.

[77] Juraeva, M., Lee, J.-h., & Song, D.-J. (2011). A computational analysis of the train-wind to identify the best position for the air-curtain installation. *Journal of Wind Engineering and Industrial Aerodynamics*, 99(5), 554–559.

[78] Juraeva, M., Ryu, K. J., Jeong, S. H., & Song, D. J. (2016). Influences of the train-wind and air-curtain to reduce the particle concentration inside a subway tunnel. *Tunnelling and Underground Space Technology*, 52, 23–29.

[79] Kaffel, A., Moureh, J., Harion, J.-L., & Russeil, S. (2015). Experimental investigation of a plane wall jet subjected to an external lateral flow. *Experiments in Fluids*, 56(5), 95.

[80] Karekla, X. & Tyler, N. (2012). Reduced dwell times resulting from train–platform improvements: the costs and benefits of improving passenger accessibility to metro trains. *Transportation Planning and Technology*, 35(5), 525–543.

[81] Katavoutas, G., Assimakopoulos, M. N., & Asimakopoulos, D. N. (2016). On the determination of the thermal comfort conditions of a metropolitan city underground railway. *Science of The Total Environment*, 566, 877–887.

[82] Ke, M.-T., Cheng, T.-C., & Wang, W.-P. (2002). Numerical simulation for optimizing the design of subway environmental control system. *Building and Environment*, 37(11), 1139–1152.

[83] Khalil, E. E., EL-Bialy, E., Khalil, E. E., & EL-Bialy, E. (2012). Flow Regimes and Thermal Patterns in a Subway Station. *American Journal of Fluid Dynamics*, 2(6), 95–100.

[84] Khayrullina, A., Blocken, B., Janssen, W., & Straathof, J. (2015). CFD simulation of train aerodynamics: Train-induced wind conditions at an underground railroad passenger platform. *Journal of Wind Engineering and Industrial Aerodynamics*, 139, 100–110.

[85] Kim, J. Y. & Kim, K. Y. (2007). Experimental and numerical analyses of train-induced unsteady tunnel flow in subway. *Tunnelling and Underground Space Technology*, 22(2), 166–172.

[86] Kim, J.-Y. & Kim, K.-Y. (2009). Effects of vent shaft location on the ventilation performance in a subway tunnel. *Journal of Wind Engineering and Industrial Aerodynamics*, 97(5–6), 174–179.

[87] Ko, Y.-Y., Chen, C.-H., Hoe, I.-T., & Wang, S.-T. (2012). Field measurements of aerodynamic pressures in tunnels induced by high speed trains. *Journal of Wind Engineering and Industrial Aerodynamics*, 100(1), 19–29.

[88] Krasyuk, A. M. (2005). Calculation of Tunnel Ventilation in Shallow Subways. *Journal of Mining Science*, 41(3), 261–267.

[89] Krasyuk, A. M. & Lugin, I. V. (2007). Investigation of the dynamics of air flows generated by the disturbing action of trains in the Metro. *Journal of Mining Science*, 43(6), 655–661.

[90] Launder, B. & Spalding, D. (1974). The numerical computation of turbulent flows. *Computer Methods in Applied Mechanics and Engineering*, 3(2), 269–289.

[91] Lee, K. B., Park, J. S., Oh, M. D., Bae, S. J., & Kim, S. D. (2014). Field measurement and estimation of ventilation flow rates by using train-induced flow rate through subway vent shafts. *Journal of Mechanical Science and Technology*, 28(7), 2677–2686.

[92] Lee, S., Kim, M. J., & Yoo, C. K. (2015). In search for modeling predictive control of indoor air quality and ventilation energy demand in subway station. *Energy and Buildings*, 98, 56–65.

[93] Lin, C.-J., Chuah, Y. K., & Liu, C.-W. (2008). A study on underground tunnel ventilation for piston effects influenced by draught relief shaft in subway system. *Applied Thermal Engineering*, 28(5–6), 372–379.

[94] Liu, H., Lee, S., Kim, M., Shi, H., Kim, J. T., Wasewar, K. L., & Yoo, C. (2013). Multi-objective optimization of indoor air quality control and energy consumption minimization in a subway ventilation system. *Energy and Buildings*, 66, 553–561.

[95] Liu, T.-h., Tian, H.-q., & Liang, X.-f. (2010). Design and optimization of tunnel hoods. *Tunnelling and Underground Space Technology*, 25(3), 212–219.

[96] London Underground Limited (2000). Engineering Standard E4064 A4: Design of Station and Tunnel Ventilation.

[97] London Underground Limited (2007). *Rolling Stock Information Sheet.* London, U.K.

[98] London Underground Limited (2015). Victoria Line Network Diagram.

[99] Marqués-Bruna, P. & Grimshaw, P. (2011). Design of the Grand Touring sports car wing. *Proceedings of the Institution of Mechanical Engineers, Part P: Journal of Sports Engineering and Technology*, 225(1), 22–31.

[100] Marzouk, M. & Abdelaty, A. (2014). Monitoring thermal comfort in subways using building information modeling. *Energy and Buildings*, 84, 252–257.

[101] Mok, J. K. & Yoo, J. (2001). Numerical study on high speed train and tunnel hood interaction. *Journal of Wind Engineering and Industrial Aerodynamics*, 89(1), 17–29.

[102] Moreno, T., Pérez, N., Reche, C., Martins, V., de Miguel, E., Capdevila, M., Centelles, S., Minguillón, M., Amato, F., Alastuey, A., Querol, X., & Gibbons, W. (2014). Subway platform air quality: Assessing the influences of tunnel ventilation, train piston effect and station design. *Atmospheric Environment*, 92, 461–468.

[103] Mortada, A., Choudhary, R., & Soga, K. (2015). Thermal Modeling and Parametric Analysis of Underground Rail Systems. *Energy Procedia*, 78, 2262–2267.

[104] Muñoz-Paniagua, J., García, J., & Crespo, A. (2014). Genetically aerodynamic optimization of the nose shape of a high-speed train entering a tunnel. *Journal of Wind Engineering and Industrial Aerodynamics*, 130, 48–61.

[105] National Technical Information Service (1968). An air conditioning study of New York City Transit System - Part I: A thermal system model and equipment valuation.

[106] Ono, T., Iwai, K., & Maeda, K. (2006). A new air conditioning and ventilation scheduling method for subway energy saving utilizing the wind driven by trains. *International Symposium on Aerodynamics and Ventilation of Vehicle Tunnels*, 1, 437–450.

[107] Ordódy, P. (2000). Thermal comfort in the passenger areas of the Budapest metro. *Periodica Polytechnica. Mechanical Engineering*, 44(2), 309–317.

[108] Parsons Brinkerhoff Quade & Douglas (1970). Proposed method for aerodynamic mathematical analysis.

[109] Parsons Brinkerhoff Quade & Douglas (1971). Development of basic mathematical models for subway environment simulation.

[110] Parsons Brinkerhoff Quade & Douglas, United States Urban Mass Transportation Administration, Transit Development Corporation, De Leuw Cather & Company, & Kaiser Engineers (1973). Aerodynamic and thermodynamic validation tests in Berkeley Hills Tunnel: Final Report.

[111] Pflitsch, A., Bruene, M., Steiling, B., Killing-Heinze, M., Agnew, B., Irving, M., & Lockhart, J. (2012). Air flow measurements in the underground section of a UK light rail system. *Applied Thermal Engineering*, 32, 22–30.

[112] Pope, C. W. (2001). CrossRail: Ventilation of the central London tunnels. *Proceedings of the Institution of Civil Engineers - Transport*, 147(2), 95–106.

[113] Pope, C. W., Newman, D. G., & Henson, D. A. (2000). The factors affecting draught relief and air temperature in an underground metro system. In *Proceeding of the 10th International symposium on aerodynamics and ventilation of vehicle tunnels*, volume 43 (pp. 153–170).

[114] Rabani, M. & Faghih, A. K. (2015). Numerical analysis of airflow around a passenger train entering the tunnel. *Tunnelling and Underground Space Technology*, 45, 203–213.

[115] Research and Special Programs Administration (2002). *Subway Environmental Design Handbook, vol. II: Subway Environmental Simulation Computer Program.* US Department of Transportation, 4th edition.

[116] Revesz, A., Chaer, I., Thompson, J., Mavroulidou, M., Gunn, M., & Maidment, G. (2016). Ground source heat pumps and their interactions with underground railway tunnels in an urban environment: A review. *Applied Thermal Engineering*, 93, 147–154.

[117] Ricco, P., Baron, A., & Molteni, P. (2007). Nature of pressure waves induced by a high-speed train travelling through a tunnel. *Journal of Wind Engineering and Industrial Aerodynamics*, 95(8), 781–808.

[118] Sabjen, M. (1971). Fluid mechanics of train-tunnel systems in unsteady motion. *AIAA Journal*, 9, 1538–1545.

[119] Shin, C.-H. & Park, W.-G. (2003). Numerical study of flow characteristics of the high speed train entering into a tunnel. *Mechanics Research Communications*, 30(4), 287–296.

[120] Shuanbao, Y., Dilong, G., Zhenxu, S., Guowei, Y., & Dawei, C. (2014). Optimization design for aerodynamic elements of high speed trains. *Computers & Fluids*, 95, 56–73.

[121] Stephen, P. (2016). Cooling the Tube. *Rail Magazine*, (pp. 100–103).

[122] Sutter, K. (1930). *The air resistance of railway trains in tunnels.* PhD thesis, ETH Zurich.

[123] Tabarra, M. & Guan, D. (2005). Measurement of train brake heat in underground systems. In *Independent Technical Conference, Tunnel Design & Systems Engineering* (pp. 93–102).

[124] Tabarra, M., Sadokierski, S., & Abi-Zadeh, D. (2004). Design of a modern subway ventilation system. *Tunnels & Tunnelling International.*

[125] Thompson, J., Maidment, G., Missenden, J., & Ampofo, F. (2007). Geothermal cooling through enhancement of the natural heat sink effect – proof of concept. *Experimental Thermal and Fluid Science*, 31(6), 551–558.

[126] Tollmien, W. (1927). Air resistance and pressure zones around trains in railway tunnels. *VDI Zeitschrift*, 71, 199–203.

[127] Transit Development Corporation (1976). *Subway Environmental Design Handbook, vol. I: Principles and Applications.* National Technical Information Service.

[128] Transport for London (2011). London Underground Environment Strategy 2008-2013.

[129] Transport for London (2016). Facts & figures.

[130] Uystepruyst, D., William-Louis, M., & Monnoyer, F. (2013). 3D numerical design of tunnel hood. *Tunnelling and Underground Space Technology*, 38, 517–525.

[131] Vaccarini, M., Giretti, A., Tolve, L., & Casals, M. (2016). Model predictive energy control of ventilation for underground stations. *Energy and Buildings*, 116, 326–340.

[132] Vardy, A. E. (1980a). Unsteady airflows in rapid transit systems Part 1: measurements on the london transport victoria line. *Proceedings of the Institution of Mechanical Engineers 1847-1982 (vols 1-196)*, 194(1980), 341–348.

[133] Vardy, A. E. (1980b). Unsteady airflows in rapid transit systems Part 2: theoretical background and design parameters. *Proceedings of the Institution of Mechanical Engineers 1847-1982 (vols 1-196)*, 194(1980), 349–356.

[134] Vardy, A. E. (1996a). Aerodynamic drag on trains in tunnels part 1: synthesis and definitions. *Proceedings of the Institution of Mechanical Engineers, Part F: Journal of Rail and Rapid Transit*, 210, 29–38.

[135] Vardy, A. E. (1996b). Aerodynamic drag on trains in tunnels part 2: prediction and validation. *ARCHIVE: Proceedings of the Institution of Mechanical Engineers, Part F: Journal of Rail and Rapid Transit 1989-1996 (vols 203-210)*, 210(16), 39–49.

[136] Versteeg, H. K. & Malalasekera, W. (2007). *An Introduction to Computational Fluid Dynamics: The Finite Volume Method*. Pearson, 2nd edition.

[137] Wang, L., Tao, H., Du, X., Dai, R., & Huang, C. (2015). Theoretical modeling of the platform piston wind wall jet using field measurements and model testing. *Tunnelling and Underground Space Technology*, 45, 1–9.

[138] White, F. (2011). *Fluid Mechanics*. McGraw-Hill, 7th edition.

[139] Wolmar, C. (2004). *The Subterranean Railway: How the London Underground Was Built and How it Changed the City Forever*. London: Atlantic.

[140] Woods, W. & Gawthorpe, R. (1972). The train and tunnel - a large-scale unsteady flow machine. In *Proceedings of the Second J.S.M.E Symposium on Fluid Machinery and Fluidics*.

[141] Woods, W. & Pope, C. (1980). A generalised flow prediction method for the unsteady flow generated by a train in a single tunnel. *Aerodynamics, Journal of Wind Engineering and Industrial*, 7, 331–360.

[142] Xiang, X., Xue, L., & Wang, B. (2015). Aerodynamic Effects of Inclined Portals on the Initial Compression Wave Generated by a High-Speed Train Entering a Tunnel. *Journal of Fluids Engineering*, 137(12), 121104.

[143] Xue, P., You, S., Chao, J., & Ye, T. (2014). Numerical investigation of unsteady airflow in subway influenced by piston effect based on dynamic mesh. *Tunnelling and Underground Space Technology*, 40, 174–181.

[144] Yamamoto, A. (1968). Aerodynamic of train and tunnel. In *First International Conference of Vehicle Mechanics*.

[145] Yan, W., Naiping, G., Lihui, W., & Xiping, W. (2013). A numerical analysis of airflows caused by train-motion and performance evaluation of a subway ventilation system. *Indoor and Built Environment*, (pp. 1–10).

[146] Yang, Z., Su, X., Ma, F., Yu, L., & Wang, H. (2015). An innovative environmental control system of subway. *Journal of Wind Engineering and Industrial Aerodynamics*, 147, 120–131.

[147] Yoshimura, M., Saito, S., Hosaka, S., & Tsunoda, H. (2000). Characteristics of the Aerodynamic Brake of the Vehicle on the Yamanashi Maglev Test Line. *Quarterly Report of RTRI*, 41(2), 74–78.

[148] Younis, B. A. & Cokjat, D. (1997). Eddy-viscosity vs. second-order closures for flows in noncircular ducts. *AIChE Journal*, 43, 893.

[149] Yuan, F.-D. & You, S.-J. (2007). CFD simulation and optimization of the ventilation for subway side-platform. *Tunnelling and Underground Space Technology*, 22(4), 474–482.

[150] Zerihan, J. & Zhang, X. (2000). Aerodynamics of a Single Element Wing in Ground Effect. *Journal of Aircraft*, 37(6), 1058–1064.

[151] Zhang, H., Zhu, C., Zheng, W., You, S., Ye, T., & Xue, P. (2016). Experimental and numerical investigation of braking energy on thermal environment of underground subway station in China's northern severe cold regions. *Energy*, 116, 880–893.

[152] Zhou, D., Tian, H.-q., Zhang, J., & Yang, M.-z. (2014). Pressure transients induced by a high-speed train passing through a station. *Journal of Wind Engineering and Industrial Aerodynamics*, 135, 1–9.